

**EXPERIMENTAL AND COMPUTATIONAL STUDIES OF THERMAL MIXING IN
NEXT GENERATION NUCLEAR REACTORS**

by

Douglas Tyler Landfried

Bachelors of Science, University of Pittsburgh, 2009

Master of Science, University of Pittsburgh, 2013

Submitted to the Graduate Faculty of
Swanson School of Engineering in partial fulfillment
of the requirements for the degree of
Doctorate of Philosophy

University of Pittsburgh

2015

UNIVERSITY OF PITTSBURGH
SWANSON SCHOOL OF ENGINEERING

This dissertation was presented

by

Douglas Tyler Landfried

It was presented on

November 17, 2015

and approved by

Minking Chyu, PhD., Associate Dean for International Initiatives, Dean Sichuan University –

Pittsburgh Institute, Leighton and Mary Orr Chair Professor, Department of Mechanical
Engineering and Material Science, University of Pittsburgh

Laura Schaefer, PhD., Department Chair and Burton J. and Ann M. McMurtry Professor,
Department of Mechanical Engineering, Rice University

Anirban Jana, PhD., Senior Computational Specialist, Pittsburgh Supercomputing Center,

Dissertation Director: Mark Kimber, PhD., Assistant Professor, Department of Nuclear
Engineering, Texas A &M University

Copyright © by Douglas Tyler Landfried

2015

EXPERIMENTAL AND COMPUTATIONAL STUDIES OF THERMAL MIXING IN NEXT GENERATION NUCLEAR REACTORS

Douglas Tyler Landfried, Ph.D.

University of Pittsburgh, 2015

The Very High Temperature Reactor (VHTR) is a proposed next generation nuclear power plant. The VHTR utilizes helium as a coolant in the primary loop of the reactor. Helium traveling through the reactor mixes below the reactor in a region known as the lower plenum. In this region there exists large temperature and velocity gradients due to non-uniform heat generation in the reactor core. Due to these large gradients, concern should be given to reducing thermal striping in the lower plenum. Thermal striping is the phenomena by which temperature fluctuations in the fluid are transferred to and attenuated by surrounding structures. Thermal striping is a known cause of long term material failure. To better understand and predict thermal striping in the lower plenum two separate bodies of work have been conducted. First, an experimental facility capable of predictably recreating some aspects of flow in the lower plenum is designed according to scaling analysis of the VHTR. Namely the facility reproduces jets issuing into a crossflow past a tube bundle. Secondly, extensive studies investigate the mixing of a non-isothermal parallel round triple-jet at two jet-to-jet spacings was conducted. Experimental results were validated with an open source computational fluid dynamics package, OpenFOAM®. Additional care is given to understanding the implementation of the realizable $k-\epsilon$ and Launder Gibson RSM turbulence Models in OpenFOAM®. In order to measure velocity and temperature in the triple-jet experiment a detailed investigation of temperature compensated hot-wire anemometry is carried out with special concern being given to quantify the error with the

measurements. Finally qualitative comparisons of trends in the experimental results and the computational results is conducted. A new and unexpected physical behavior was observed in the center jet as it appeared to spread unexpectedly for close spacings ($S/D_{jet} = 1.41$).

TABLE OF CONTENTS

1.0	INTRODUCTION.....	1
1.1	VERY HIGH TEMPERATURE REACTOR.....	1
1.2	THERMAL STRIPING AND TRIPLE-JET STUDIES	5
2.0	DESIGN OF AN EXPERIMENTAL FACILITY.....	14
2.1	FLOW SKID DESIGN	14
2.1.1	Heater and Heat Exchanger Specifications.....	18
2.1.2	Blower Specifications	20
2.1.3	Uncertainty of Mass Flow Rate	24
2.1.4	Control of Mass Flow Rate	27
2.2	UNIT CELL EXPERIMENTAL DESIGN	28
2.2.1	Design of a Unit Cell Experiment.....	28
2.2.2	Scaling and Experimental Measurements in the Unit Cell Design	30
2.2.3	Implementation and Fabrication of the Unit Cell Design.....	36
3.0	CHARACTERIZATION OF JET FLOW BEHAVIOR.....	44
3.1	EXPERIMENTAL APPROACH.....	44
3.1.1	In-Situ Single Wire Calibration	45
3.1.2	Flow Conditioning	45
3.1.3	Temperature Correction Error Quantification	56

3.2	VELOCITY CONTOURS AND TURBULENCE QUANTIFICATION.....	61
3.3	QUANTIFICATION OF JET PROFILE.....	64
4.0	MEASUREMENTS IN A PARALLEL-TRIPLE-JET	71
4.1	ERROR ASSESSMENT OF TRIPLE-JET MEASUREMENTS	72
4.2	ANALYSIS OF TRIPLE-JET FLOW PROFILES.....	80
4.3	TRENDS IN THE TRIPLE-JET.....	88
5.0	NUMERICAL MODELING OF A PARALLEL TRIPLE-JET	95
5.1	MESH DESIGN	96
5.2	SOLVER SELECTION AND TURBULENCE MODELING BACKGROUND IN OPENFOAM®	99
5.2.1	Reynolds-Averaged Navier Stokes Equations.....	99
5.2.2	Realizable k- ϵ Turbulence Model	101
5.2.3	Reynolds Stress Transport Models	104
5.2.3.1	RANS/RSM Wall Functions.....	107
5.2.4	Steady State Solution (RANS) - buoyantSimpleFoam	109
5.3	GRID CONVERGENCE INDEX (GCI)	110
5.4	SIMULATION RESULTS.....	113
5.4.1	Parabolic Velocity vs Tophat Velocity Profile	114
5.4.2	Comparison of Turbulence Models.....	120
6.0	FUTURE WORK	125
	APPENDIX A	128
	APPENDIX B	133
	APPENDIX C	137

BIBLIOGRAPHY..... 145

LIST OF TABLES

Table 1 – Pipe Lengths and Diameters in flow skid	21
Table 2 – Expansion and contraction ratios	22
Table 3 - Assumed values and uncertainties	26
Table 4 - Velocity and temperature calibration experiments	67
Table 5 – Matrix of cases mapped in horizontal plane	72
Table 6 - Matrix of cases mapped in vertical plane through jet centerline	72
Table 7 – Errors in experimental inlet conditions	74
Table 8 – Estimated bulk temperature of flow into test section for each case	89
Table 9 - Boundary conditions for realizable $k-\varepsilon$ model without wall functions	104
Table 10 - Boundary conditiosn for RSM simulation	107
Table 11 - Matrix of simulations ran	114
Table 12 - IDDES Boundary Conditions	140

LIST OF FIGURES

Figure 1- Illustration of the VHTR	2
Figure 2 - CFD predictions of streamlines colored with temperature [K] in a computer model of the lower plenum of a VHTR.....	4
Figure 3- CFD prediction of streamlines colored with velocity magnitude [m/s] in the lower plenum of a VHTR (Magnitudes greater than 70 m/s appear red. Adapted from data in [4]	4
Figure 4 – Illustration of a round parallel triple-jet showing the mixing and development downstream.....	7
Figure 5 - Schematic of the experimental test section with honeycomb flow conditioners pictured	16
Figure 6 - Triple-jet experimental test section.....	18
Figure 7 - Plot of predicted system curve with the manufacturer supplied blower curves.....	24
Figure 8 - Percent uncertainty of mass flow rate and individual uncertainty components.....	27
Figure 9 – Half Model of the VHTR lower plenum with jets (colored) and posts (grey) [27].....	29
Figure 10 – Matched index of refraction facility test section at INL [27].....	30
Figure 11 – Experimental unit cell for studying the lower plenum of the VHTR.....	31
Figure 12 - Isometric view of the test section with key design components highlighted.....	35
Figure 13 - Thermocouple/Support post assembly with thermocouples shown	36
Figure 14 – Cross flow wind tunnel design	37
Figure 15: (a) Array of six jets located above test section (b) transparent jet revealing internal honeycomb insert	39
Figure 16: Transparent circular top plate with post configuration	40

Figure 17: Stepper motor coupled to center post via a shaft.....	41
Figure 18 – Ice point facility.....	43
Figure 19 - Illustration of experimental facility for studies for single round	45
Figure 20- Calibration velocity versus CTA voltage corrected for temperature	50
Figure 21 – Comparison of calibration and predicted velocities	51
Figure 22 – (a) CTA calibration curves for heated flows	53
Figure 23 – Temperature dependency of a and c with curve fits shown	54
Figure 24 – Curve fit velocity versus calibration velocity for all tested data	55
Figure 25 - CTA and CCA two-wire probe	56
Figure 26 $-x/D_{jet}=0.33$ (a) straight pipe (b) Coarse honeycomb (c) Refined honeycomb	46
Figure 27 – (a) Coarse honeycomb (b) refined honeycomb (c) ceramic honeycomb – shown in pipe coupling.....	47
Figure 28 - (a) Velocity magnitude with simultaneous temperature correction [m/s] (b) Velocity magnitude with collocated temperature correction [m/s] (c) Temperature [°C]. For each contour, the circular jet geometry is included for reference (solid black line, $D_{jet} = 0.875$ in (22.23 mm)). $Re_{jet} = 10.6 \times 10^3$	59
Figure 29 – Error [m/s] between different velocity correction methods. The circular jet geometry is included for reference (solid black line, $D_{jet} = 0.875$ in (22.23 mm)). $Re_{jet} = 10.6 \times 10^3$	60
Figure 30 – triple-jet velocity magnitude for $R=1/2$ $\Delta T=60^\circ C$ (a) Velocity Magnitude using simultaneous temperature correction (b) - Velocity Magnitude using collocated temperature correction.	61
Figure 31 - Contours at $x/D_{jet} = 0.09$: (a) Simultaneously corrected velocity magnitude (m/s), (b) turbulent kinetic energy (m^2/s^2), and (c) percent turbulence intensity. For each contour, the circular jet geometry is included for reference (solid black line, $D_{jet} = 22.23$ mm). $Re_{jet} = 10.6 \times 10^3$	63
Figure 32 - Surface plots of single jet contours. (a) Turbulent kinetic energy [m2/s2] (b) Percent turbulent intensity	63
Figure 33 - Schematic of line traces used to analyze single jet	65
Figure 34 – Normalized velocity contours “folded” on each other with curve over 90% D_{jet} for $x/D_{jet} = 0.09$ for $Re_{jet} = 10.6 \times 10^3$, $U_0 = 13.78$ m/s	66

Figure 35 - Temperature contours “folded” on each other with curve over 90% D_{jet} for $x/D_{jet}=0.09$ for $Re_{jet} = 10.6 \times 10^3$	70
Figure 36 – Case H1: $R = 1/2$, $\Delta T = 44.4^\circ\text{C}$, $S/D_{jet} = 1.41$ measured at $x/D_{jet} = 0.09$ (a) profiles of velocity magnitude [m/s], and (b) temperature profiles [$^\circ\text{C}$].....	76
Figure 37 - Case H4: $R = 1/2$, $\Delta T = 44.4^\circ\text{C}$, $S/D_{jet} = 3$ measured at $x/D_{jet} = 0.09$ (a) profiles of velocity magnitude [m/s], and (b) temperature profiles [$^\circ\text{C}$].....	77
Figure 38 - Case H5: $R = 1/2$, $\Delta T = 11.1^\circ\text{C}$, $S/D_{jet} = 3$ measured at $x/D_{jet} = 0.09$ (a) profiles of velocity magnitude [m/s], and (b) temperature profiles [$^\circ\text{C}$].....	78
Figure 39 – Difference in temporally congruent and spatially congruent velocity correction methods [m/s] (a) case H1: measured at $x/D_{jet} = 0.09$, (b) case H2: measured at $x/D_{jet} = 5$, and (c) case H3: measured at $x/D_{jet} = 10$	80
Figure 40 – Velocity contours [m/s] for $R = 1/2$, $\Delta T = 44.4^\circ\text{C}$, $S/D_{jet} = 1.41$ (a) measured at $x/D_{jet} = 0.09$, (b) measured at $x/D_{jet} = 5.09$, and (c) measured at $x/D_{jet} = 10.09$	82
Figure 41 – Temperature contours [$^\circ\text{C}$] for $R = 1/2$, $\Delta T = 44.4^\circ\text{C}$, $S/D_{jet} = 1.41$ (a) measured at $x/D_{jet} = 0.09$, (b) measured at $x/D_{jet} = 5.09$, and (c) measured at $x/D_{jet} = 10.09$	84
Figure 42 - Traces for triple-jet study and the averaging applied – \square inner horizontal averages, \times outer horizontal averages, \circ vertical averages, \square inner diagonal averages, \times outer diagonal traces. Black circle represents jet.	85
Figure 43 - Symmetrically averaged inlet profiles the case H1 measured at $x/D_{jet} = 0.09$. (a) averaged traces for both hot jets, and (b) averaged traces for cold jet.....	85
Figure 44 - Symmetrically averaged inlet profiles the case H4 measured at $x/D_{jet} = 0.09$. (a) averaged traces for both hot jets, and (b) averaged traces for cold jet.....	86
Figure 45 - Symmetrically averaged inlet profiles the case H5 measured at $x/D_{jet} = 0.09$. (a) averaged traces for both hot jets, and (b) averaged traces for cold jet.....	87
Figure 46 – Effects of temperature on the non-dimensional triple-jet velocity profile for different downstream distances (a) measured at $x/D_{jet} = 0.09$, (b) measured at $x/D_{jet} = 0.59$, (c) measured at $x/D_{jet} = 1.09$, (d) measured at $x/D_{jet} = 4.09$, and (e) measured at $x/D_{jet} = 6.09$	90
Figure 47 – Effect of temperature difference on the non-dimensional triple-jet temperature profiles at different downstream distances (a) measured at $x/D_{jet} = 0.09$, (b) measured at $x/D_{jet} = 0.59$, (c) measured at $x/D_{jet} = 1.09$, (d) measured at $x/D_{jet} = 4.09$, and (e) measured at $x/D_{jet} = 6.09$	91
Figure 48 – Differences related to velocity ratio for triple-jet velocity profiles at different downstream distances (a) measured at $x/D_{jet} = 0.09$, (b) measured at $x/D_{jet} = 0.59$, (c) measured at $x/D_{jet} = 1.09$, (d) measured at $x/D_{jet} = 4.09$, and (e) measured at $x/D_{jet} = 6.09$	93

Figure 49 – Simulation domain. Lines: - walls, -- symmetry planes, hot jets, cold jets. Shaded section represents quarter model.....	97
Figure 50 – Mesh structure. Lines: – walls, -- symmetry plane, cold jet, hot jet, -.- mesh regions	98
Figure 51 – Illustration of mesh layers between the jet and the shear layer. Lines: -- symmetry plane, cold jet, hot jet, -.- mesh regions, -inscribed box with 10 elements.....	99
Figure 52 - Mean velocity profiles in fully-developed turbulent channel flow measured by Wei and Willmarth []. \circ , $Re_0 = 2,970$; \square , $Re_0 = 14,914$; Δ , $Re_0 = 2,970$; ∇ , $Re_0 = 39,582$; line, the log law (Taken from Pope [47]).....	108
Figure 53 – Comparison of axial velocity profile in simulations with parabolic inlet profiles. (a) measured at $x/D_{jet} = 0.06$, (b) measured at $x/D_{jet} = 0.25$, (c) measured at $x/D_{jet} = 1$, (d) measured at $x/D_{jet} = 3$, (e) measured at $x/D_{jet} = 6$, (f) measured at $x/D_{jet} = 9$, and (g) measured at $x/D_{jet} = 18$	116
Figure 54 – Comparison of temperature profiles in simulations with parabolic inlet profiles. (a) measured at $x/D_{jet} = 0.06$, (b) measured at $x/D_{jet} = 0.25$, (c) measured at $x/D_{jet} = 1$, (d) measured at $x/D_{jet} = 3$, (e) measured at $x/D_{jet} = 6$, (f) measured at $x/D_{jet} = 9$, and (g) measured at $x/D_{jet} = 18$	117
Figure 55 - Comparison of turbulent kinetic energy profiles in simulations with parabolic inlet profiles. (a) measured at $x/D_{jet} = 0.06$, (b) measured at $x/D_{jet} = 0.25$, (c) measured at $x/D_{jet} = 1$, (d) measured at $x/D_{jet} = 3$, (e) measured at $x/D_{jet} = 6$, (f) measured at $x/D_{jet} = 9$, and (g) measured at $x/D_{jet} = 18$	118
Figure 56 - Comparison of axial velocity profiles for tophat and parabolic inlet velocity profiles for both jet configurations. (a) measured at $x/D_{jet} = 0.06$, (b) measured at $x/D_{jet} = 0.25$, (c) measured at $x/D_{jet} = 1$, (d) measured at $x/D_{jet} = 3$, and (e) measured at $x/D_{jet} = 6$	119
Figure 57 - Comparison of temperature profiles for tophat and parabolic inlet velocity profiles for both jet configurations. (a) measured at $x/D_{jet} = 0.06$, (b) measured at $x/D_{jet} = 0.25$, (c) measured at $x/D_{jet} = 1$, (d) measured at $x/D_{jet} = 3$, and (e) measured at $x/D_{jet} = 6$	120
Figure 58 - Comparison of axial velocity profiles for different turbulence models. (a) measured at $x/D_{jet} = 0.06$, (b) measured at $x/D_{jet} = 0.25$, (c) measured at $x/D_{jet} = 1$, (d) measured at $x/D_{jet} = 3$, and (e) measured at $x/D_{jet} = 6$	122
Figure 59 - Comparison of turbulent kinetic energy profiles for different turbulence models. (a) measured at $x/D_{jet} = 0.06$, (b) measured at $x/D_{jet} = 0.25$, (c) measured at $x/D_{jet} = 1$, (d) measured at $x/D_{jet} = 3$, and (e) measured at $x/D_{jet} = 6$	123
Figure 60 - Contours at $x/D_{jet} = 0.333$: (a) velocity (m/s), (b) turbulent kinetic energy (m^2/s^2), and (c) percent turbulence intensity. For each contour, the circular jet geometry is included for reference (solid black line, $D_{jet} = 0.875$ in (22.2 mm)). $Re_{jet} = 19.8 \times 10^3$	129

Figure 61 - Contours at $x/D_{jet} = 3$: (a) velocity (m/s), (b) turbulent kinetic energy (m^2/s^2), and (c) percent turbulence intensity. For each contour, the circular jet geometry is included for reference (solid black line, $D_{jet} = 0.875$ in (22.2 mm)). $Re_{jet} = 19.8 \times 10^3$ 130

Figure 62 - Contours at $x/D_{jet} = 8$: (a) velocity (m/s), (b) turbulent kinetic energy (m^2/s^2), and (c) percent turbulence intensity. For each contour, the circular jet geometry is included for reference (solid black line, $D_{jet} = 0.875$ in (22.2 mm)). $Re_{jet} = 19.8 \times 10^3$ 130

Figure 63 – Measured at $x/D_{jet}=0.33$ (a) normalized velocity contours “folded” on each other, and (b) curve fit over 0.85% of data included 132

Figure 64 - Normalized velocity contours “folded” on each other. (a) measured at $x/D_{jet}=8$, and (b) measured at $x/D_{jet}=16$ 132

Figure 65 – Dantec Dynamics 55P91 three wire anemometer 133

PREFACE

Thank you to all those who have offered assistance, both mental and physical, on the completion of the current work. It has been an undertaking that is not possible without each and everyone involved. I would like to offer special thanks to my friends and lab mates who without I would have burned out long ago. Thank you to Andy and Thorin for your continuous support, assistance, and interest in the project. Finally special thanks to my loving and caring parents and sister, Mike Cushman, and Dr. Mark Kimber all of whom have helped me throughout the entirety of my graduate schooling. I owe you all so much.

-Tyler

This research is being performed using funding received from the DOE Office of Nuclear Energy's Nuclear Energy University Programs.

1.0 INTRODUCTION

1.1 VERY HIGH TEMPERATURE REACTOR

The Very High Temperature Reactor (VHTR) is a next generation nuclear reactor, one of the six concepts originally proposed by the Generation IV International Forum (GIF). This presents a solution where Helium is employed as the coolant, and subsequently used for high-efficiency production of either electricity or hydrogen. As shown in Figure 1, the Helium travels vertically downward through the core picking up heat from the core and then enters the lower plenum much like an array of jets. Due to the non-uniform heat generation in the core, the temperature of these jets directed into the lower plenum can vary significantly. In the current designs for the VHTR lower plenum 272 jets issue into a hexagonal array of 196 posts. In this design, there are 68 83.8 mm jets, 72 116.8 mm jets, and 132 144.8 mm jets which can vary in both inlet temperature and mass flow rate. The temperature of these jets can vary from 1050 K to 1370 K with velocities ranging from 12 m/s to 150 m/s [1,4]. Analysis by Rodriguez and El-Genk [2], as well as Bayless [3], suggest temperature differences between two jets in close proximity can be on the order of 300°C, with velocity differences of 50-100 m/s. Once in the lower plenum, the flow of these jets changes directions by 90° and traverses across complex geometric features, including an array of cylindrical support posts. Preliminary simulations of the lower plenum, conducted by Mazumdar et al. [4] show that there are thermal “hot streaks” that

interact with neighboring cold streaks in close proximity to posts and other important structures, as shown in Figure 2. In addition to these hot streaks, large velocity gradients exist, as illustrated in Figure 3 which is generated from data presented in Mazumdar et al. [4]. As shown in Figure 3, the flow in the lower plenum is accelerates as it approaches the outlet where the average velocity is approximately 70 m/s. As this is an extremely complicated flow there has been much recent effort [5- 11] dedicated to better modeling techniques and fundamental understanding of the associated turbulent mixing characteristics.

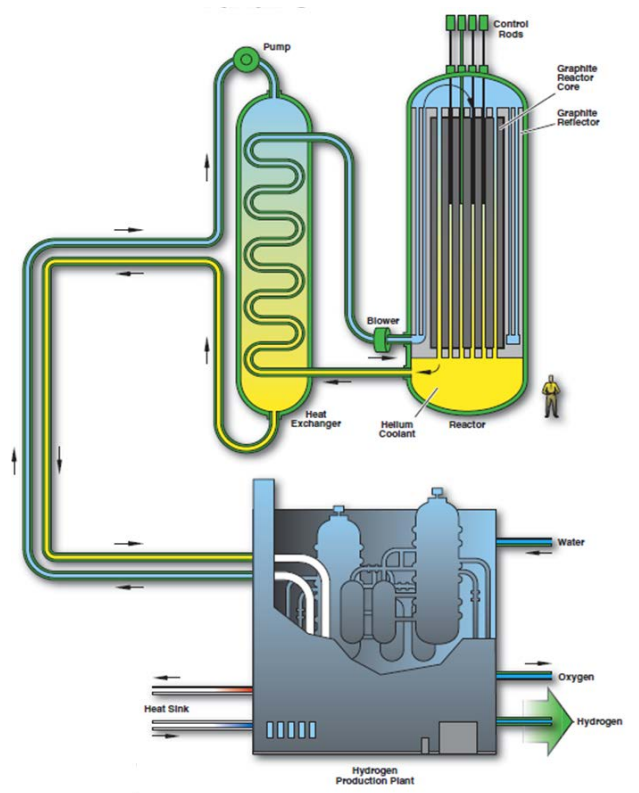


Figure 1- Illustration of the VHTR¹

The hot streaks caused by the non-isothermal mixing raise major concerns regarding structural failure due to thermal fatigue, since temperature fluctuations in fluid flow can

¹ <http://www.gen-4.org/Technology/systems/vhtr.htm>

ultimately be transmitted to the support structure. This phenomenon is known as thermal striping, and represents a significant challenge for the next generation gas cooled nuclear reactors, not just the VHTR. In order to achieve approval for any new reactor design, thermal hydraulic analysis must be performed of the reactor under normal and accident scenarios. Modeling tools used for this purpose (e.g., TRACE, RELAP) have been vetted by the Nuclear Regulatory Commission (NRC) through rigorous verification and validation (V&V) procedures. Therefore, a certain level of trust is tied to the analysis results themselves. However, this same amount of trust cannot be applied for next generation reactors, whose operating conditions greatly differ than today's prevalent reactor types. In addition, the fully vetted tools are systems level codes with 1-D thermal-hydraulic modeling capabilities, and cannot account for localized phenomena such as thermal striping. Therefore, a significant need exists for a more fundamental understanding of this complicated lower plenum flow, one where modeling tools have also been experimentally validated for turbulent mixing of isothermal and non-isothermal jets. This is consequently the primary goal of the proposed work. Both computational and experimental studies are conducted for turbulent jets (single and multiple jet configurations) under isothermal and non-isothermal conditions. Round jets are of primary interest, and investigations are conducted for a single jet and parallel round triple-jet configurations. The velocity and temperature fields are the response metrics of interest, and the input variables include jet Reynolds number, temperature difference between the jet and ambient, and temperature difference between the jet and its neighboring jets. A detailed literature survey is included next to provide perspective of previous and ongoing efforts related to thermal striping and triple-jet studies.

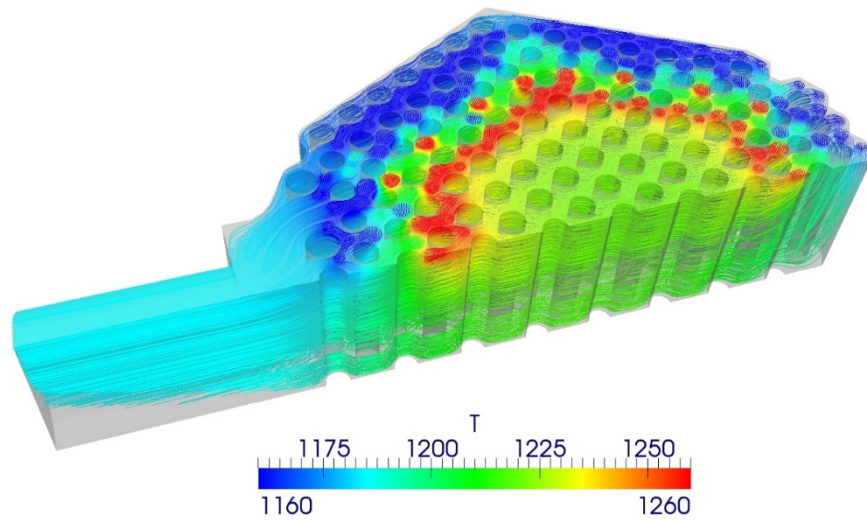


Figure 2 - CFD predictions of streamlines colored with temperature [K] in a computer model of the lower plenum of a VHTR.

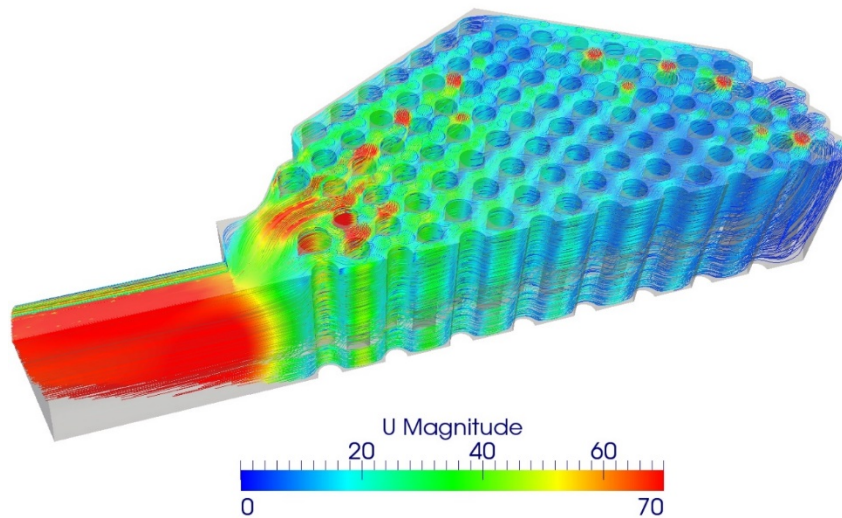


Figure 3- CFD prediction of streamlines colored with velocity magnitude [m/s] in the lower plenum of a VHTR (Magnitudes greater than 70 m/s appear red. Adapted from data in [4])

1.2 THERMAL STRIPING AND TRIPLE-JET STUDIES

Thermal striping is the process by which temperature fluctuations due to mixing of different temperature fluid flows are transported through the fluid boundary layers at the wall and then into the support structure. It has been observed that, with time, this can cause thermal fatigue. The Sodium Fast-Breeding reactor PHENIX (France) experienced cracking from thermal striping in a mixing tee due to stratified flow from injection [12].

The concept of thermal striping has been explored previously by several authors, however always in specific geometric configurations, with a limited number of operational parameters. Perhaps the most extensively studied flow configuration is stratified flow, specifically in regard to internal pipe flow with a tee branch. A 1993 study by Kim et al [13] investigated thermal stratification, turbulence penetration, and thermal striping where hot flow passed through a mixing tee. The branch of the tee was stagnant and at a lower temperature. Their primary interest was determining the conditions where thermal striping was observed in the stagnant branch. Using two thin film anemometers and dye injection, flow patterns were categorized in the branch piping. Additional attention was given to determining the effects of swirl in the bypass flow. It was found that the turbulence penetration length was independent of the main line velocity. Leakage of the cold-branch line into the main line was found to be minimal under most conditions.

Similar research was carried out by Kimura et al. [14] in 2005. Cold fluid was injected perpendicularly into a heated cross flow. The intent was to determine the effects of having an upstream elbow in the cross flow, and to better understand turbulent temperature mixing upstream of the injection. The velocity field was visualized using Particle Image Velocimetry (PIV), while the downstream temperature was measured using a movable thermocouple tree.

Three different branch flows were classified and investigated based on momentum ratio, corresponding to an impinging branch jet, deflecting jet, and wall jet. Temperature fluctuation and fluctuation intensity were measured for each case. It was found that the elbow significantly increased the temperature fluctuation intensity for all scenarios. Special consideration was given to the wall jet case, where a large fluctuation was witnessed due to the effects of an upstream elbow.

In a 2009 experiment by Kamide et al. [15], the work of Kimura et al. [14] was expanded to include comparisons to numerical results. Experiments were conducted without an upstream elbow and compared to a finite difference thermal hydraulic code. Flow visualization of the wall jet case revealed strong eddy formation just downstream of the branch pipe opening, but not for the case of the deflecting or impinging jets. These eddies had large temperature fluctuations in them, believed to contribute strongly to thermal mixing behavior. Moreover, for the wall jet, a prominent temperature fluctuation frequency was found at a Strouhal number of approximately 0.2. This is similar to Karmen Vortex generation from flow past a cylinder, where a Strouhal number of 0.2 is expected across a wide range of Reynolds numbers. For the conditions in Kamide et al. [15], a Strouhal number of 0.2 corresponds to a prominent frequency of approximately 6 Hz. A prominent temperature fluctuation frequency was not found for the impinging and wall jets.

A Detached Eddy Simulation (DES) code, a hybrid of Reynolds Averaged Navier Stokes (RANS) and Large Eddy Simulation (LES) codes, was used by Nakamura et al. [16] to further investigate thermal striping in a mixing tee. Numerical results of the DES were compared to the WALTON experimental data from the Japan Nuclear Cycle Development Institute (JNC DI). Similar to previous studies by Kimura et al. [14] and Kamide et al. [15], cold water was injected

in the branch of the mixing tee. The DES code accurately predicted distributions of temperature fluctuation for both the impinging and deflecting jet. However, the maximum fluctuation intensity in the wall jet case was underestimated by the code. Finally, frequency distributions of temperature near the pipe walls were in good agreement between the experiment and the DES.

A parallel triple-jet is somewhat of a canonical flow in thermal mixing. A parallel triple-jet, much as the name implies, consists of three jets, whose axes lay in a common plane, an illustration of which is shown in Figure 4. Triple-jet investigations have included both round jets and slot jets, normally with the two outer jets sharing a common flow condition, while the center jet is varied. There are numerous variables that can be studied including the velocity ratio between the center jet and the isovelocitory outer jets, the temperature difference between the cold center jet and the hot outer jets, and geometric properties of the three-jet array (e.g., spacing between jets). Of particular interest is the manner in which temperature fluctuations in the flow field occur and how they are attenuated within the flow field.

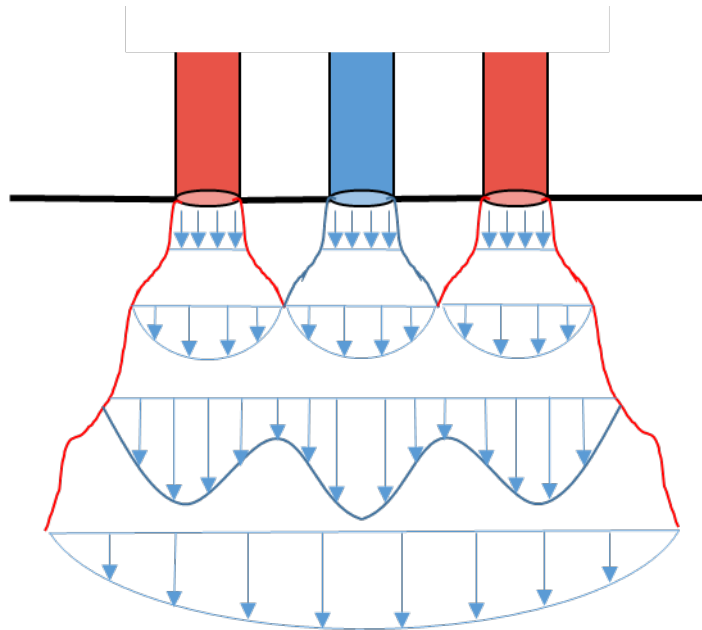


Figure 4 – Illustration of a round parallel triple-jet showing the mixing and development downstream

Tokuhiro and Kimura [17] investigated the thermal striping phenomenon in vertical parallel triple slot jets, producing a quasi-two dimensional flow. For the experiment, a non-buoyant, cold jet, was situated between two buoyant hot jets. Velocity ratios between the hot and cold jets were varied, as well as temperature differences between the jets. Velocity was measured using ultrasound Doppler velocimetry, while temperature data was collected using a movable thermocouple tree. Additionally, dye injection was used to visualize the flow fields. Data for the non-isothermal triple-jet was compared to data for a single jet. For the triple-jet, local maximums of the velocity field were observed close to the center of each jet. These distinct peaks decayed along the axial distance, as the fluid approached a well-mixed condition. However, the flow was not symmetric about the center jet, possibly due to measurement error. The velocity fluctuation intensity was calculated along the axial direction for the center of the cold jet. Compared to the single jet, the non-dimensional fluctuation intensity is approximately three times larger for the triple-jet until 9 diameters downstream, denoted as $x/D_{jet} = 9$. Temperature data was collected for the spanwise and axial directions, for both the isovelocity and non-isovelocity conditions. For axial locations near to the jet exit, sharp temperature gradients were observed near the interface of the hot and cold jets. The gradients decreased as axial distance increased, since the fluid temperature was approaching a mixed temperature everywhere in the flow. Additionally, at the interface of the jets, large temperature fluctuations were measured. Moreover, the temperature fluctuation intensity was larger for the isovelocity case than the non-isovelocity case. Axially, the largest temperature fluctuation intensities coincided with the center of the cold jet, at approximately 5 diameters downstream.

Continuing this work using the same experimental setup, Kimura et al. [18] investigated frequency content of the temperature profile for use in turbulence models. The data collected was

compared to numerical models based on unsteady Reynolds averaged Navier-Stokes (uRANS), low Reynolds number turbulence stress and heat flux model (LRSFM), and quasi-direct numerical simulation (DNS). The DNS accurately predicted temperature profiles and fluctuation intensities everywhere in the flow, while the LRSFM and uRANS models normally underestimated the fluctuation intensity in the flow, as well as overestimated temperature at some locations. When estimating temperature fluctuations in the flow, only the DNS model accurately predicted the frequency content of the fluid. This work was further expanded by Kimura et al. [19], in 2007. While this body of work was well conducted, the range of the experiments is very limited. For the water experiments, the largest velocity ratio studied between the cold jet and the hot jet was only 1 (i.e., the hot jet was always at a higher velocity). Similarly, the maximum temperature difference between the hot and cold jet studied was only 40°C. For the VHTR lower plenum, this can be as high as 300°C [2,3].

A 2007 study by Choi and Kim [20] further evaluated turbulence models for thermal striping in a triple-jet. A two-layer model, a shear stress transport model, and an elliptic relaxation model for turbulence were compared to experimental data. From the test, the elliptic relaxation model was the only model capable of predicting the oscillatory behavior of the jets, as well as the time averaged temperature and temperature fluctuation intensity. However, all three models predicted slower downstream mixing than was experimentally measured. It is worth nothing, a Power Spectral Density (PSD) of the temperature time history showed prominent frequencies around 22 Hz and 60 Hz in the planar triple-jet experiment.

Many of the high quality studies mentioned focus on slot jet geometries. For the VHTR lower plenum, round jet studies are more applicable. When reviewing literature for arrays of round jets, three predominant works were found which most closely pertain to the body of work

contained in this thesis. Two sets of analytical work [21, 22] attempted to quantify the mixing behavior of twin round jets. Knystautas [21] studied closely spaced circular jets ($S/D_{jet} = 1.5$, $Re_{jet} = 44,000$) to determine if sufficiently far downstream the flow field could be treated as two-dimensional. However, detailed measurement of the jet inlet profiles or discussion of flow conditioning was not given. Additionally, no investigation is given into the effects of various flow variables on the flow field observed [21]. Pani and Dash [22] investigated centerline decay rates for the center jet in an array based on the number of round jets in the array ($S/D_{jet} = 1.5, 3.0$) and as a function of the jet shape. While several analytically derived profiles are presented there is no investigation into the near field of the jet, the area of most interest for the lower plenum. More in depth experimental work was conducted by Harima and Osaka looking at mixing processes in twin jets. Investigating three different jet spacings, $S/D_{jet} = 2, 4$, and 8 , the mean flow profiles were presented for $x/D_{jet} > 5$. Work was done to quantify the combining or necking of the jets as well as discussion of the combining of the jets [23]. A more recent study looked at the differences between a row of confluent round jets and a square array. For the row of jets study, the jet spacing was $S/D_{jet} = 2.82$. PIV and LDA measurements were compared to RANS simulations utilizing both the $k-\varepsilon$ turbulence model and an RSM simulation. Specific care and concern was given to identifying the merging point and combining point of the jet [24]. For current work the merging point is defined as the axial distance where the negative recirculating region between two jets becomes positive. At this location the two jets begin to behave as a single jet. The combining point is defined as the axial location at which the maximum velocity occurs on the symmetry plane between neighboring jets. At this location velocity profiles in the twin jet begin to resemble those for a single jet.

While much work has been conducted investigating thermal striping, several key limitations exist in the previous studies. First, while much has been done investigating slot-jets, studies are scarce for arrays of round jets such as those seen in the lower plenum. Furthermore, the current body of work has only investigated for a limited range of jet Reynolds numbers, velocity ratios, and temperature differences, none of which accurately represent those expected in the VHTR lower plenum. Also missing from the current work is the effect on flow condition, specifically velocity inlet profile and turbulent intensity profiles on the mixing of jets. In order to address these limitations and provide data more application to VHTR lower plenum flows, the current research focuses on round jet configurations where mixing between neighboring jets is examined both experimentally and computationally. Specifically, a round triple-jet facility is designed and built to quantify the dependence of the mixing parameters on factors including Reynolds number, temperature difference, and jet spacing. These relationships are evaluated from the near field to intermediate downstream locations. The facility design can also accommodate more complex studies, including a unit cell geometry which consists of seven support post and six round jets in a crossflow designed to emulate the VHTR.

An in depth scaling analysis of the VHTR lower plenum is conducted and used as motivation in the design of the unit cell facility. The unit cell facility represents an impinging jet array combined with flow across a tube bundle. Detailed expectations are laid out comparing the lower plenum flow to what will be recreated in the experimental facility. Additionally to better study mixing in jets an experiment with a parallel, round triple-jet, the experimental will be carried out to see how unique flow variables, namely Reynolds number and temperature difference, and geometric variables such as the jet spacing effect the flow field in the near field of the jets. In order to contribute to the current body of work, several triple-jet simulations are

proposed with the goal of investigating the ranges at which different variables effect the turbulent mixing.

The main contribution of the current work is an investigation of new fundamental mixing for closely spaced gas jets with a detailed investigation into what should be done to improve modeling capabilities. This, along with the unit cell studies, provide a much needed foundation for more applied modeling and experiments. Several key contributions are listed as follows:

- Development and error assessment of a method for Constant Temperature Anemometry in a non-isothermal flow
- Quantification of jet inlet profiles for mean velocity, turbulent kinetic energy, and turbulent intensity
- Qualitative assessment of thermal hydraulic development in a parallel triple-jet as a function of velocity ratio and temperature difference
- Qualitative assessment of the effects of inlet velocity profile on thermal hydraulic development in a parallel round triple-jet
- Comparison of realizable $k-\varepsilon$ and Launder Gibson RSM turbulence models for flow in a round parallel triple-jet

The remainder of the document is organized as follows: Section 2.0 describes the development of the experimental facility, including the flow skid (Section 2.1) and design of the unit cell experimental facility (Section 2.2), experimental results of which are beyond the scope of this thesis. Section 3.0 discusses the anemometry capabilities used to examine the velocity field while Sections 3.2 and 3.3 examine the mean and turbulent statistics for a single jet. Section 4.0 examines measurements made for the round parallel triple jet. Specific care is given to error introduced from various temperature correction techniques, and is discussed in Section 4.1.

Section 5.2 and 5.3 explain the steps necessary to overcome hurdles associated with numerical modeling of non-isothermal flows while results for the simulations are compared in Section 5.4. Finally Section 6.0 discusses the experimental and numerical needs for future validation of turbulence models.

2.0 DESIGN OF AN EXPERIMENTAL FACILITY

2.1 FLOW SKID DESIGN

In order to improve the current body of work on thermal striping, it was necessary to increase the range of variables considered in previous studies. Investigators at the Idaho National Laboratory (INL) [5-9,11,28] have performed numerous experimental studies aimed at characterizing the turbulence in the VHTR lower plenum. They have built a 6.55:1 scale model of a portion of the lower plenum enabling them to study the isothermal turbulent mixing between multiple jets. This scaled model used a jet diameter of 0.87 in (22.10 mm). In order to take advantage of standard tubing sizes, our facility utilizes a jet diameter of 0.875 in (19.1 mm). The goal of the experimental setup was to create three simultaneous flows capable of producing jet Reynolds numbers of at least 25,000. Although the setup can easily accommodate jets of different geometries (e.g., round, square, slot), the focus of the facility was round jets. Additionally, in order to expand upon previous experimental ranges in parallel triple-jet studies [17], the target for the maximum operating temperature of the facility was 150°C. For a 19.1 mm diameter air jet at a Reynolds number of 25,000 and temperature of 150°C, the jet velocity was 18.2 m/s. Since the facility is to be used for thermal striping investigations, it was determined that the temperature and velocity of each of the three jets should be independently controlled with a maximum ΔT between any two jets of 100°C. In order to determine a final design, an

iterative approach was utilized until agreement was found between the desired specifications and actual hardware specifications. Only the hardware utilized in the final design is considered here.

Shown in Figure 5 is a diagram illustrating the design of the experimental flow skid. This closed loop air handling system is driven by a variable speed blower (Model AT700 with 7.5HP motor and water cooling) which supplies the flow motivation for all three jets. A portion of the flow from the blower is taken from the main line and fed through a heat exchanger, whose cold side is supplied by the building chilled water lines. This flow channel constitutes the “cold” jet. The remainder of the flow in the main line is then split into two additional lines, each of which is then sent through individually controlled heaters. These two channels of flow constitute the two hot jets. Pressure drop across an orifice plate is used in each of the three flow channels (two hot jets and one cold jet) to monitor the individual flow rates. All the flow entering the test section does so through one of these three jets, each of which has a honeycomb flow straightener upstream of the test section as shown. The design of the honeycomb flow straighteners is discussed in detail in Section 3.1.1. Exiting the test section is a single line which returns the mixed flow back to the blower. An additional heat exchanger is placed after the test section before the blower in order to account for any heat gained in the flow from the blower itself. This provides a solution for scenarios where the desired jet temperature is only slightly above ambient conditions, where the heat imparted to the flow by the blower may become significant. Finally, there is a bypass line in parallel with the flow through the blower and system heat exchanger which can vary between completely closed and completely open, to accommodate low mass flow rate experiments. Actuated valves for each of three flow channels along with a fourth in the bypass line allow independent control of the flow rate for each jet. A pressure relief valve

designed for 20100 Pa ensures the pressure in the flow loop does not exceed acceptable limits for the blower.

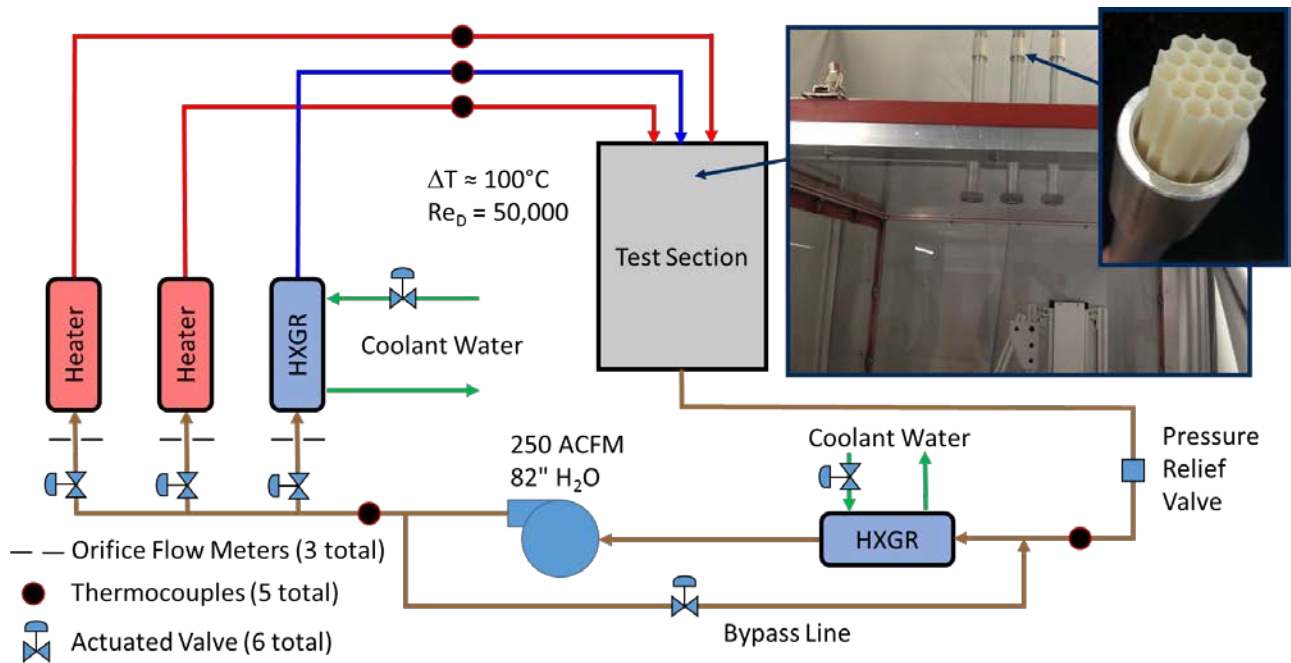


Figure 5 - Schematic of the experimental test section with honeycomb flow conditioners pictured

The test section is utilized in both single and triple-jet experiments via a removable spacing plate, as shown in Figure 6. The test section has dimensions of 813 mm × 813 mm × 1016 mm and is made from a high temperature polycarbonate material, LEXAN®. LEXAN® is optically transparent so that Particle Image Velocimetry (PIV) can be accommodated for full field velocity measurements (although PIV is not considered in this work). The test section was designed such that it had a removable door for easy access to any internal measurement equipment. On this door special consideration was given for mounting of an Infrared-Viewport (FLIR IRW-4C) for use with IR camera (FLIR SC5000) measurements (not considered in the present work). Internally, an 8020 aluminum extrusion frame is used for supporting any test

equipment, as well as the 3-Axis, high temperature, linear stages (not shown in the figure) supplied by Parker Hannifan Inc. The stages can travel 457 mm in the vertical direction, as well 254 mm in both horizontal directions. The setup was sealed using a high temperature rubber gasket. The test section was insulated using 1 in thick high density polystyrene with an R value of 0.241 K-m/W.

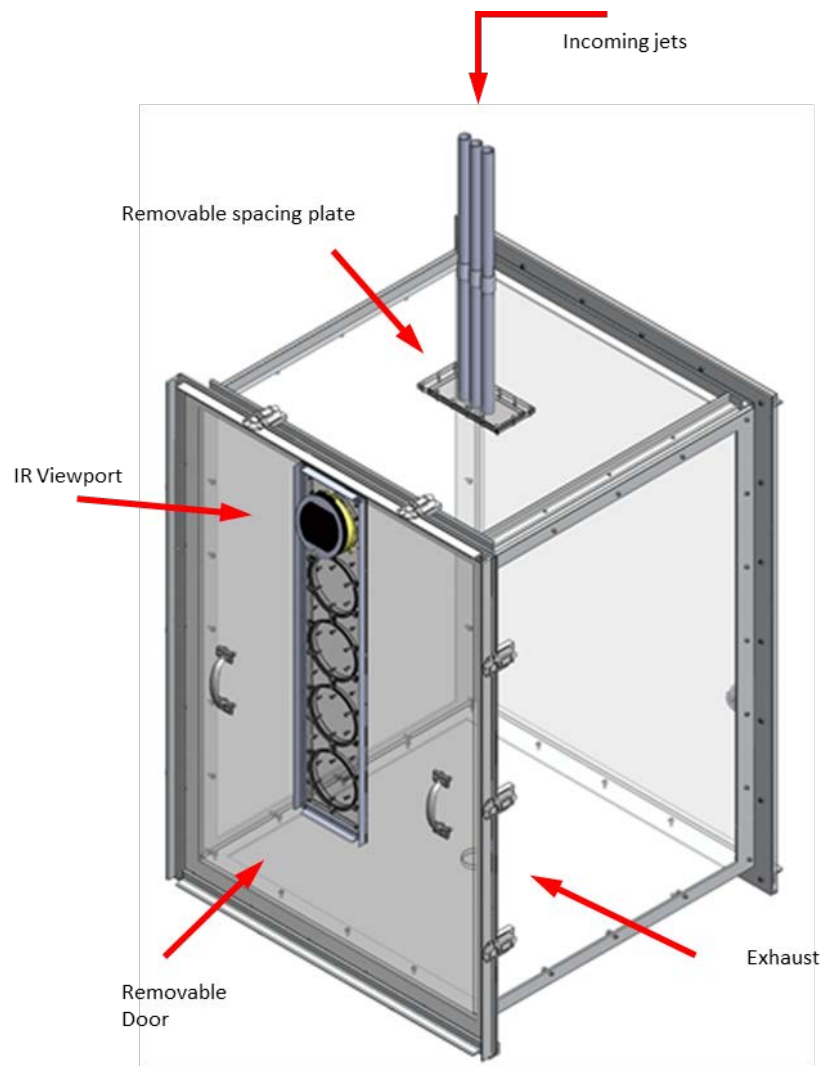


Figure 6 - Triple-jet experimental test section

2.1.1 Heater and Heat Exchanger Specifications

Although the designed apparatus is a closed loop system, conservative design principles were implemented by treating all components as once through. Since the heating elements for the two hot jets and the heat exchanger for the cold jet are fed with the same bulk temperature, their ability to increase or decrease the temperature of the fluid before it reaches the test section is

critical in meeting the overall test conditions desired. The upper and lower bounds for the operating temperature are 150°C (maximum temperature for certain measuring components in test section) and 25°C (temperature of building chilled water supply), respectively. The maximum desired temperature differential between hot and cold jets is $\Delta T = 100^\circ\text{C}$. For the two hot jet heaters, the air temperature is assumed to increase by up to 80°C in a single pass. For flow with a Reynolds number of 50,000, this suggests a mass flow rate of 0.0173 kg/s, the corresponding heating requirements can then easily be found according to the following expression:

$$Q = \dot{m}C_p\Delta T \quad (1)$$

where C_p is the heat capacity of the air (1070 J/(kg K), evaluated at 150°C). This results in 2.9 kW required for each hot jet. As a result, two inline 3 kW, screw plug, immersion heaters (custom manufactured by Wattco) are used. These heaters are 30 in long, with 0.403 in diameter sheath and a power density of $2.17 \times 10^4 \text{ W/m}^2$. The accuracy of the supplied control system is 0.1% of the user desired temperature.

The next component sourced was the heat exchanger for the cold jet. Here, in order to provide a conservative analysis, it was assumed that it should be able to create the desired temperature difference of 100°C without the aid of the hot jet heaters. It was assumed the exhaust temperature of the test section was equal to that of the hottest jet (150°C) and that no heat losses occur through the piping network leading up to entrance of the cold jet heat exchanger. The mass flow rate is the same as that considered during the hot jet analysis (0.0173 kg/s), and therefore dictates a heat removal of 3.69 kW (found using Equation (1)). For the water side of the heat exchanger, we take the inlet temperature to be 25°C (chilled water supply temperature) and outlet coolant temperature of 35°C to insure that in case of an accident, the risk

of being burned due to high fluid temperatures is minimal or non-existent. A shell and tube type heat exchanger (Southwest Thermal BOSCO AB1008-98500) can provide 4.19 kW of heat removal, well over the performance needed. The surface area on the tube side of the heat exchanger is 2.19 m².

A second heat exchanger (Southwest Thermal BOSCO AB705-98500) is used to cool the exhaust flow from the test section in order to remove any heat that may be imparted by the blower during continual operation. The maximum temperature difference for this heat exchanger was specified at 40°C with the total mass flow rate for the air including the two hot jet channels and single cold jet channel (total of 0.0519 kg/s). Calculating the heat removed, according to Equation (1), the total heat removed is 0.9 kW.

2.1.2 Blower Specifications

The final component sourced was the blower. The blower is the most important parameter for determining the flow rate, and subsequently the jet velocities, possible in the system. In order to determine the possible flow rates, a thorough estimation of the system pressure drop is necessary. However, before pressure drop can be accurately determined, the final piping configuration, which depends on the specific blower chosen, is needed. Here, we step through the calculations utilized when calculating the pressure drop. This pressure drop, along with the pump curve of the blower, was then used to calculate actual operating ranges. These predictions are experimentally verified in a later section. For the present study, only flow in a single jet, with the bypass completely closed, was considered.

Shown in Table 1 are the various diameters of pipe used in the flow skid. First, the primary pressure losses due to pipe length (ΔP) were calculated according to Equation (2),

where f is the friction factor, L is the length of the pipe, D is the pipe diameter, and U is the average velocity in the pipe. The friction factor, f , was iteratively calculated using the Colebrook Equation (see Equation (3)), which depends on the Reynolds number of the pipe, Re_{pipe} , and the surface roughness of the pipe, e (which is taken to be 0.045 mm).

$$\Delta P_{pipe} = f \rho \frac{L}{D} \frac{\langle |U| \rangle^2}{2} \quad (2)$$

$$\frac{1}{\sqrt{f}} = -2 \ln \left(\frac{e/D}{3.7} + \frac{2.51}{Re_{pipe} \sqrt{f}} \right) \quad (3)$$

Table 1 – Pipe Lengths and Diameters in flow skid

Diameter (in)	0.75	1	1	3	4
Length (in)	0	72	28	12	8

Similarly, the minor pressure losses, due to expansion and contraction between pipes of different sizes, were calculated. The minor losses (ΔP_{exp}) were calculated according to Equation (4), where the small and large diameters are d and D , respectively [25]. The average velocity is always calculated in the smaller pipe diameter, regardless of whether the change in pipe diameter is an expansion or contraction. Shown in Table 2 is the expansion/contraction ratio, $d:D$, and the number of each expansion/contraction in the current piping configuration being analyzed.

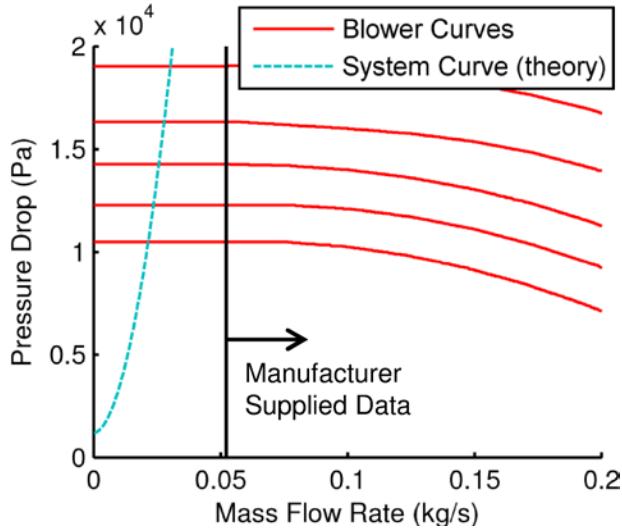
$$\Delta P_{exp} = \frac{1}{2} \left[1 - \left(\frac{d}{D} \right)^2 \right] \frac{\rho \langle |U| \rangle^2}{2} \quad (4)$$

Table 2 – Expansion and contraction ratios

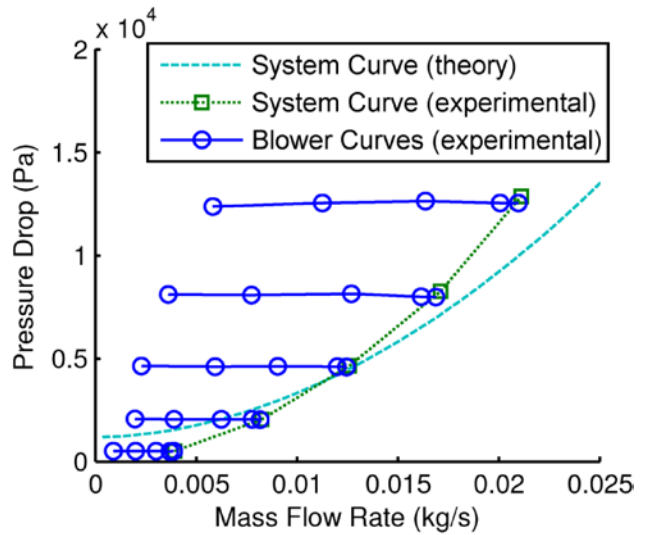
d:D (in:in)	Number
0.75:2	1
1:2	6
1:3	2
2:3	1
0.75:36	2

Finally, it was assumed the pressure drop across the system heat exchanger and the heater was 0.2 psi (1.4 kPa), as per manufacturer specifications. Although in reality, the actual pressure drop across the air side of the heat exchanger is dependent on the flow rate, this data was not available to include in the present analysis. This assumption causes the predicted system curve to have a non-zero pressure, even when the flow rate is set at zero. The blower selected is a Paxton AT700 centrifugal air blower. It is capable of producing 280 CFM (0.118 m³/s), at 3.035 psi (20.9 kPa). The blower is powered by a 7.5 HP Emerson Technologies motor, controlled by a GS2-27P5 variable frequency drive (Automation Direct). In order to calculate the achievable operating conditions, the blower curve must be analyzed in conjunction with the system curve. A family of blower curves supplied by the manufacturer is shown in Figure 7(a) along with the predicted system curve. As previously noted, the system curve intercepts the pressure axis at approximately 1.4 kPa (due to the constant pressure drop assumed for the heat exchanger). The presupplied specifications for the blower curves did not provide data below a certain flow rate, denoted by the vertical black line at approximately 0.052 kg/s. To the left of this line, a constant pressure drop is assumed.

In order to determine the accuracy of the predicted system curves, and validate the assumption in regard to the blower behavior at low flow rates, experimental measurements were taken. Only a single jet (cold jet channel) was used in an isothermal configuration (water side of heat exchanger was not operating). These experiments focused on acquiring portions of both the blower curves and system curves. The results are shown in Figure 7(b). The pressure drop across the blower was measured with a 0-2 psi (0-13.8 kPa) linear pressure transducer with an output current of 4-20 mA. The experiments were limited in that the pressure needed to remain below 2 psi to protect the transducer used. The mass flow rate through the system was measured by quantifying the pressure drop across the orifice plate using a linear pressure transducer (0-1 psi (6.9 kPa) with 4-20mA output). The system curve was collected by completely opening the control valve of the jet and increasing the horsepower to the blower. The blower curves were acquired by keeping the horsepower to the blower constant and adjusting the control valve of the jet, to increase system pressure drop. Five unique horsepower settings were considered, thereby generating 5 blower curves. Note that collecting data in this manner precludes characterizing the blower performance beyond the operating point (intersection of blower and system curves). Therefore, blower curve data was only captured to the left of the system curve. The assumption of constant pressure in this region seems to be validated. The predicted system curve is also included in Figure 7(b) for direct comparison with the experimental curve. Worth noting is that the pressure is under-predicted for reasonably high flow rates. This is likely due to the fact that head losses for the entire piping network are not known with an extremely high level of confidence.



(a)



(b)

Figure 7 – (a) Plot of predicted system curve with the manufacturer supplied blower curves. (b) Experimentally measured system curves and blower curve

2.1.3 Uncertainty of Mass Flow Rate

One important function considered in the design of the experimental setup was the ability to control the flow rate, and thereby be able to dial in a specific jet Reynolds number. The ability to do this is closely tied to the uncertainty of the mass flow rate. As previously discussed, the mass flow rate is determined from the differential pressure drop across an orifice plate. The mass flow rate of a compressible fluid, traveling through an orifice plate, can be calculated according to Equation (5), where the isentropic expansion factor (Y) is defined in Equation (6), where C_D is the discharge coefficient for the selected orifice plate, D_o is the orifice plate diameter, D_{pipe} is the internal diameter of the 2 in (50.8 mm) NPT piping leading to the orifice plate, T_o is the temperature at the inlet of the orifice, P_o is the absolute pressure at the orifice inlet, ΔP is the pressure drop across the orifice, and γ is the specific heat ratio.

$$\dot{m} = \sqrt{\frac{RT_o Z}{P_o}} \frac{D_o^2 \pi}{4} \frac{C_D}{\sqrt{1 - \frac{D_o^4}{D_{pipe}^4}}} \sqrt{\Delta P} Y \quad (5)$$

$$Y = \sqrt{\left(\frac{P_o - \Delta P}{P_o} \right)^{2/\gamma} \left(\frac{\gamma}{\gamma - 1} \right) \left(\frac{1 - \left(\frac{P_o - \Delta P}{P_o} \right)^{\frac{\gamma-1}{\gamma}}}{1 - \left(\frac{P_o - \Delta P}{P_o} \right)} \right) \left(\frac{1 - \frac{D_o^4}{D_{pipe}^4}}{1 - \frac{D_o^4}{D_{pipe}^4} \left(\frac{P_o - \Delta P}{P_o} \right)} \right)} \quad (6)$$

Shown in Table 3 are the assumed values for each parameter, as well as their respective uncertainties. Using these values, the uncertainty of the actual mass flow measurement was calculated using standard propagation of uncertainty analysis [25]. Accordingly, in order to maintain an average jet velocity of 15 m/s at 27°C, corresponding to a jet Reynolds number of 20.6×10^3 , the mass flow rate is 6.437×10^{-3} kg/s, and the pressure drop across the orifice plate is 0.024 psi. This corresponds to an uncertainty in mass flow rate of 0.305%. Similar calculations were carried out assuming the gas was incompressible, meaning that the isentropic expansion factor was equal to a value of 1. Assuming the gas was incompressible, the uncertainty in the mass flow rate is $4.5 \times 10^{-4}\%$ different from that when the isentropic expansion factor was solved for. Since this change is three orders of magnitude less than the calculated uncertainty the incompressible flow assumption is applied to reduce the complexity of uncertainty calculation. For the extreme case, where the Reynolds number is 25×10^3 , corresponding to an average jet velocity of 18.25 m/s and a mass flow rate of 7.831×10^{-3} kg/s at a temperature of 27°C, and a pressure drop across the orifice of 0.036 psi, the uncertainty for the compressible mass flow rate was 0.273%.

Table 3 - Assumed values and uncertainties

	Value	Uncertainty
D_o (in)	1.0231	0.001
D_{pipe} (in)	2.067	0.001
T_o (K)	293.15	0.1
P_o (psi)	17	0.025
ΔP (psi)	0.036	$9 \cdot 10^{-5}$
γ (1)	1.389	0.01

Shown in Figure 8 is a plot of the total uncertainty of the mass flow rate, as well as for each of the terms necessary in calculating the total uncertainty. As shown, the most significant contribution to the overall uncertainty in mass flow rate comes from the uncertainty associated with measuring the pressure drop across the orifice plate. Since the uncertainty in this pressure measurement is a constant value, its influence on the overall uncertainty diminishes as the flow rate increases. At sufficiently high flow rates, the overall uncertainty becomes nearly constant (approximately 0.27%). For these calculations the orifice pressure drop transducers were a 0-0.249 kPa high accuracy ($\pm 0.25\%$ FS) Setra Model 2461 pressure transducer with 4-20 mA output. These pressure transducers are used in the remainder of this work.

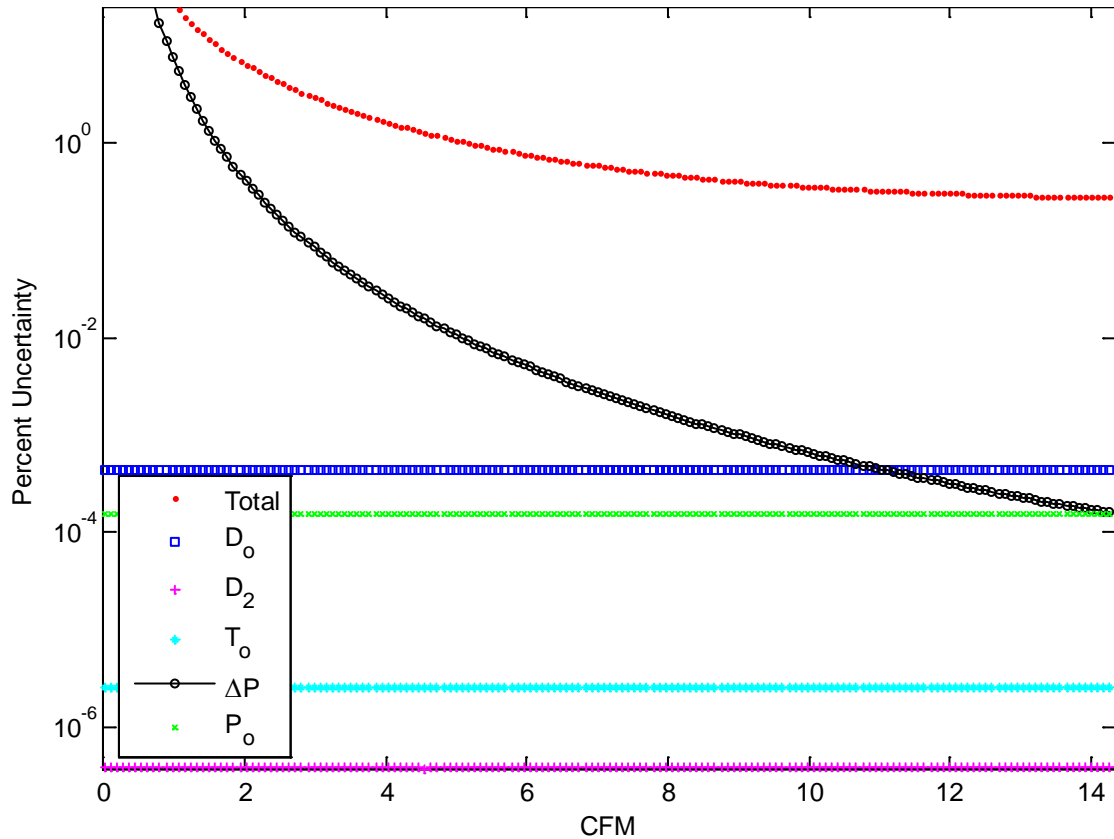


Figure 8 - Percent uncertainty of mass flow rate and individual uncertainty components

2.1.4 Control of Mass Flow Rate

The mass flow rate is measured utilizing an orifice flow plate and controlled via electronically actuated valves, Belimo model AFB-24-SR with 2-10 V input. The valves were controlled utilizing a Koyo DirecLogic 06 PLC (D0-06DD2) with signal I/O utilizing three unique DAQ cards (F0-04AD-1, F0-08ADH-1, F0-08DAH-1). In order to implement real time control of the mass flow rate, the pressure drop across the orifice plate was gathered and used in Equation (5). In Equation (5), the isentropic expansion factor Y is replaced with the empirical value Y_{exp} , shown in Equation (7). Note that the discharge coefficient C_d is found from interpolation of experimental data and is performed utilizing a table look up based on β and the orifice Reynolds

number. During all calculations geometric parameters such as orifice diameter are corrected to account for thermal expansion due to the increased temperature. For a more detailed explanation of the calculation of flow rate across an orifice plate, including explanation for the empirical fit of the isentropic expansion factor and the discharge coefficient, see [26].

$$Y_{\text{exp}} = 1 - \frac{0.41 + 0.35\beta^4}{\gamma} \frac{\Delta P_o}{P_o} \quad (7)$$

2.2 UNIT CELL EXPERIMENTAL DESIGN

2.2.1 Design of a Unit Cell Experiment

Although the facility is primarily used for triple-jet studies in the present work, design modifications were made in order to also evaluate physics more closely tied to the actual VHTR lower plenum. This is done by designing a unit cell test section, one that represents a portion of the lower plenum, complete with supports posts. A half model of the lower plenum [27] is shown in Figure 9. As previously noted, the jets and posts combine to create a complex flow field that is a combination of many canonical problems, including impinging jets, jet arrays, jets issuing into cross flow, and flow past tube bundles. Several studies have been conducted which specifically investigated turbulent mixing and thermal striping in the lower plenum of the VHTR. However, for all these studies, the typical experimental domain is that originally designed by INL and used in their Matched Index of Refraction (MIR) Facility [5,11,28], shown in Figure 10 [27]. This facility was designed based on an in-depth scaling analysis, and therefore generates conditions in the same range of key dimensionless parameters when compared to the full scale VHTR design. In the years that followed its construction, this facility became somewhat of a canonical VHTR-

related configuration, with multiple research group performing relevant experimental and computational studies. The MIR facility, by definition, requires mineral oil as its working fluid and must be kept within a reasonably tight temperature window in order to maintain the transparent fluid solid interfaces. As a result, non-isothermal studies are precluded. In addition, the model is meant to mimic a slice of the lower plenum near the line of symmetry in Figure 10, and therefore cannot be used to investigate interactions between more than two neighboring jets. Additional scaling studies have been conducted by Oregon State University [29] and Texas A & M University [30], both of which were considered when designing the lower plenum model for use in conjunction with the present facility investigated in the present body of work.

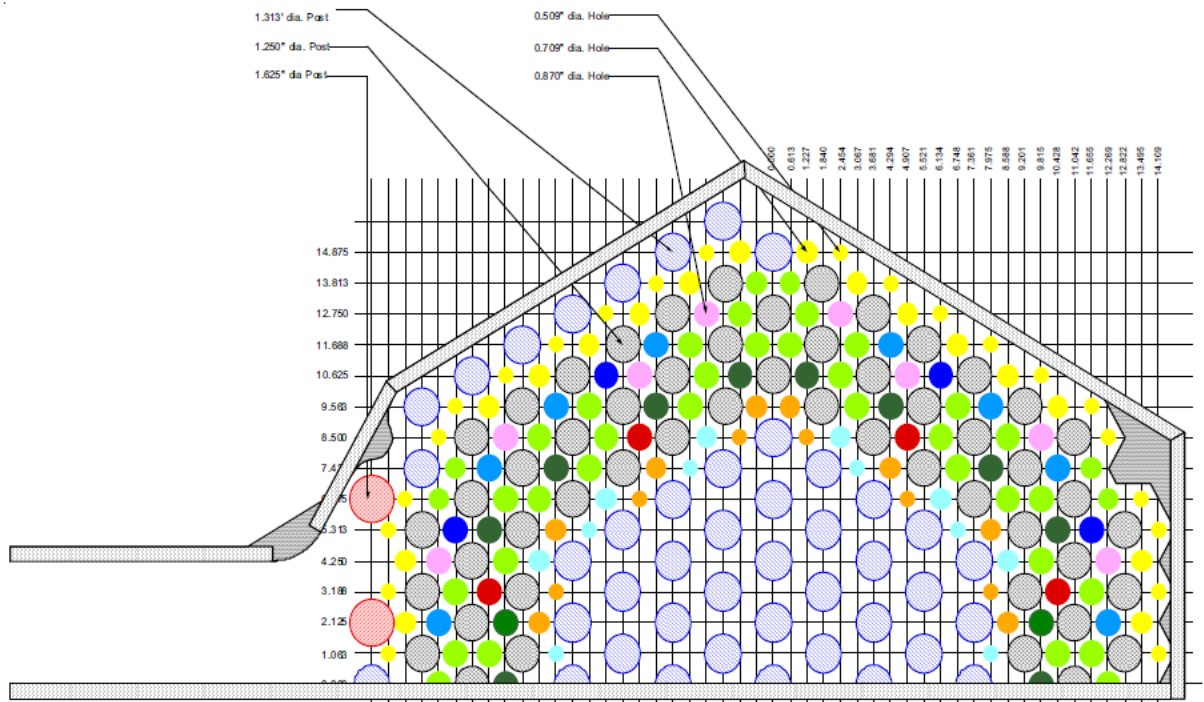


Figure 9 – Half Model of the VHTR lower plenum with jets (colored) and posts (grey) [27]

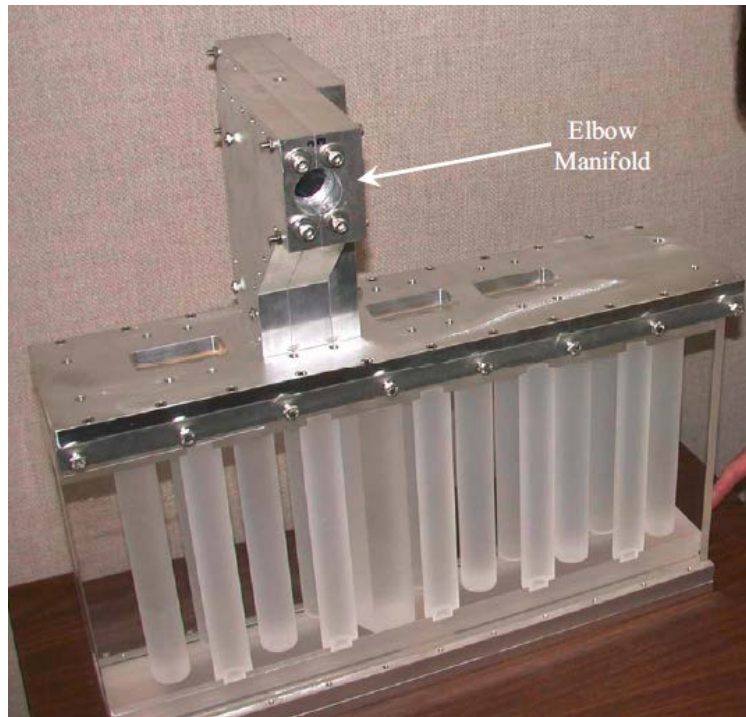


Figure 10 – Matched index of refraction facility test section at INL [27]

2.2.2 Scaling and Experimental Measurements in the Unit Cell Design

In order to expand upon current studies related to isothermal and non-isothermal flows in the lower plenum, an experimental facility is designed to enable high quality data collection for future validation studies. A repeating flow configuration, referred to as the unit cell is the focus of this experimental facility, and consists of six jets arranged in a hexagonal pattern whose flow enters the test section with the dominant flow direction along the length of the seven cylindrical support posts. This flow is then met by an orthogonal crossflow. This is illustrated in Figure 11, and focuses on three unique configurations of the flow in the half model of the VHTR lower plenum labeled case A, B, and C. By adjusting the velocities and temperatures of the six jets and the strength and temperature of the crossflow, different regions of the lower plenum can be

experimentally simulated. Each of the cases have unique flow features that are considered during the design. Case C represents a unit cell far away from the outlet of the lower plenum. For this case the cross flow velocity and temperature are very low. Assuming Gaussian shaped temperature and/or velocity profiles in the radial direction, one could assume two unique jet temperatures and flow rates (designated by the numbers 1 and 2 shown on the jets). Geometrically, case C is similar to case A as both represent flow across staggered tube bundle. However in case A, which is near the outlet, the cross flow velocity and temperature as predicted via Figure 2 and Figure 3 are much larger than in case C. Case B then represents a unit cell near the periphery of the lower plenum. In this case there is a low cross flow velocity and temperature, however the orientation with respect to the cross flow is more closely represented by that of an inline tube bundle. For this case, three unique jet temperatures would exist, as depicted by the numbers 1, 2, and 3.

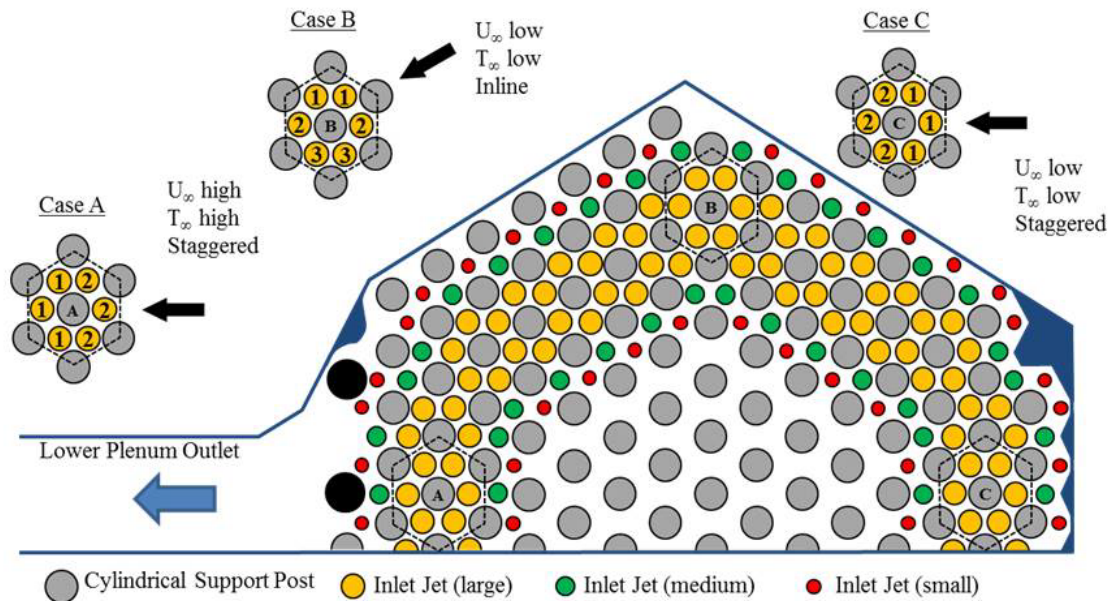


Figure 11 – Experimental unit cell for studying the lower plenum of the VHTR

Before examining the three unit cell cases detailed in Figure 11, the extensive VHTR lower plenum scaling studies conducted by INL [5-8,11] were reviewed. As explained by Condie et al. [11] based on expected Richardson numbers it is reasonable to assume that during full power operation the jets in the lower plenum are momentum-driven with negligible buoyancy effects. Based on the preliminary simulations conducted by Mazumdar et al [4], scaling of the lower plenum was further investigated. In the lower plenum, jet Reynolds numbers vary from 10^3 to 10^5 , while the transverse Reynolds number, calculated based on the cross flow velocity and jet diameter, can be as large as 51,000 assuming a maximum crossflow velocity of 70 m/s. In areas with large transverse velocities (~ 50 m/s) the transverse velocity ratio ($R = V_{\text{jet}}/V_{\text{trans}}$) can be less than one half. For locations with minimal transverse flow near the edges of the plenum, transverse velocity ratio can be very large (~ 70 based on a maximum jet velocity of 148 m/s [4]). However, typical of the majority of the jets in the lower plenum is a transverse velocity ratio between 0.5-5. Similarly, in the lower plenum, post Reynolds numbers reach 70,000 with shedding frequencies of approximately 60 Hz, based on a Strouhal number of 0.2. For a detailed description of non-dimensionalization and scaling in fluid flows the reader is suggested to see [31].

Design of the facility is achieved using standard scaling requirements for matching many non-dimensional parameters in the VHTR lower plenum including jet Reynolds number, post Reynolds number and vortex shedding frequency, transverse Reynolds number, and plenum Reynolds number, as well as maintaining geometric similarity. The MIR facility designed at INL to study turbulent mixing in the VHTR lower plenum utilized a 6.55:1 scale model [5-9,11,28], which resulted in a jet diameter of 22.10 mm. For our current work, a scaling of 6.598:1 was selected such that standard tubing sizes 22.23 mm (0.875 in) could be used. Based on this same

scaling, the post diameter was 31.75 mm, with a length of 219.7 mm, which also represents the scaled plenum height.

Utilizing the previously designed flow motivation skid, the maximum achievable Reynolds number in a single experimental jet is approximately 74,000, while the maximum achievable jet Reynolds number when all six jets are run at equal flow rates, is approximately 36,000. In order to motivate the cross flow, an axial fan capable of producing jet to cross flow velocity ratios of 0.5-5, typical of what is experienced in the lower plenum, is used. The specified axial fan described in Section 2.2.3 can motivate nearly 15,000 cfm of air in the setup, yielding a maximum Reynolds number based on the test section's hydraulic diameter of approximately $1.32 \cdot 10^6$. The maximum transverse Reynolds number achievable in the facility is about 100,000. Similarly, the maximum achievable post Reynolds number in the facility is approximately 140,000 with a vortex shedding frequency of 440 Hz. The maximum temperature difference in the unit cell experiment is the same as the maximum producible in the flow skid (i.e., $\Delta T = 100$ K).

After addressing desired flow requirements for scaling of the experiment, concern was given to what temperature and velocity measurements were both possible and desired. PIV measurements were determined to be a sufficient method of capturing the velocity fields. Olive oil was chosen as the seeder particle for this application. The TSI Six-Jet Atomizer 9306 was chosen as the dispersion method for the seeding material and is capable of injecting particles with a flow rate of 2.4 L/hr per jet. Olive oil is dispersed at a particle size range of 0.1 to 2.0 μm with a 0.3 μm mean diameter, and a concentration of 10^7 particles/ cm^3 . The insertion point in the wind tunnel, where the atomizer will be connected, is located upstream of the fan. To ensure a mass balance in the system, an exit will also be cut out of the ducting which will then reconnect

to the flow motivation skid. It was determined that to have a seeding density of 20% by volume of the wind tunnel, the atomizer will need to run for just under 2 hours. This is an over estimate of the amount of seeder particle needed in the system, and the true amount required will need to be determined empirically. With the mean diameter of 0.3 μm , the olive oil seeder particles will stay buoyant in the closed loop wind tunnel even without the cross flow being generated. This implies that the seeder injection will only need to be performed once over an extended period of time.

A CAD model of the unit cell design is shown in Figure 12. There are several key features apparent. First, issuing top-down into the test section are the pipe jets. Each of these pipe jets contains, within its' length, a high temperature ceramic honeycomb which helps straighten the flow. These honeycombs, and their effect on the flow, are addressed in detail in Section 3.0. Second, moving downward into test section, through the top plate, are the seven support posts, six in a hexagonal array with one center post. The rectangular shaped test section is 219.7 mm high (fixed by the length of the cylindrical support posts) and 457 mm (81 in) wide (direction orthogonal to the incoming crossflow). This width is approximately 2.5 times the width of the hexagonal array in order to remove interaction with the flow near the cylinders and the side walls of the test section. The length of the test section is 610 mm.

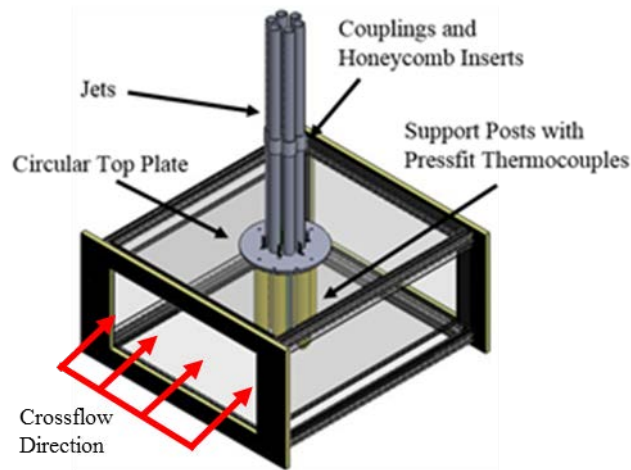


Figure 12 - Isometric view of the test section with key design components highlighted

PIV measurements are sufficient in capturing the velocity fields, but the temperature maps of flow are a significant challenge. The thermal mixing effects for this scenario will primarily be quantified from the temperature attenuation through the support cylinders. In order to measure the attenuation of temperature fluctuations in the posts, four thermocouples were placed in each of the six outer posts, and aligned radially towards the center post. Additionally, four thermocouples were placed in the center post. The outer 6 posts remain fixed in space, but the center post will be attached to a stepper motor enabling rotation. This is done in order to capture an azimuthal map of the temperature fluctuations in the center post, without the need to fill the post with a large amount of thermocouples. The thermocouples are inserted into each post from the top flat surface of the cylinder. The insertion depth for two of the thermocouples is 2.16 in ($L/D = 0.25$), while the insertion depth for the other two thermocouples is 4.33 in ($L/D = 0.5$). These four thermocouples are also located at different radial positions within the cylinder, namely $r/D = 0.131$ and 0.369 for the thermocouples with $L/D = 0.25$, and $r/D = 0.231$ and 0.469 for the $L/D = 0.5$ thermocouples. This is illustrated in Figure 13. In order to achieve accurate location of the thermocouples, a “press fit insert” was designed, to overcome machining limitations associated with large aspect ratio holes.

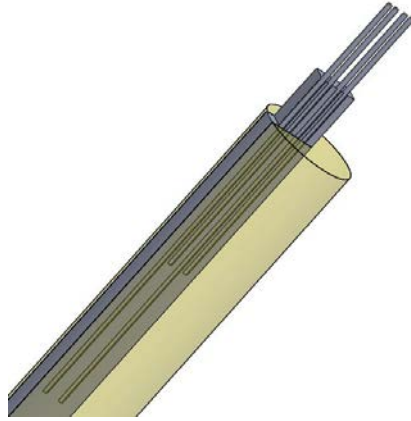


Figure 13 - Thermocouple/Support post assembly with thermocouples shown

2.2.3 Implementation and Fabrication of the Unit Cell Design

After appropriately identifying the functional requirements for the test section, and addressing design issues with the desired measurements, the next major concern was cross flow conditioning. In order to take consistent, meaningful velocity measurements, it was desirable to have an easily quantifiable, near uniform cross flow past the unit cell. In order to achieve this, standard wind tunnel design methodology was employed. From previous scaling in Section 2.2.2, it was desired to have a minimum transverse velocity ratio of 0.15 between the cross flow velocity and the jet velocity. In order to create sufficient cross flow velocities to maintain a low transverse velocity ratio ($R = 0.15$) when all six jets are operating with a jet Reynolds numbers of 10,900 at 27°C, a crossflow flowrate of 5.2 m³/s was necessary. Accordingly, after developing analytical models for the system pressure drop curves, the Greenheck mixed flow fan (model QEI-22-I-50) was selected. The QEI-22-I-50 provides a flow rate of 5.7 m³/s overcoming up to 124.4 Pa (0.5 inH₂O) pressure drop, while the maximum possible volumetric flow rate is 7.04 m³/s. The fan itself has a diameter of 0.78 m requiring that custom round-to-square transitions be fabricated to mate the fan to the rectangular 0.91 m x 0.61 m ducting.

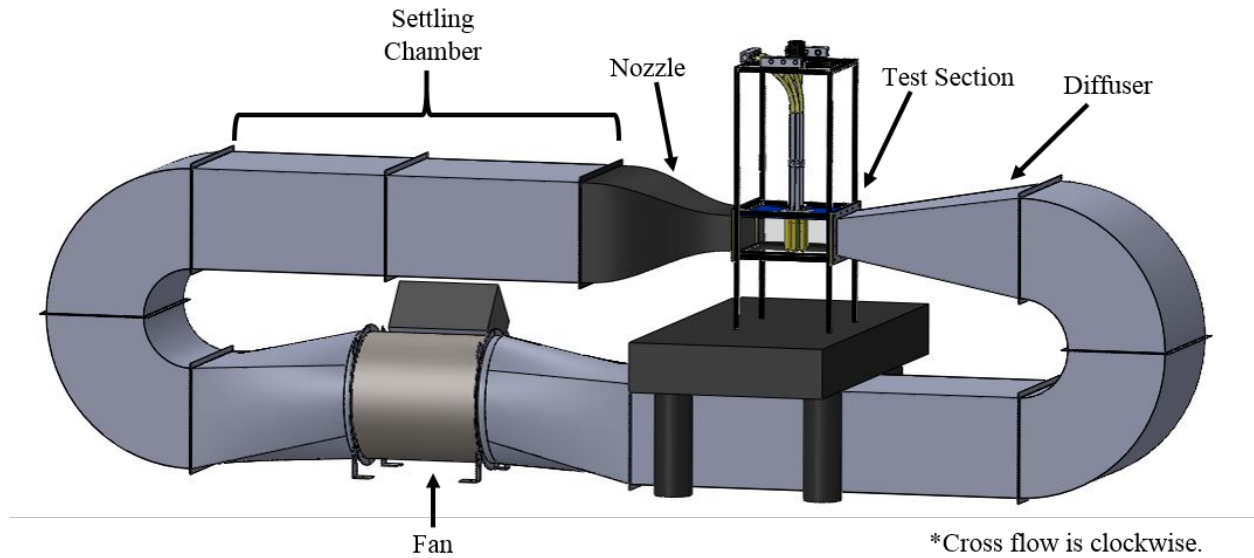


Figure 14 – Cross flow wind tunnel design

The next component of the recirculating wind tunnel is the settling chamber. The effective length of the settling chamber was limited by the available lab space. The effective length is therefore 2.4 m long. In this length, flow straightening devices were utilized to help straighten and allow for better control of the turbulent intensity distribution in the flow. Two aluminum hexagonal honeycomb inserts were utilized to aid in reducing large scale structures such as swirl from the flow as well as lateral mean velocity variations. A stainless steel wire mesh screen was incorporated to make the flow velocity more uniform. The design of the honeycomb and wire mesh was done in accordance with studies presented by Metha [32] and Scheiman [33]. The screen selected had a wire diameter of 1.37 mm with a spacing of 3x3 wires per square inch. The open area ratio for the screen was approximately 0.702, resulting in a pressure drop coefficient of 0.339 [34]. The screen was placed directly on the exit of the downstream honeycomb insert. Similar design was done for the honeycomb flow straighteners. Based on these sources, a honeycomb hydraulic diameter of 25.4 mm was selected, with a total

length of $L/D_{hyd} = 6$. The honeycomb inserts were placed at the entrance and exit of the settling chamber.

Following downstream of the settling chamber is the nozzle. The contraction nozzle, whose shape was determined following guidelines described by Bell and Metha [34,35], was designed to achieve a uniform cross flow by reducing both the mean and fluctuating velocity variations to a smaller fraction of the average velocity while simultaneously eliminating flow separation and reducing Moffatt eddies in the corners. The curve of the nozzle consists of a fifth order polynomial shown in Equation (8). For the horizontal contraction dimensions, the inlet radius, H_i , was 0.457 m while the outlet radius, H_e , was 0.229 m. For the vertical dimensions of the contraction, the inlet radius was 12 in while the outlet radius was approximated as 0.108 m. The total length of the contraction, L , was 0.91 m. The nozzle design has a contraction ratio, defined as the ratio of inlet to outlet area, of 8.47. The nozzle which was constructed using 2 x 2 weave carbon fiber layups (from HEXCEL Composites [36]) is shown in Figure 14. The final nozzle design dictated the 0.91 m x 0.61 m cross section for flow approaching the nozzle.

$$y(x) = H_i - (H_i - H_e) \left[6 \left(\frac{x}{L} \right)^5 - 15 \left(\frac{x}{L} \right)^4 + 10 \left(\frac{x}{L} \right)^3 \right] \quad (8)$$

The next portion downstream of the nozzle is the test section. Several design parameters were incorporated with the test section to allow for accurate and relevant velocity and temperature measurements to be found with the proper scaled design. First, a closer look at the test section is presented in Figure 12. The first part of the test section are the jets which run vertically into the test section. Each of these jets contains two 0.305 m straight pipes with an inner diameter of 22.23 mm, and are connected with a custom made coupling. Inside each of the couplings is a high temperature ceramic honeycomb insert for flow straightening and improved uniform turbulence statistics. These honeycomb flow straighteners are composed of Somos ®

NanoTool with a glass transition temperature of 82°C and consist of $L/D_{hyd} = 20$. Design of the honeycomb flow straighteners is addressed later in Section 3.1.1. The jet array can be seen in Figure 15 (a) while an individual honeycomb flow straightener can be viewed with a transparent version of its jet in Figure 15 (b).

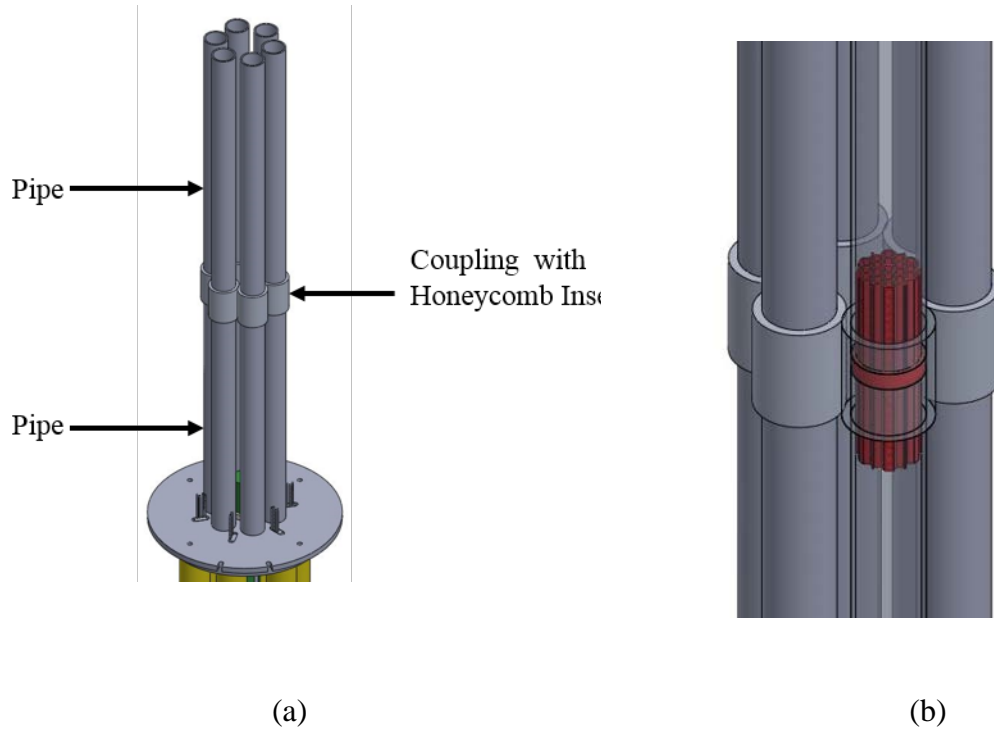


Figure 15: (a) Array of six jets located above test section (b) transparent jet revealing internal honeycomb insert

Also seen in Figure 12 is the circular aluminum top plate of the test section which holds the six hexagonal posts and the central support post. The top plate supports the jets, as well as aligns the outer support posts in the top wall of the test section. A more detailed view of the circular top plate with support posts, thermocouples, and jet inlets is shown in Figure 16. The aluminum circular plate locates each support post utilizing a four thermocouple press fit

assembly (described previously), with the exception of the rotating center post, which is secured with a press fit bushing. Additionally, the aluminum plate locates each jet in space. Finally, this aluminum plate was designed such that it can be rotated 30°, to accommodate flow across an inline tube bundle (case B in Figure 11) and a staggered tube bundle (cases A and C in Figure 11). In order to allow PIV measurements, the side walls and bottom plate were constructed from LEXAN®, a high temperature polycarbonate plastic that is optically transparent. Additionally, in order to reflect the laser sheet, which is inserted laterally through the sides into the test section, all posts were given a high accuracy mirror finish polish after being machined. The top wall was constructed from a high temperature, ultrahigh-molecular weight (UHMW) plastic.

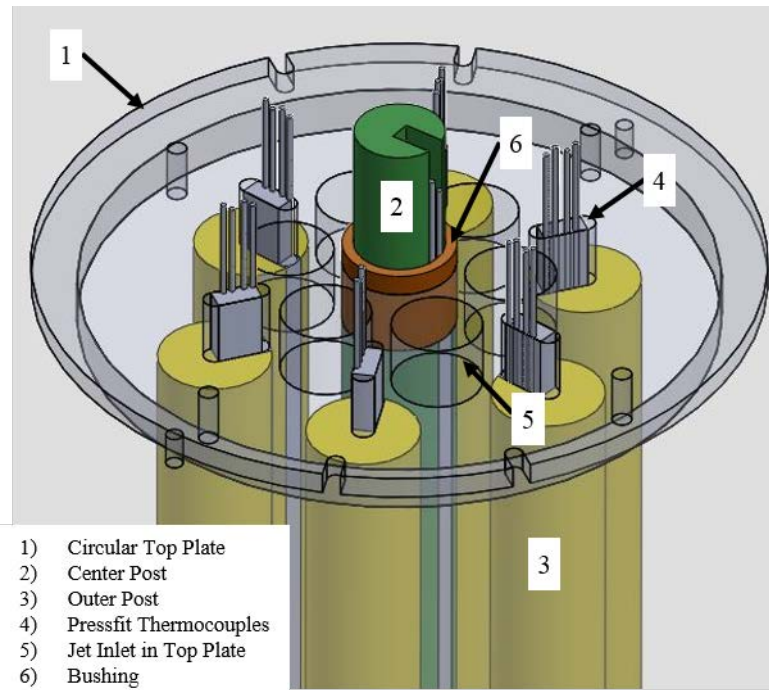


Figure 16: Transparent circular top plate with post configuration

Shown in Figure 17 are the manifolds used to connect the six jets to the flow motivation skid detailed in Section 2.1. This allows for up to three unique jet temperatures to be independently controlled, as is required for case B (Figure 11). Similarly, by utilizing just two

manifolds it is possible to have only two unique temperatures so that case A and C (Figure 11) can be studied. Flexible hosing will be used to connect the manifolds to each jet. Also shown in Figure 17 is the stepper motor. The stepper motor is connected via long shaft to the center post of the test section so that it can be rotated to allow for sampling radial temperature distributions at multiple azimuthal locations.

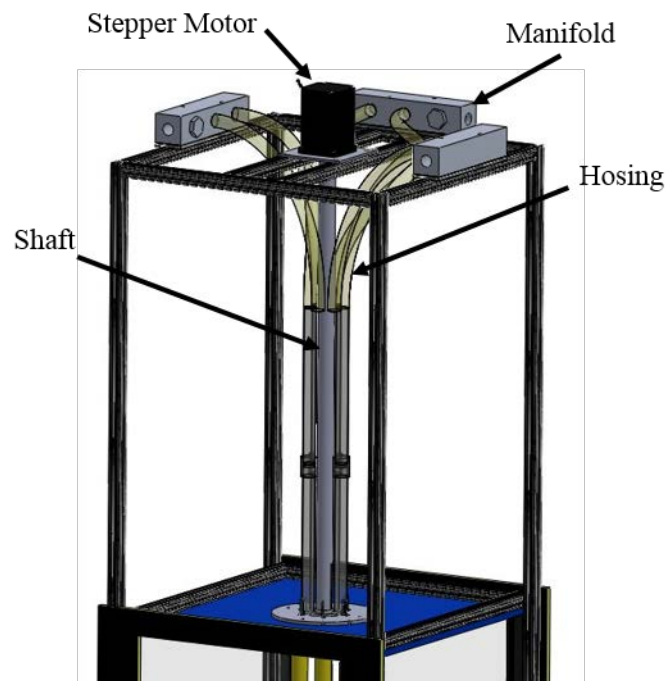


Figure 17: Stepper motor coupled to center post via a shaft

The last component designed was the diffuser. The diffuser design process was much simpler than that for the nozzle design since no flow conditioning characteristics need to be considered downstream of the test section. Therefore, a simple linear expansion was utilized to scale the ducting from the 0.61 m x 0.22 m cross section of the test section to that of the 0.91 m x 0.61 m ducting. For proper mating and convenient dimensioning, the diffuser is 1.22 m in length. The diffuser and the remainder of the ducting in the closed loop system, are all composed of stainless steel.

In addition to construction of the unit cell test section and cross flow conditioning setup, an ice-point reference facility has been built to act as a known temperature reference when measuring temperature with the thermocouples in the post, and is shown in Figure 18. The ice point is comprised of an ice bath placed in a refrigerator to increase the lifetime of the ice. The ice-point facility includes 30 type-T thermocouples, placed in the ice bath to act as reference junctions. In order to increase the ease of use, an input panel for type T measurement thermocouples equipped with mini-TC plugs is mounted to the side of the refrigerator. The facility uses a National Instruments TC-2095 32 Channel Thermocouple Connector, in conjunction with a SCXI-1102 32 Channel Thermocouple Amplifier, and SCXI-1600 USB Data Acquisition Module for gathering the thermocouple data. In experimental testing, the ice-point reference maintained $0^{\circ}\text{C} - 0.1^{\circ}\text{C}$ for 56 hours, monitored using a high accuracy RTD with built in alarm (Control Company, Thermometer, LCD, -2 to 2°C).

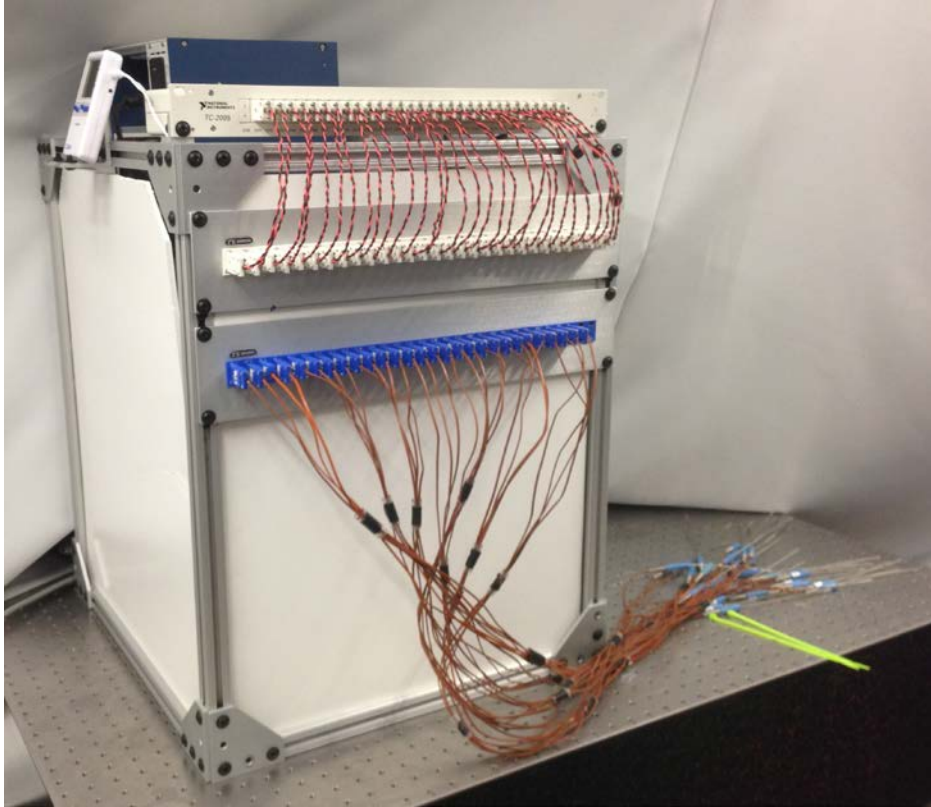


Figure 18 – Ice point facility

With the inclusion of the ice point facility, the unit cell experimental facility design and fabrication is complete. The experimental facility is capable of creating experiments for jets impinging jet arrays, jet array in cross flow, impinging jet in a crossflow, flow across a bank of cylinders, and the unit cell experiment. As currently constructed the unit cell experiment can accommodate up to six jets with Reynolds numbers ranging from 10,800 in the jets simultaneous, up to a maximum Reynolds number of 21,800 in a single jet. The cross flow volumetric flow rate can reach $7.02 \text{ m}^3/\text{s}$ for an average crossflow velocity of 70 m/s in the test section. For experimental measurements the test section has been made of optically transparent polycarbonate for use with PIV while thermocouples have been press fit in each post. Additionally an ice point reference facility has been constructed to aide with high accuracy thermocouple measurements.

3.0 CHARACTERIZATION OF JET FLOW BEHAVIOR

Special care was given to characterize the performance of a single jet before progressing to more complicated experiments. The “flow skid” previously described in Section 2.0 was used to create a single jet. The captured single jet behavior provides both inlet data for RANS simulations where both the mean velocity profile and kinetic energy profile are necessary to accurately capture trends in the jets. Furthermore, the single jet profiles provide a benchmark to which the triple jet inlet results can be compared and discussed.

3.1 EXPERIMENTAL APPROACH

In order to gather velocity measurements in the test section, a single-wire constant temperature anemometry (CTA) probe, Dantec Dynamics 55P16, was used. The CTA measurements are detailed in Section 3.1.1. In order for the probe to be able to transverse the test section, a 3-axis, high temperature, linear stage setup, supplied by Parker Hannifan Inc, was used. The stages can travel 18 inches in the vertical direction, as well 10 inches in both directions within the horizontal plane. The origin of the coordinate system in this study is the center of the nozzle of the jet (i.e., entry point to the test section). The positive x axis is along the downstream direction of the jet. The positive y axis is defined as the direction away from the flow skid. The positive z axis is defined according to standard right hand rule convention based on the x and y

axes. A sketch of the experimental test section, with stages included, is shown in Figure 19. This is a simplified illustration of the same test section previously shown in Figure 6.

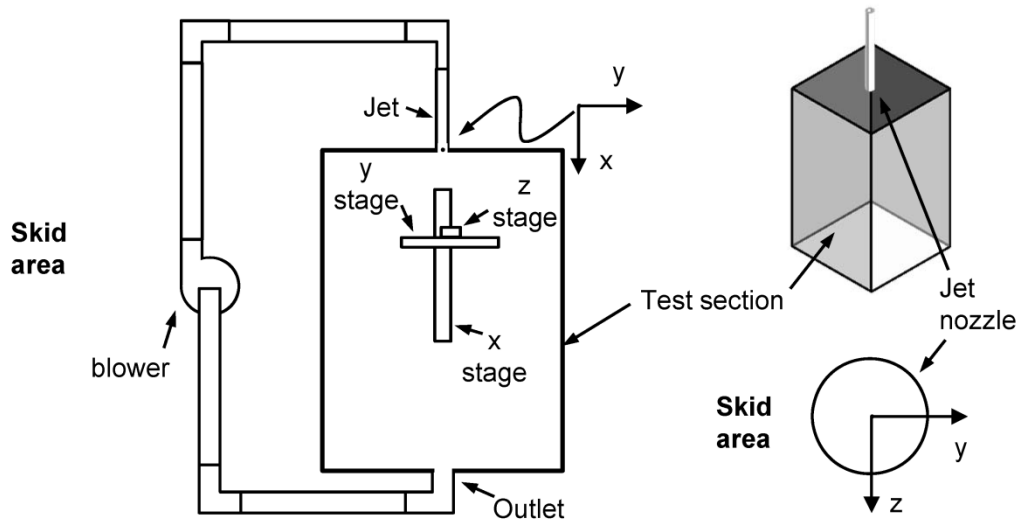


Figure 19 - Illustration of experimental facility for studies for single round

3.1.1 Flow Conditioning

It is desirable for experiments to have controlled, repeatable, and quantifiable conditions. Inability to meet these conditions can severely complicate quantifying and garnering new understanding into the physics involved. This is especially true when there are physical phenomena that are not yet understood. Some problems that need to be addressed in real flows are asymmetry, swirl, and non-uniform turbulent distribution. For the current work described here, special consideration is given to the first, asymmetry in the flow, with notes made regarding swirl and uniformity of turbulence. Shown in Figure 20(a) are velocity contours produced in the single jet experiment illustrated in Figure 19. In this case, only a straight pipe twenty hydraulic diameters (0.875 in) in length was used before the jet entered the test section.

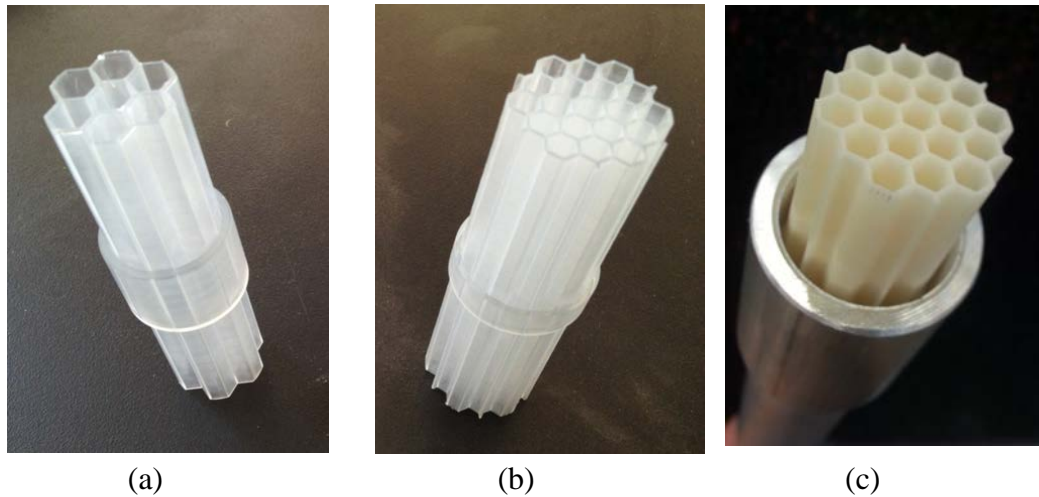


Figure 21 – (a) Coarse honeycomb (b) refined honeycomb
(c) ceramic honeycomb – shown in pipe coupling

The first attempted prototype honeycomb printed in Figure 21 (a), yielded the flow profiles seen in Figure 20 (b). The honeycomb was designed with a hydraulic diameter of 0.26 in, and a length of 11.5 hydraulic diameters. It was mounted in the pipe such that the flow develops ten pipe diameters before entering the honeycomb, and then has ten more pipe diameters to develop before entering the experimental test section. Unfortunately, these profiles strongly show the presence of the honeycomb within the pipe. In order to try and reduce the presence of the honeycomb on outlet flow profiles, a refined honeycomb with a hydraulic diameter of 0.15 in and a length of 20.2 hydraulic diameters, was fabricated as shown in Figure 21(b), with the resultant flow profiles being shown in Figure 20(c). The refined honeycomb shows a much more symmetric profile, and is discussed further in Appendix A. Additionally, the velocity contours (and subsequent downstream contours) do not exhibit any strong asymmetries or hexagonal pattern as observed before, suggesting a lack of asymmetric swirl, and as seen later creating symmetric turbulent fluctuations. In order to accommodate the high temperatures capable of being achieved in the experimental facility, a high temperature ceramic, Samos®

Nano Tool™, printed by FineLine Prototyping, was used to make six honeycombs for use in the unit cell and triple-jet experiments. These ceramic honeycombs are shown in Figure 21 (c).

3.1.2 In-Situ Single Wire Calibration

One method of experimental velocity measurement is constant temperature anemometry (CTA). The heat transfer from a long wire exposed to Joule heating is shown in Equation (9), where Q is the power required to heat the wire, E is the wire voltage, R_w is the wire resistance, A is the surface area of the wire, T_w is the wire temperature, and T_∞ is the fluid temperature. From this expression, it can be seen that the wire voltage is dependent on the heat transfer coefficient, h . According to King's Law the heat transfer coefficient for flow across a cylinder is proportional to the Reynolds number raised to an exponent. If the electrical circuitry utilized to heat the wire can adaptively maintain the wire temperature the voltage is a function of only the Reynolds number, or more specifically the velocity of the flow across the wire as shown in Equation (10) where a , b , and c are curve fit coefficients. In Equation (10) U_{ref} is 1 m/s. If the ambient temperature is not expected to vary the term $T_w - T_\infty$ can be included in the curve fit coefficients a and c . For a detailed description of both the theoretical heat transfer and the signal conditioning electronics involved, see [57] and [61]. For the current work the hot wire probe is a 5 μm gold plated wire manufactured by Dantec Dynamics, model 55P16. The signal conditioning box is a Dantec Dynamics 54T30 miniCTA.

$$Q = \frac{E^2}{R_w} = hA(T_w - T_\infty) \quad (9)$$

$$E^2 \propto (\text{Re}^b + c)(T_w - T_\infty) \cong \left(a \left[\frac{|\mathbf{U}|}{U_{ref}} \right]^b + c \right) (T_w - T_\infty) \quad (10)$$

In order to express the output voltage of the CTA in terms of a velocity, the probe is first calibrated using the Dantec 54H10 Hot-wire Calibrator. This is capable of creating flows ranging from 0.5 m/s to 60 m/s. The CTA is placed in the center calibrator nozzle and approximately 10 velocities are considered ranging from 1.5 to 30 m/s. For the calibration standard velocity is calculated relative to the pressure drop across a known geometry orifice plate. The fluid density is corrected for both the atmospheric pressure, measured using a Conex Electro-Systems JDB-1 barometer (± 170 Pascal), and temperature, using a thermistor (± 0.2 K) internal to the calibrator. The pressure drop across the orifice plate is measured with a high accuracy pressure transducer (Omega MMDWU10WV5P2D0T2A2) with an accuracy of 0.05% of the full scale (10 inch water column, or 2.5 kPa). Five independent tests were ran to account for repeatability error. Shown in Figure 22 is a plot of the calibrator velocity versus the CTA voltage corrected for using an average ambient temperature of 18.6°C, gathered using a Constant Current Anemometer (discussed later). Note that T_w is the wire temperature, maintained at a constant 242°C. The CTA curve fit is also shown.

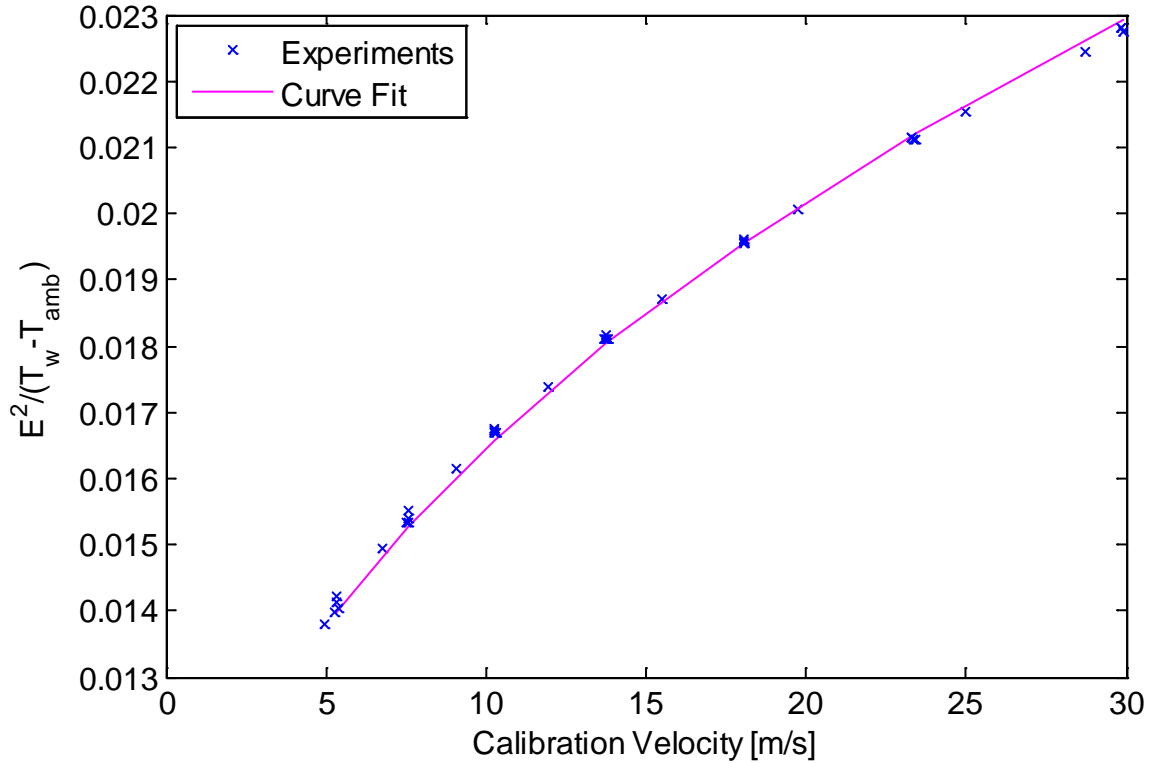


Figure 22- Calibration velocity versus CTA voltage corrected for temperature

For the CTA calibration, five separate voltage versus velocity curves were gathered in order to quantify the repeatability error. The average of each velocity is utilized in the calibration curve fit, the form of which is provided in Equation (11), where V is the magnitude of the velocity, E is the voltage output from the CTA which is captured via a data acquisition unit (National Instruments NI-9215A), and a , b , and c are the curve fit parameters found to be $0.003633 \frac{V^2}{^\circ C}$, 0.448 , and $0.00627 \frac{V^2}{^\circ C}$. The experimental data and the corresponding curve fit are shown in Figure 22. The maximum error for the curve fit is 22.1%, while the mean error for the curve fit is 2.42%. Note that if velocities less than 6 m/s are discarded due to the high uncertainty in pressure drop measurements, the mean error for the curve fit is 2.14% while the maximum

error is 7.4%. Figure 23 shows the calibration velocity versus that recovered via the curve fit. As seen the data largely falls within 5% of the calibration velocity.

$$|\mathbf{U}| = \left(\frac{\frac{E^2}{T_w - T_\infty} - c}{a} \right)^{1/b} \quad (11)$$

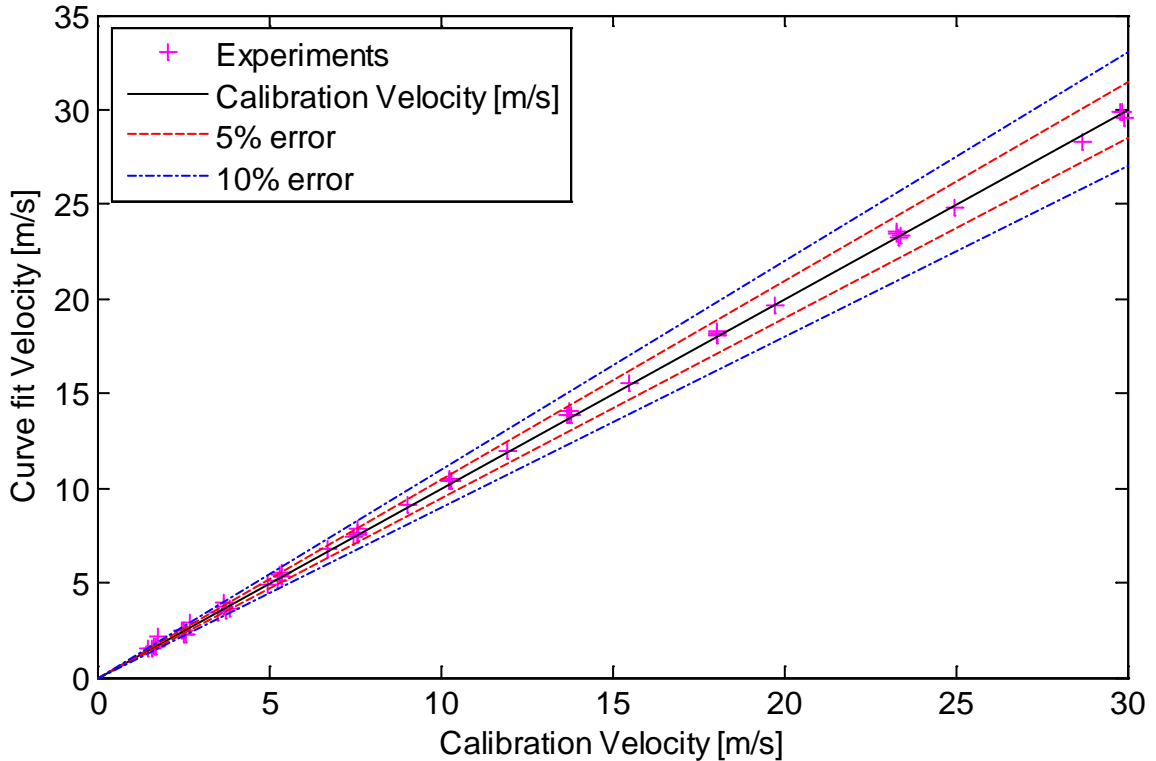


Figure 23 – Comparison of calibration and predicted velocities

Numerous previous hot-wire studies [21, 22, 38, 57, 58, 59, 60, 61] have utilized this calibration approach for investigating isothermal flows. While his calibration approach would be acceptable if the ambient temperature is held constant between the calibration and data acquisition steps for the present work the temperature difference in the triple-jet was as large as 50°C. The temperature differences in the domain drastically reduce the applicability of conventional hot-wire techniques creating a need for new calibration procedures. Some previous

work has looked at increasing the applicability of CTA in non-isothermal flows, often by incorporating real time control of the wire temperature in order to fix the temperature difference in Equation (10). However, such solutions often require hardware specifically designed for the flow being studied [57]. In order to study the effect of temperature on curve fit parameters a and c , multiple calibrations similar to that shown in Figure 22 were gathered for flows at various temperatures. The range of temperatures were created using a 3 kW Wattco. Inc. submersion heater placed inline with the Dantec Calibrator. For these flows the fluid temperature was measured utilizing a higher accuracy ($\pm 0.015^\circ\text{C}$) Omega RTD model HH42. Results from this study are shown in Figure 24 (a) where the temperature corrected squared voltage is compared to the calibrator velocity. Not surprisingly, each unique temperature generates a different voltage and velocity relationship. A curve fit with constant coefficients would obviously introduce a large amount of error (see for example Figure 24 (b)), and therefore the functional dependence of a and c with respect to temperature must be adequately captured.

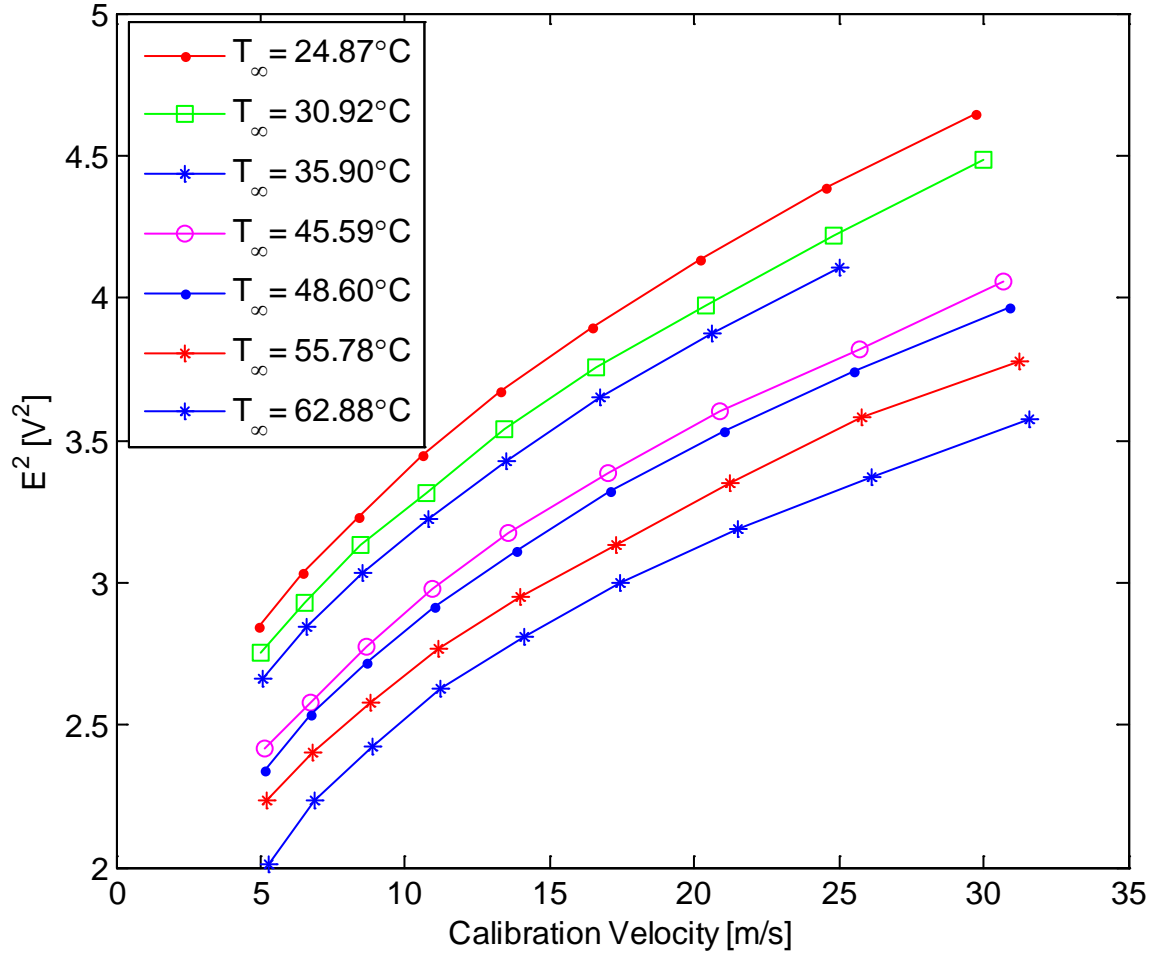


Figure 24 – (a) CTA calibration curves for heated flows

To address the errors when utilizing a constant curve fit a temperature dependent curve fit was developed as shown in Equation (12) where the temperature difference ($T_w - T_{\infty}$) is now grouped in the coefficients $a(T)$ and $c(T)$, similar to the work in [57]. As suggested in that study, b is approximately 0.5 and independent of temperature. Moreover, a and c are expected to be linear functions of temperature. In order to check the functional dependence of a and c on temperature, each curve of data shown in Figure 24 (a) were fit using a least squares regression. From the unique curve fit coefficients for each temperature curve the average coefficient b was 0.3819. Then, fixing the exponential value b , the coefficients a and c are reevaluated. The new

coefficients $a(T)$ and $c(T)$ are then fit linearly as a function of temperature. For the temperature dependent calibration, experimental data for 9 unique velocities and 7 unique temperatures was used as training data for the curve fits of a , b , and c . From the training data, the curve fits for $a(T)$ and $c(T)$, shown in Figure 25, are listed in Equations (13) and (14).

$$E^2 = a(T) \left(\frac{|U|}{U_{ref}} \right)^b + c(T) \quad (12)$$

$$a(T) = -0.0050 \left[\frac{E^2}{^\circ\text{C}} \right] T + 1.1140 [E^2] \quad (13)$$

$$c(T) = -0.0117 \left[\frac{E^2}{^\circ\text{C}} \right] T + 1.3127 [E^2] \quad (14)$$

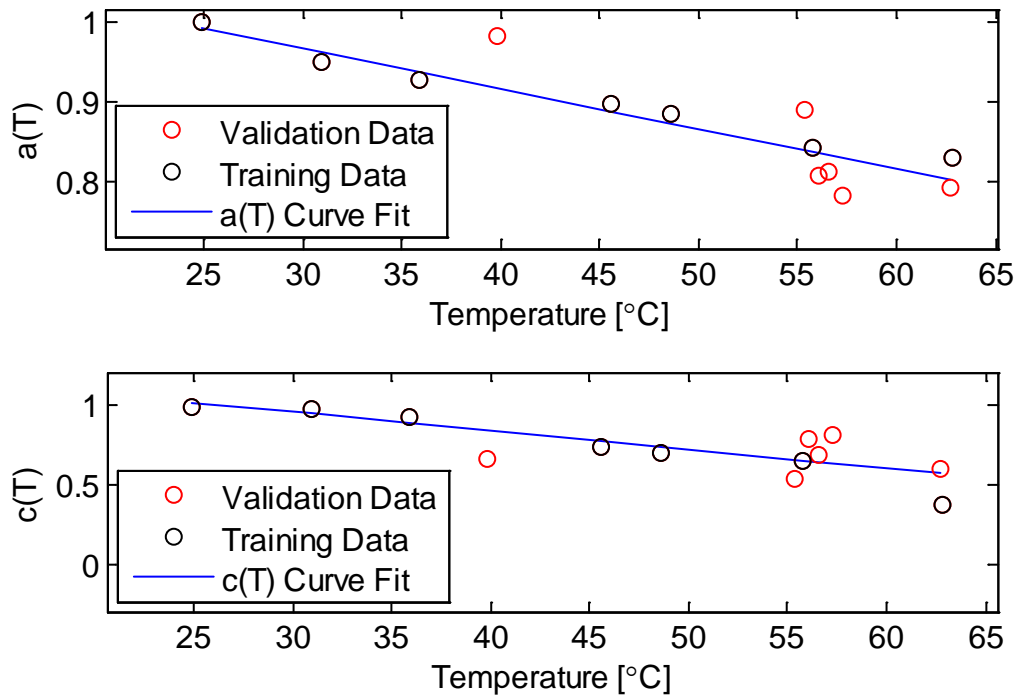


Figure 25 – Temperature dependency of a and c with curve fits shown

In addition to the training data, it was necessary to ensure the curves generated could adequately be used for all gathered data points, thus the 6 unique temperatures, each with 9

velocities, not used in the training data set are used as validation data. Additionally, to check for hysteresis and systemic errors, four different temperatures and four velocities were also gathered to be used as random data. Shown in Figure 26 is the curve fit velocity for the training data set, the data omitted from the training cases which was then used as validation data, and the random validation data set versus the calibration velocity. For the training data the mean error was 3.68% while for all data sets the mean error was 3.06%. Similarly, the maximum error for the training data and entire set of data is 15.65% and 17.65%, respectively, with both maximums occurring for the lowest velocity tested.

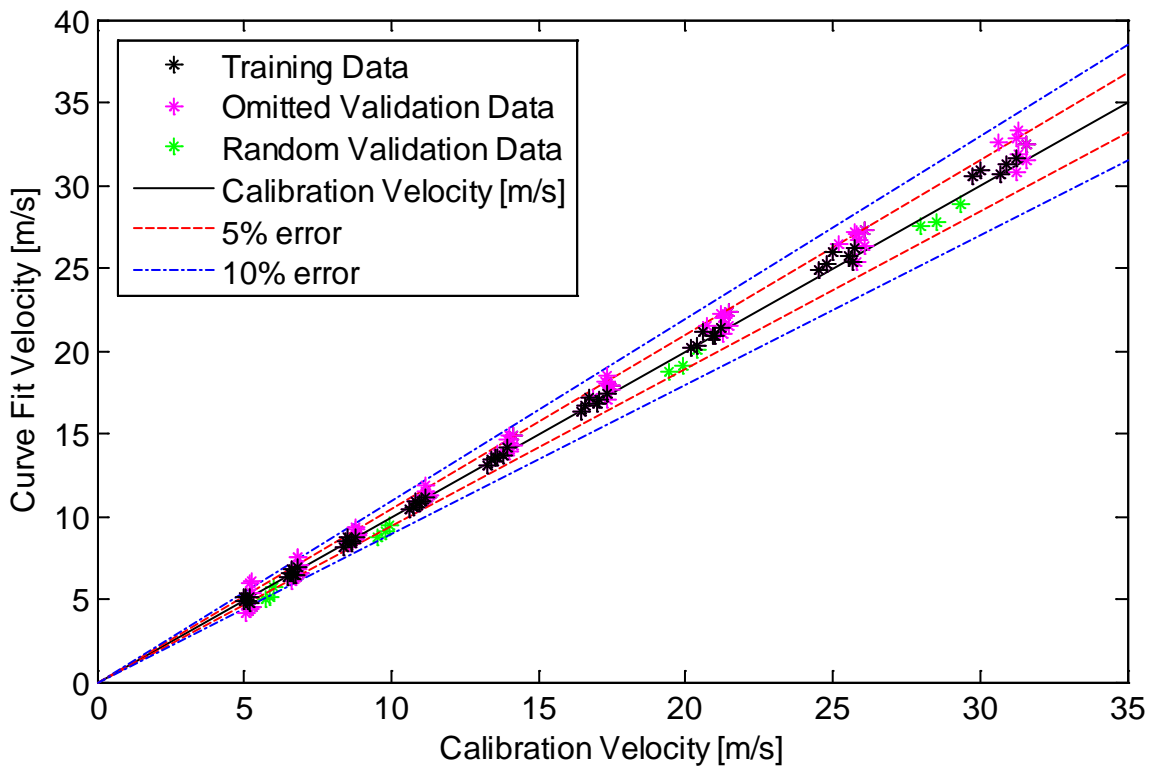


Figure 26 – Curve fit velocity versus calibration velocity for all tested data

To correct for variation in ambient temperature from the calibration, the CTA was mounted in parallel with a constant current anemometer, referred to as the cold wire, as shown in Figure 27. Note that the CTA and CCA are located in parallel 4.76 mm apart. It should be noted

that since the temperature and velocity measurement points are not co-located, errors exist by making that assumption. These errors in velocity and temperature correction are discussed in Section 3.1.3. Cold wire signal conditioning was done utilizing an AA Lab Systems Inc. AN-1002 with Option 11, constant current anemometer mode. A second Dantec 55P16 5 μm gold plated wire was used for the cold wire. Calibration of the cold wire was achieved through separate experiments conducted in the actual facility. The temperature standards were taken from tightly calibrated thermocouples placed at the direct center of the outlet of the jets. These temperatures were then used in conjunction with the CCA voltage gathered at each location to determine coefficients for a linear calibration curve for the cold-wire. For the remaining work in this thesis, the CCA curve fit was applied as shown in Equation (15). The mean error from the CCA curve fit was 1.9%

$$T [^{\circ}\text{C}] = 8.51 \left[\frac{^{\circ}\text{C}}{\text{V}} \right] E + 34.1 [^{\circ}\text{C}] \quad (15)$$



Figure 27 - CTA and CCA two-wire probe

3.1.3 Temperature Correction Error Quantification

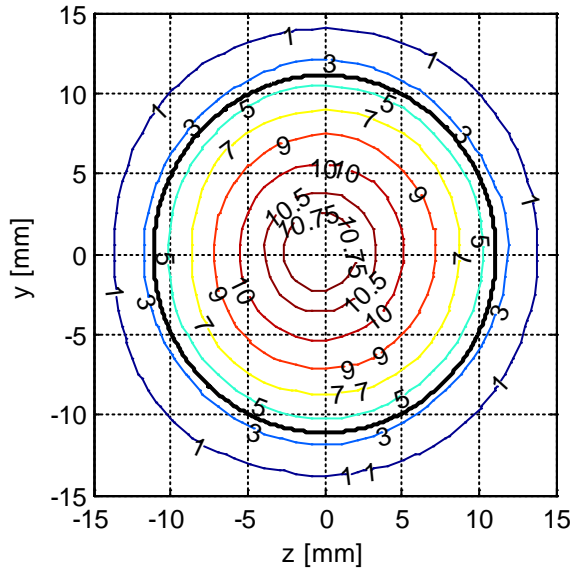
As shown previously in Figure 27, temperature correction was done using a single wire CCA mounted in parallel with a single wire CTA. For the current work, both the CTA and CCA voltage were sampled at 2 kHz utilizing a NI-9215 BNC DAQ card. Since it is not possible to locate both wires in the same physical space, there is some offset that exists between the wires.

For the probe mount designed, the CTA and CCA are located 4.76 mm apart. Multiple wire probes are available, but suffer from the same issue, namely collocated measurements are not possible. For reference, a specialty four-probe sensor (three for velocity and one for temperature) from Dantec Dynamics has an offset of 1.3 mm between the CCA and the center of the three CTA wires. Although this smaller offset could potentially be justified as zero under certain conditions, this must be carefully done. For the two sensor assembly used in the current study, two approaches for CTA temperature correction were considered. For the first method, it was assumed that the CCA and CTA experienced the same temperature and that all corrections to velocity can be applied in real time with the simultaneously sampled temperature field. This method is shown in Equation (16) where the subscript i denotes simultaneously sampled data points while $\langle \rangle$ denotes the arithmetic mean. This will be referred to as the temporally congruent method. In regions where there exists a large temperature gradient this correction method is expected to produce significant errors. The second methodology uses collocated data points, with the assumption that temporal variation is not significant. Since the samples are no longer simultaneous only mean values for the CTA probe voltage and the CCA temperature are used, as illustrated in Equation (17). This method is referred to as being spatially congruent. Note that when using mean data, any temporally dependent flow quantities, such as velocity fluctuation, cannot be calculated.

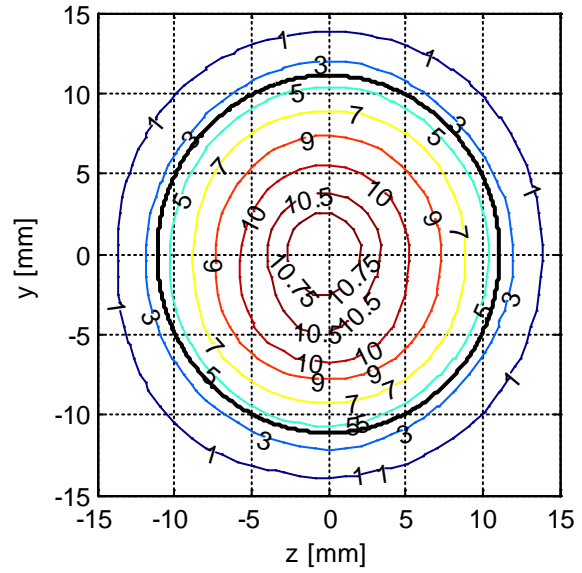
$$|\mathbf{U}_{\text{simultaneous}}| = \left\langle \left[\frac{E_i^2 - (c_1 T_i + c_2)}{a_1 T_i + a_2} \right]^{1/b} \right\rangle \quad (16)$$

$$|\mathbf{U}_{\text{collocated}}| = \left[\frac{\langle E \rangle^2 - (c_1 \langle T \rangle + c_2)}{a_1 \langle T \rangle + a_2} \right]^{1/b} \quad (17)$$

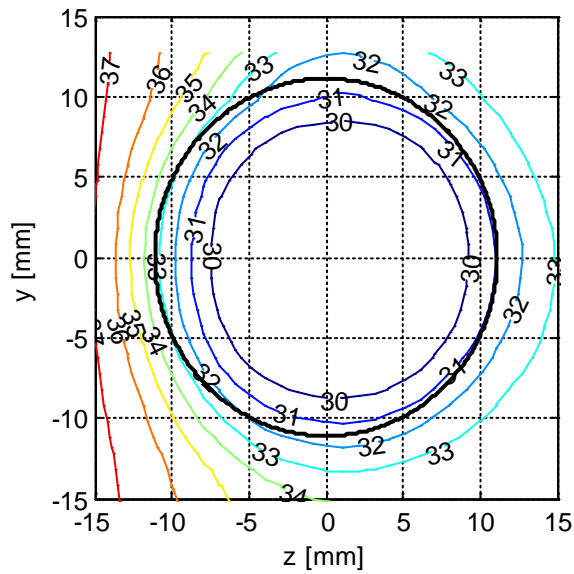
In order to quantify the error due to the limited spatial resolution of the probe, profiles for the mean velocity, calculated utilizing simultaneous but displaced data and using collocated but at separate times, were compared as shown in Figure 28 (a) and (b), respectively, with contours of jet temperature shown in (c). For this data, the CTA and CCA wires were aligned with the z-axis with the CCA being displaced -4.76 mm from the CTA wire. For the quantification of jet profiles, only the line cooled by the heat exchanger was used, creating a single jet. Since these temperatures were relatively low ($\sim 30^{\circ}\text{C}$) the presence of an ambient temperature gradient, most likely from the linear stage stepper motors, is observed in the $-z$ direction in Figure 28 (c). When comparing the velocity profiles in (a) and (b) the most obvious difference is the oblong deformation in the $-y$ -direction near the center of the jet when utilizing temporally congruent data. This error is expected due to the spatial resolution. To quantify this resolution the profiles and their errors are compared and shown in Figure 29 where a positive error suggests that simultaneous temporal correction under predicts the velocity found using a collocated temperature correction, while oppositely a negative error suggests that the simultaneous correction method predicts a larger velocity than the mean correction method. As expected when considering the data presented in Figure 24 (a), when the CCA is in the warmer ambient fluid (near the $-z$ periphery of the jet) the simultaneous correction method under predicts the jet velocity. Conversely when the CCA wire “lags” behind the CTA and is still in the cold jet, the velocity is over predicted utilizing the simultaneous correction method.



(a)



(b)



(c)

Figure 28 - (a) Velocity magnitude with simultaneous temperature correction [m/s] (b) Velocity magnitude with collocated temperature correction [m/s] (c) Temperature [°C]. For each contour, the circular jet geometry is included for reference (solid black line, $D_{jet} = 0.875$ in (22.23 mm)). $Re_{jet} = 1.06 \times 10^4$

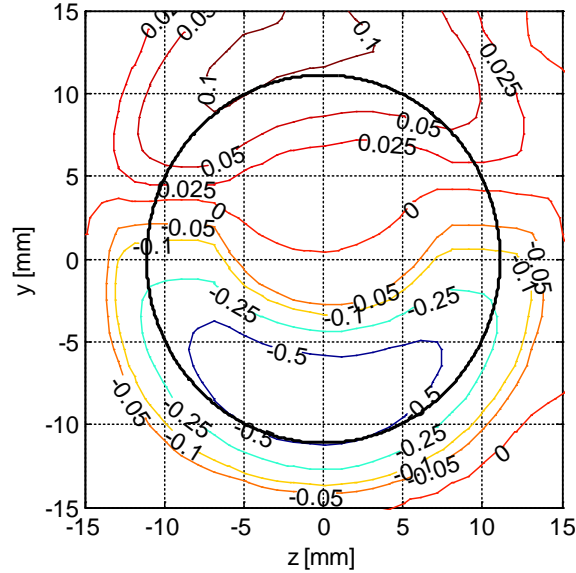
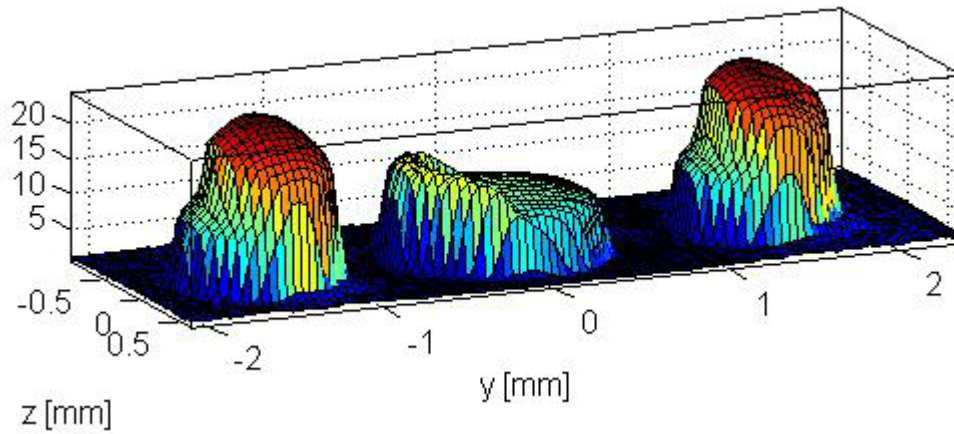
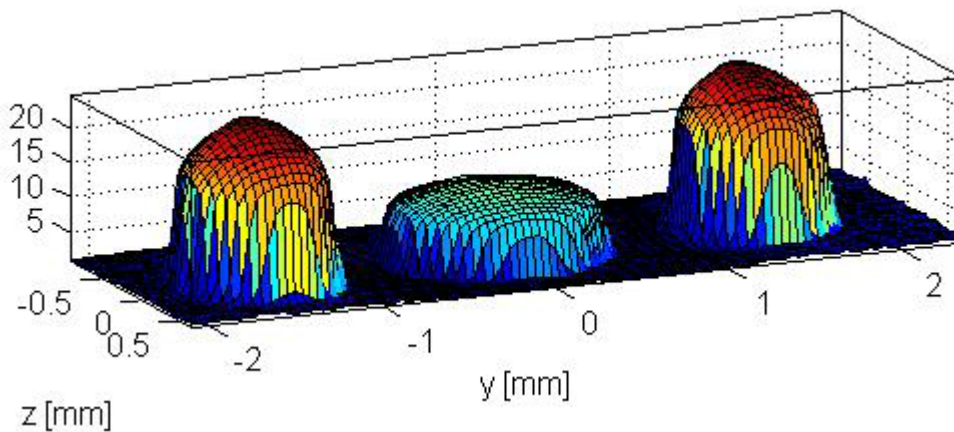


Figure 29 – Error [m/s] between different velocity correction methods. The circular jet geometry is included for reference (solid black line, $D_{jet} = 0.875$ in (22.23 mm)). $Re_{jet} = 1.06 \times 10^4$

For the work in this thesis, it is generally preferred to measure velocity magnitude profiles using the collocated, spatially congruent temperature correction method introduced in Equation (17). For the majority of conditions studied, there exists large temperature difference between the jets in the domain ($\sim 45^\circ\text{C}$). In the presence of these large differences, and subsequently large temperature gradients, the simultaneous correction method creates unexpected artifacts in the jet profiles. This is easily seen for a typical triple jet experiment, results of which are shown in Figure 30 (a). The most drastic errors are seen on the $-y$ direction of all three jets. For comparison the mean corrected velocity profiles for the same case are shown in Figure 30 (b). Note that for quantification of temporally dependent quantities, namely the fluctuating velocity magnitude and following the turbulent kinetic energy and turbulent intensity (Equations (18) and (19) defined following) it is necessary to use simultaneously corrected velocity magnitudes. More detailed analysis of the data in Figure 30 will be conducted in Section 4.2.



(a)



(b)

Figure 30 – triple-jet velocity magnitude for $R=1/2$ $\Delta T=60^\circ\text{C}$ (a) Velocity Magnitude using simultaneous temperature correction (b) - Velocity Magnitude using collocated temperature correction.

3.2 VELOCITY CONTOURS AND TURBULENCE QUANTIFICATION

Before studying the behavior of a parallel triple-jet, attributes of the single jet scenario are of interest. Extreme care is taken to ensure the jet enters completely normal to the test section, but in reality there could potentially be some misalignment between the jet and the linear

stages upon which the CTA is mounted. A detailed examination of this misalignment, studied for an earlier iteration of the experimental design is given in Appendix B. Presently a detailed examination of the inlet profiles for a single jet is conducted. Velocity data in the y - z plane are captured utilizing the temperature corrected single wire anemometer (Figure 27) at $x/D_{jet} = 0.09$ (slightly downstream of the jet nozzle). For a description of the two-wire probe and a description of the calibration procedures please see Section 3.1.1. For these tests the jet Reynolds number was $Re_{jet} = 10.6 \times 10^3$ at 27°C . Contours for the velocity, turbulent kinetic energy, and percent turbulent intensity are shown in Figure 31(a), (b), and (c), respectively. The black circle represents the outline of the jet nozzle. The jet is approximately a power law velocity profile, with the majority of the velocity decay occurring near the nozzle walls. For the turbulent kinetic energy (Figure 31 (b)) and percent turbulence intensity (Figure 31 (c)), the respective quantities are computed from the velocity data according to Equation (18) and (19). Similarly, surface plots for turbulent kinetic energy and percent turbulent intensity are shown in Figure 32 (a) and (b) respectively. As shown in Figure 31 (a) and Figure 32 (a) the kinetic energy is approximately $0.1 \text{ m}^2/\text{s}^2$ near the center of the jet, increases to a peak value of approximately $0.2 \text{ m}^2/\text{s}^2$ just inside of the diameter of the jet, then decreases to a very small value outside the jet where the mean velocity is close to zero. Very similar trends are seen for percent turbulent intensity in Figure 31 (b) and Figure 32 (b). Note that the average turbulent intensity over the diameter of the jet is 8.55%. For future studies where the experimental data will be used to validate numerical modeling efforts, it is ideal to have a symmetric, easy to quantify profile. The setup, in its current configuration, meets these requirements as described later.

$$k = \frac{1}{2} \langle |\mathbf{U}| - \langle |\mathbf{U}| \rangle \rangle^2 \quad (18)$$

$$I\% = \frac{\langle |U| - \langle |U| \rangle \rangle}{\langle |U| \rangle} \cdot 100 \quad (19)$$

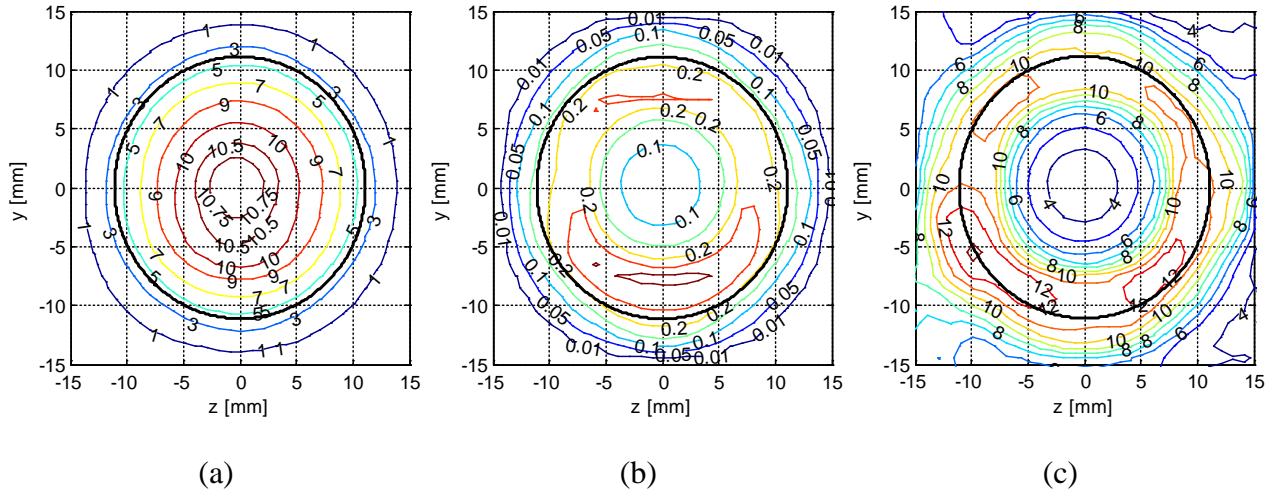


Figure 31 - Contours at $x/D_{jet} = 0.09$: (a) Simultaneously corrected velocity magnitude (m/s), (b) turbulent kinetic energy (m^2/s^2), and (c) percent turbulence intensity. For each contour, the circular jet geometry is included for reference (solid black line, $D_{jet} = 22.23$ mm). $Re_{jet} = 1.06 \times 10^4$

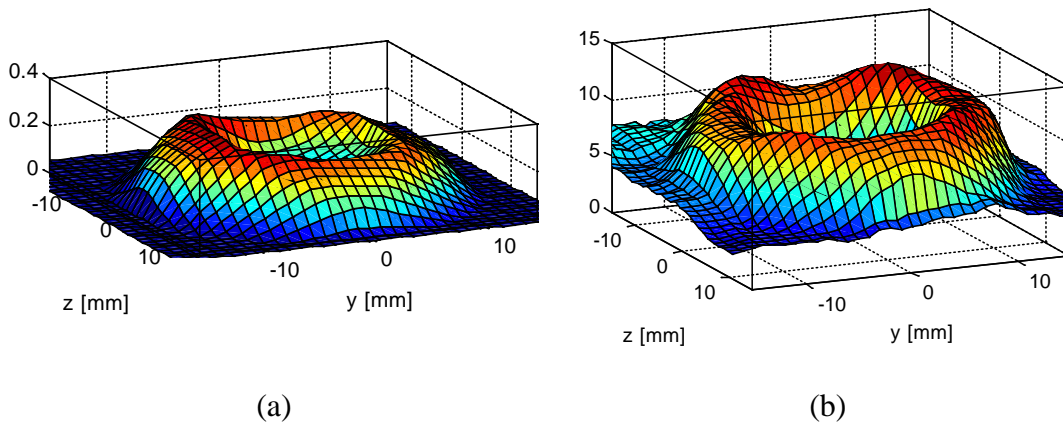


Figure 32 - Surface plots of single jet contours. (a) Turbulent kinetic energy [m^2/s^2] (b) Percent turbulent intensity

3.3 QUANTIFICATION OF JET PROFILE

It is important to be able to gauge and quantify the asymmetries in a manner other than a visual estimate, as well as to find an appropriate, axisymmetric curve fit. Here, we choose to analyze velocity data traces from six distinct lines in the contours: negative y -axis, positive y -axis, negative z -axis, positive z -axis, quadrant one (positive z , positive y) diagonal cut, and quadrant 3 (negative z , negative y) diagonal cut, as shown in Figure 33. This creates eight unique lines, representative of four lines “folded” onto themselves. If the jet were perfectly symmetric, these eight lines would lie exactly on top on each other. This data is shown for $x/D_{jet} = 0.09$ plane in Figure 34 where the velocities have been normalized by the centerline value (U_0). Investigating the data near the periphery of the jet, by $r/D_{jet} = 0.5$ the velocity has dropped to 20% of the centerline velocity. In order to fit the data, a power law relationship was chosen as suggest by Schlichting [37]. It is shown that the coefficient of the power law, b in Equation (20), varies as a function of the Reynolds number, for example Mi [38] found $n = 6.5$ in experiments. Pope [47] suggests the dependency of n on Reynolds number can be given by Equation (21), which for our given flow of $Re_{jet} = 10.6 \times 10^3$ yields $n = 5.178$. In order to account for variability in the power law coefficient a least squares regression method was utilized. Fitting the data for $0 < |r/D_{jet}| < 0.45$ (90% of the diameter of the jet), it was found that $m = 1.139$ with $n = 6.12$ with $R^2 = 0.9889$. As reported the calculated power law does not agree with that suggested by Pope. This is likely do to variations in the flow conditions upstream of the jet. Moreover this could possibly suggest our curves are not fully developed. Investigating our curve fit, over 90% of the domain the mean error was 0.78% with a maximum curve fit error of 3.87%, occurring at the outer most points. For comparison, several different curve fits and data ranges were tested. The

results, in conjunction with those in Figure 31, show that the facility produces a jet with a predictable and acceptable mean velocity profile.

$$\frac{|\mathbf{U}|}{U_0} = m \left| \frac{r}{D_{jet}} - \frac{1}{2} \right|^{1/n} \quad (20)$$

$$\frac{1}{n} = \frac{1.085}{\ln Re} + \frac{6.535}{(\ln Re)^2} \quad (21)$$

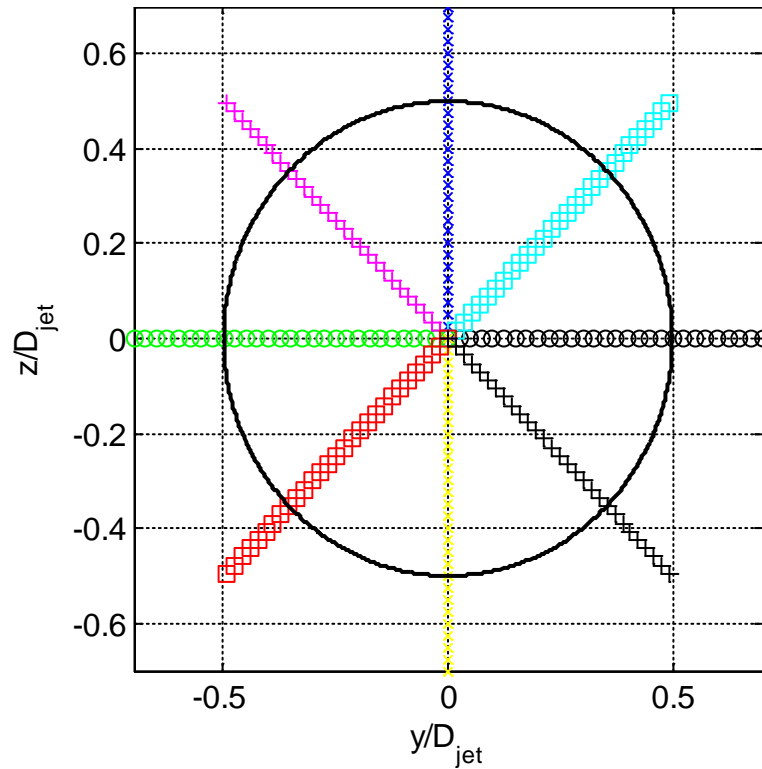


Figure 33 - Schematic of line traces used to analyze single jet

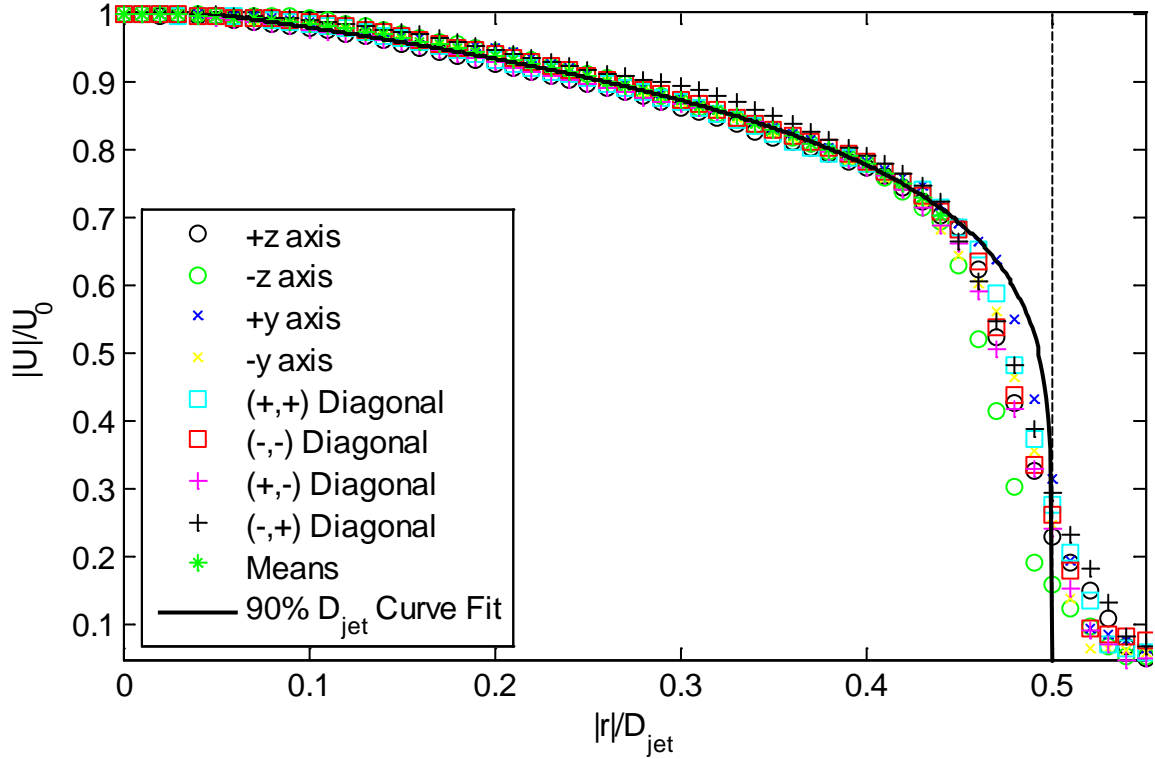


Figure 34 – Normalized velocity contours “folded” on each other with curve over 90% D_{jet} for $x/D_{jet} = 0.09$ for $Re_{jet} = 10.6 \times 10^3$, $U_0 = 13.78$ m/s

To further validate the curve fit present the mass flow rate of the jet was considered. The equation for the mass flow rate is given in Equation (22) where m and n are the same as in Equation (20), 1.139 and 6.12 for our given case, and U_0 is the centerline velocity, equal to 13.78 m/s for single jet study. For the given test case, the theoretical volumetric flow calculated from Equation (22) is 0.00432 m³/s. Using Sampson’s rule to integrate the numerical results shown in Figure 28 (b) as an approximation to the volumetric flow rate present in the experiment. Considering only those points within the diameter of the jet, the experimentally measured volumetric flow rate is 0.004249 m³/s. For the given study the flow rate was set in the PLC controller (See Section 2.1.4) to 6.37 cfm (0.003006 m³/s). This suggests the error between the measured volumetric flow rate and the programmed/expected mass flow rate is 43.7%. Additionally, using the programmed volumetric flow rate the peak velocity estimated via the

curve fit shown in Equation was 9.58 m/s, suggesting the peak velocity was over estimated by 43.8%.

$$\dot{V} = 2\pi \int_0^{\frac{D_{jet}}{2}} U_o m r \left| \frac{r}{D_{jet}} - \frac{1}{2} \right|^{1/n} \partial r \quad (22)$$

This seemingly large error can be attributed to a shift in the AN-1002 CCA signal conditioning box, which is a highly sensitive electronic device. Out of necessity unrelated to the current work, the laboratory was relocated, and the original calibration curve was no longer valid. As previously noted, a small error in temperature compensation can yield large difference in predicted velocities from the CTA. In order to address this calibration shift, a set of triple jet experiments were performed and the calibration adjustments were made in response to the known temperatures (measured with tightly calibrated thermocouples) and known flow rates (quantified by the PLC controller, whose error is negligible compared to that of the temperature compensated velocity calibration approach). The triple jet experiments used for this calibration shift are listed in Table 4. Note that the distance between the jets was large so that the velocity and temperature just downstream of the nozzle are assumed to be isolated from the neighboring jets.

Table 4 - Velocity and temperature calibration experiments

R	x/D_{jet}	S/D_{jet}	\dot{V}_{cold} [m³/s]	U_{cold} [m/s]	\dot{V}_{hot} [m³/s]	U_{hot} [m/s]	ΔT [°C]
½	0.09	3.00	1.06 x10 ⁴	9.59	6.07 x10 ⁻³	19.18	22.2
½	0.09	3.00	1.06 x10 ⁴	9.59	6.07 x10 ⁻³	19.18	44.4
½	N/A	3.00	3.06x10 ⁻³	9.59	6.07 x10 ⁻³	19.18	44.4
½	N/A	3.00	3.06x10 ⁻³	9.59	6.07 x10 ⁻³	19.18	11.1

In order to account for the shift in temperature a correction to the original equation was investigated according to Equation (23) where α represents a proportional correction to the measured temperature and β represents a bias error. In order to quantify these error correction

factors it is necessary to trust velocity expected in the jets. As such, only cases where the jets are spaced sufficiently far apart enough that effects are not expected near the inlet are utilized. This is then done utilizing the experiments in Table 4, all of which are discussed in more detail in Section 4.0 . First, utilizing the curve fit equations m and n from the non-corrected Equation (17), the peak expected velocity, based on the flowrate programmed into the PLC was found. Then utilizing these peak velocities α and β were found utilizing a least squares regression method. Next an iterative procedure was utilized where the peak expected velocities were updated using Equation (23), then the coefficients were solved for again. This procedure was repeated multiple times until the coefficients no longer changed with subsequent iterations. The final coefficients were found to be $\alpha = 1.0498$ and $\beta = -9.7035^\circ\text{C}$. Before applying the temperature correction factors the maximum and mean error between the measured velocity and expected velocity was 28.1% and 21.3% respectively. After applying the correction factors to the calibrated data set the max and mean absolute errors were 3.8% and 1.0%.

$$U = \left[\frac{\langle E \rangle^2 - a(\langle \alpha T + \beta \rangle)}{c(\langle \alpha T + \beta \rangle)} \right]^{\frac{1}{b}} \quad (23)$$

Reinvestigating the velocity profiles, given the new correction technique a power law fit of the same from originally used was applied with the constants $m = 1.141$ and $n = 5.874$. Utilizing the new curve fit coefficients the expected peak velocity, based on the skid flow rate, is 9.65 m/s. The peak measured velocity is 11.22 m/s for a 16.3%. Calculated as done before the measured volumetric flow rate was 0.0034 m³/s, which compared to the flow rate programmed into the skid of 0.0031 m³/s yields an error 11.1%. Note that the temperature correction factors α and β were used when creating all of the previous velocity plots and contours.

Additionally, after quantifying the velocity profile attention was given to quantifying the temperature profiles in the jets. As shown in Figure 35 the same eight unique traces of the jet temperature were “folded” on top of each other and compared. Since the jet temperature deviates only slightly from the ambient there is a steady heat up of the jet in the $-z$ direction as observed for all traces originating in the $-z$ -hemisphere of the jet. Note that across 90% of the jet diameter the mean temperature of the slices varies by 2.6% of the centreline temperature. For this reason the jet was qualitatively considered to have a tophat temperature profile. Rigorous efforts are not spent to quantify the jet temperature profile for this case, but is given additional attention in all triple-jet experiments where the ambient temperature in the test section differs more subsequently from the jet temperatures. Moreover, it will be convenient to non-dimensionalize the temperature profile, which is more straight forward when there are two constrained jet temperatures in the domain.

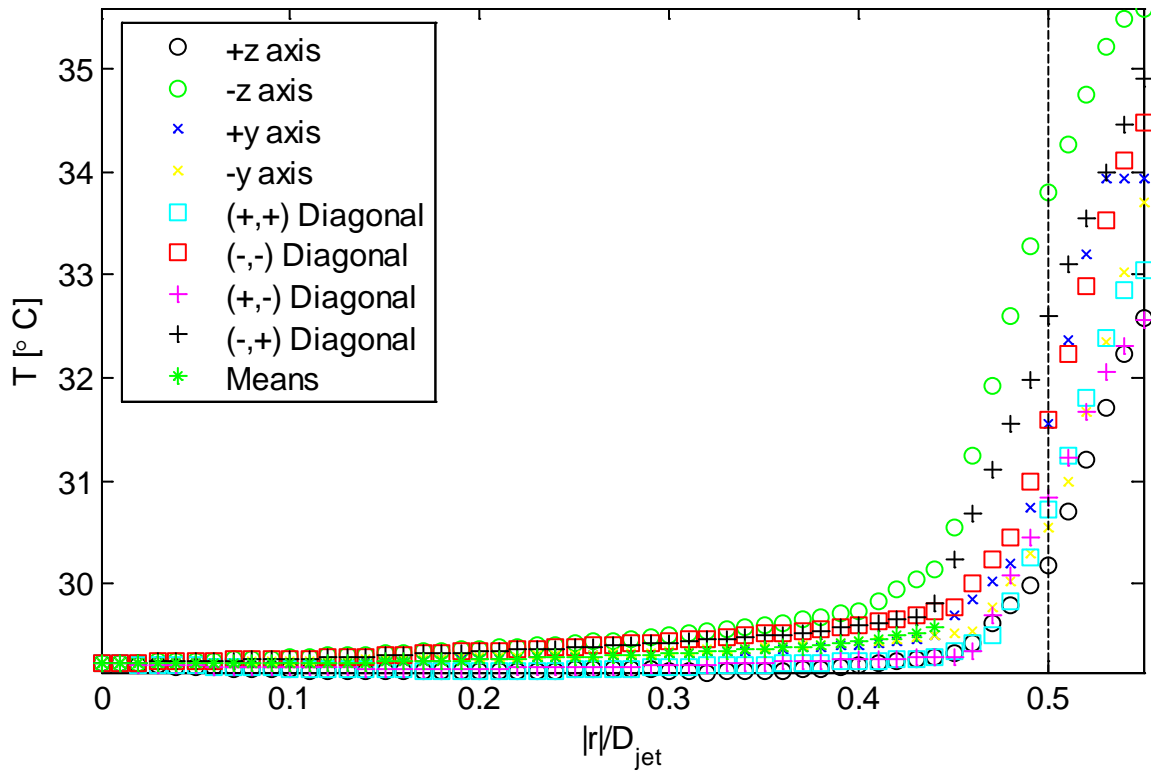


Figure 35 - Temperature contours “folded” on each other with curve over 90% D_{jet} for $x/D_{jet}=0.09$ for $Re_{jet} = 10.6 \times 10^3$

4.0 MEASUREMENTS IN A PARALLEL-TRIPLE-JET

Of primary interest in parallel triple-jets is turbulent mixing between the jets. This phenomenon in non-isothermal flows is thought to influence thermal striping in support components in the VHTR, as well as serve to prevent thermal stratification in piping connections. However, properly studying turbulent mixing can be difficult in experimental studies utilizing constant temperature anemometry. When considering a single-wire anemometer, only the magnitude of velocity, and its fluctuation, can be gathered, opposed to individual components of the velocity and the respective fluctuations. One improvement to single-wire anemometry is three-wire anemometry, where three orthogonal, simultaneous velocity measurements are captured corresponding to the entire velocity vector at a point. Considered for future work, an overview of three wire anemometry for both isothermal and non-isothermal flows is considered in Appendix C. For the present work, the custom built two-wire CTA and CCA probe was utilized with temperature dependent curve fits as detailed in Section 3.1.1. In order to study the flow in a round parallel triple-jet, a matrix of experiments was gathered in separate horizontal and vertical measurement planes. Multiple horizontal planes of data were acquired at different downstream distances. For the vertical plane data sets, each was gathered on the $y = 0$ plane. A list of the cases studied is shown in Table 5 and Table 6. In Table 5 the case $R = \infty$ is the case of a single free jet analyzed in Section 3.0 while in Table 6 the case $R = 0$ is the

case of a round twin-jet. It should be noted that case H4 and case H5 were used as the calibration set discussed in Section 3.3.

Table 5 – Matrix of cases mapped in horizontal plane

Y-Z Plane Experiments								
#	R	x/D_{jet}	S/D_{jet}	\dot{V}_{cold} [m ³ /s]	Re_{Cold}	\dot{V}_{hot} [m ³ /s]	Re_{Hot}	ΔT [°C]
H1	1/2	0.09	1.41	3.08×10^{-3}	1.05×10^4	6.07×10^{-3}	1.93×10^4	44.4
H2	1/2	5.09	1.41	3.08×10^{-3}	1.05×10^4	6.07×10^{-3}	1.93×10^4	44.4
H3	1/2	10.09	1.41	3.08×10^{-3}	1.05×10^4	6.07×10^{-3}	1.93×10^4	44.4
H4	1/2	0.09	3.00	3.08×10^{-3}	1.05×10^4	6.07×10^{-3}	1.93×10^4	44.4
H5	1/2	0.09	3.00	3.08×10^{-3}	1.05×10^4	6.07×10^{-3}	1.93×10^4	22.2
H6	∞	0.09	N/A	3.08×10^{-3}	1.05×10^4	N/A	N/A	N/A

Table 6 - Matrix of cases mapped in vertical plane through jet centerline

X-Z Plane Experiments							
#	R	S/D_{jet}	\dot{V}_{cold} [m ³ /s]	Re_{Cold}	\dot{V}_{hot} [m ³ /s]	Re_{Hot}	ΔT [°C]
V1	0	2.81	N/A	N/A	6.07×10^{-3}	1.93×10^4	N/A
V2	1/2	1.41	3.06×10^{-3}	1.05×10^4	6.07×10^{-3}	1.93×10^4	44.4
V3	1/2	1.41	3.06×10^{-3}	1.07×10^4	6.07×10^{-3}	2.05×10^4	22.2
V4	1/2	3.00	3.06×10^{-3}	1.05×10^4	6.07×10^{-3}	1.93×10^4	44.4
V5	1/2	3.00	3.06×10^{-3}	1.07×10^4	6.07×10^{-3}	2.11×10^4	11.1
V6	1	1.41	6.07×10^{-3}	2.15×10^4	6.07×10^{-3}	1.96×10^4	44.4
V7	1	1.41	3.06×10^{-3}	1.06×10^4	3.06×10^{-3}	9.66×10^3	44.4
V8	2	1.41	6.07×10^{-3}	2.16×10^4	3.06×10^{-3}	9.73×10^3	44.4
V9	2	1.41	6.07×10^{-3}	2.17×10^4	3.06×10^{-3}	1.02×10^4	22.2
V10	4	1.41	1.51×10^{-3}	5.31×10^3	6.07×10^{-3}	1.93×10^4	44.4

4.1 ERROR ASSESSMENT OF TRIPLE-JET MEASUREMENTS

The first cases ran were those listed in Table 5. For these cases, the probe was transversed in the y-z plane. Both CTA and CCA data were gathered simultaneously with a sample rate of 2 kHz at

1 mm increments in space. Data was gathered beyond the periphery of both jets to insure that all important trends were captured. Shown in Figure 36 is case H1, where $R = \frac{1}{2}$ and $\Delta T = 44.4^\circ\text{C}$. It is observed that the center jet velocity profile appears to be wider than expected. This unexpected behavior is rigorously investigated in Section 4.2. To validate the accuracy of the measurements found after application of the temperature corrected curve fit, they were compared against the controlled volumetric flow rate from the skid. Using Simpson's rule for numerical integration on the measured velocity profile, flow rate was calculated to be $0.01622 \text{ m}^3/\text{s}$, while the flow skid controls were set at $0.01505 \text{ m}^3/\text{s}$ (a 7.9% difference). To check these sources of error, cases H4 and H5 were considered since they had a larger center-to-center jet spacing, and therefore represented a scenario where the influence of the outer jets on the center jet could be neglected at a downstream distance so close to the jet nozzle ($x/D_{jet} = 0.09$). In addition, these two cases represent two different temperature ratios, allowing the impact of this factor to be explored as well. Case H4 with $R = \frac{1}{2}$, $\Delta T = 44.4^\circ\text{C}$, and $S/D_{jet} = 3.0$ is shown in Figure 37. For this case the volumetric flow rate programmed into the skid is $0.01505 \text{ m}^3/\text{s}$ while the measured volumetric flow rate was $0.0162 \text{ m}^3/\text{s}$ for an error of 11.4%. For Case H5 shown in Figure 40, which is identical to case H4 except the temperature difference is reduced to $\Delta T = 11.1^\circ\text{C}$, the experimentally measured volumetric flow rate was $0.0143 \text{ m}^3/\text{s}$ for an error of 5.2%.

With the large temperature gradients found in the triple-jet experiment, especially for spacings of $S = 1.41D_{jet}$ additional concern was spent investigating the difference in temporally congruent and spatially congruent velocity correction methods. Shown in Figure 39, the error is largest at the edges of the jets nearest the outlet. As measurements are taken further and further downstream the effect of the limited spatial resolution of the probe is reduced due to the mixing of the jets. The largest error is approximately 8 m/s and exists when the CTA is located in the

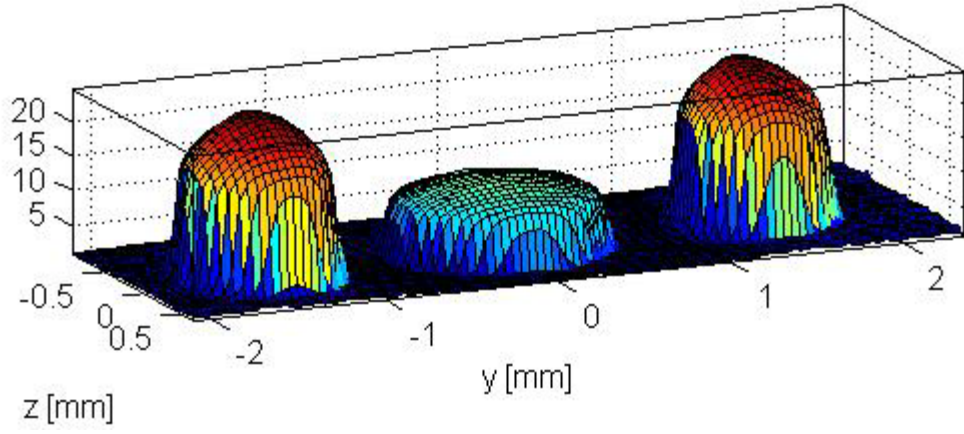
edge of the heated jets while the cold wire is still in the lower temperature ambient fluid. Further downstream near $x/D_{jet} = 10.09$ (Figure 39 (c)) the largest absolute velocity difference is approximately 1.5 m/s and occurs in the mixing region between the two distinct hot jets. The spatially collocated temperature and velocity profiles used in generating Figure 39 are shown subsequently in Figure 40 and Figure 41. It is valuable for validation to compare expected inlet conditions with measured inlet conditions. The expected inlet conditions and the inlet conditions actually measured are presented in Table 7. The expected centerline velocity is calculated based on Equation (22) where the volumetric flow rate is that programmed into the skid.

Table 7 – Errors in experimental inlet conditions

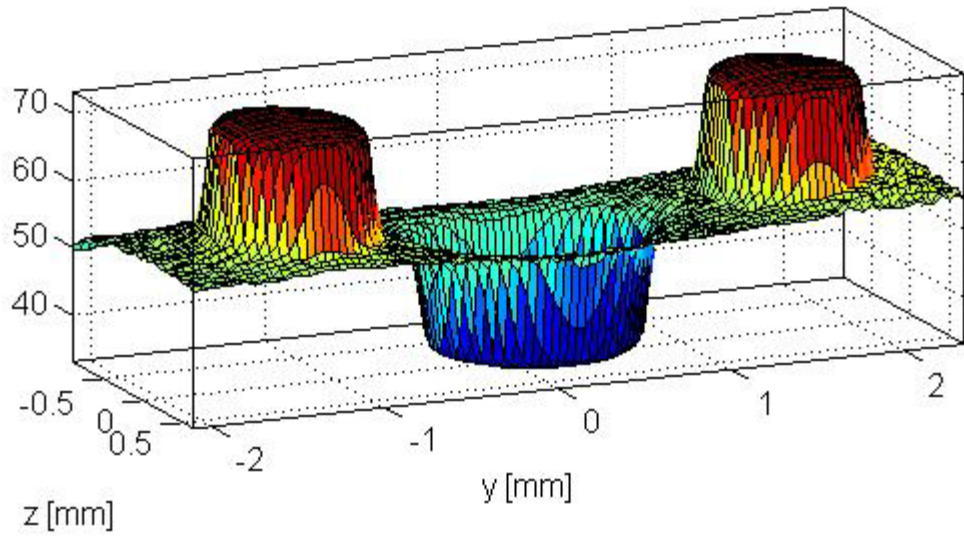
#	R	ΔT [°C]	S/D_{jet}	U_0 Expected [m/s]	U_0 Actual [m/s]	R Actual	T_{jet} [°C]	ΔT_{max} [°C]
H1	1/2	44.4	1.41	$U_{0,cold} = 9.59$ $U_{0,hot} = 19.18$	$U_{0,cold} = 12.18$ $U_{0,hot,1} = 24.18$ $U_{0,hot,2} = 24.64$	0.50	$T_{cold} = 32.81$ $T_{hot,1} = 72.97$ $T_{hot,2} = 72.22$	39.79
H4	1/2	44.4	3	$U_{0,cold} = 9.59$ $U_{0,hot} = 19.18$	$U_{0,cold} = 9.92$ $U_{0,hot,1} = 19.16$ $U_{0,hot,2} = 18.86$	0.52	$T_{cold} = 31.95$ $T_{hot,1} = 78.25$ $T_{hot,2} = 75.98$	45.16
H5	1/2	11.1	3	$U_{0,cold} = 9.59$ $U_{0,hot} = 19.18$	$U_{0,cold} = 9.63$ $U_{0,hot,1} = 19.60$ $U_{0,hot,2} = 19.31$	0.50	$T_{cold} = 29.39$ $T_{hot,1} = 39.66$ $T_{hot,2} = 40.39$	10.62
H6	∞	N/A	N/A	$U_{0,cold} = 9.59$	$U_{0,cold} = 13.77$	∞	$T_{cold} = 29.22$	N/A
V1	0	N/A	2.82	$U_{0,hot} = 19.18$	$U_{0,hot,1} = 20.84$ $U_{0,hot,2} = 20.71$	N/A	$T_{hot,1} = 41.89$ $T_{hot,2} = 42.31$	N/A
V2	1/2	44.4	1.41	$U_{0,cold} = 9.59$ $U_{0,hot} = 19.18$	$U_{0,cold} = 11.96$ $U_{0,hot,1} = 24.25$ $U_{0,hot,2} = 24.11$	0.49	$T_{cold} = 32.94$ $T_{hot,1} = 73.01$ $T_{hot,2} = 72.28$	39.70

Table 7 (continued)

V3	1/2	22.2	1.41	$U_{0,cold} = 9.59$ $U_{0,hot} = 19.18$	$U_{0,cold} = 10.48$ $U_{0,hot,1} = 21.40$ $U_{0,hot,2} = 21.35$	0.49	$T_{cold} = 30.83$ $T_{hot,1} = 51.07$ $T_{hot,2} = 51.00$	22.30
V4	1/2	44.4	3.00	$U_{0,cold} = 9.59$ $U_{0,hot} = 19.18$	$U_{0,cold} = 10.03$ $U_{0,hot,1} = 19.35$ $U_{0,hot,2} = 19.21$	0.52	$T_{cold} = 31.41$ $T_{hot,1} = 77.54$ $T_{hot,2} = 75.39$	45.05
V5	1/2	11.1	3.00	$U_{0,cold} = 9.59$ $U_{0,hot} = 19.18$	$U_{0,cold} = 9.67$ $U_{0,hot,1} = 19.39$ $U_{0,hot,2} = 19.15$	0.51	$T_{cold} = 29.59$ $T_{hot,1} = 39.78$ $T_{hot,2} = 40.39$	10.49
V6	1 ($Re_{jet} = 21.2 \times 10^3$)	44.4	1.41	$U_{0,cold} = 19.18$ $U_{0,hot} = 19.18$	$U_{0,cold} = 22.89$ $U_{0,hot,1} = 22.57$ $U_{0,hot,2} = 22.37$	1.02	$T_{cold} = 31.48$ $T_{hot,1} = 72.67$ $T_{hot,2} = 71.96$	40.83
V7	1 ($Re_{jet} = 10.6 \times 10^3$)	44.4	1.41	$U_{0,cold} = 9.59$ $U_{0,hot} = 9.59$	$U_{0,cold} = 11.16$ $U_{0,hot,1} = 12.22$ $U_{0,hot,2} = 12.12$	0.92	$T_{cold} = 32.32$ $T_{hot,1} = 71.98$ $T_{hot,2} = 72.41$	39.87
V8	2	44.4	1.41	$U_{0,cold} = 19.18$ $U_{0,hot} = 9.59$	$U_{0,cold} = 22.88$ $U_{0,hot,1} = 12.44$ $U_{0,hot,2} = 12.11$	1.86	$T_{cold} = 30.51$ $T_{hot,1} = 69.21$ $T_{hot,2} = 69.50$	38.85
V9	2	22.2	1.41	$U_{0,cold} = 19.18$ $U_{0,hot} = 9.59$	$U_{0,cold} = 21.11$ $U_{0,hot,1} = 11.01$ $U_{0,hot,2} = 11.10$	1.91	$T_{cold} = 29.38$ $T_{hot,1} = 49.64$ $T_{hot,2} = 49.97$	20.43
V10	4	44.4	1.41	$U_{0,cold} = 19.18$ $U_{0,hot} = 4.79$	$U_{0,cold} = 22.54$ $U_{0,hot,1} = 6.66$ $U_{0,hot,2} = 6.47$	3.43	$T_{0,cold} = 30.19$ $T_{0,hot,1} = 69.90$ $T_{0,hot,2} = 70.28$	39.90

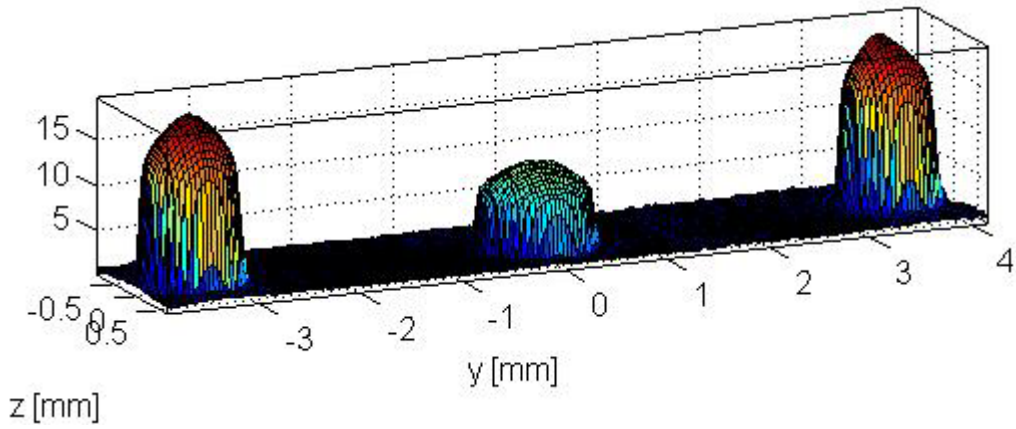


(a)

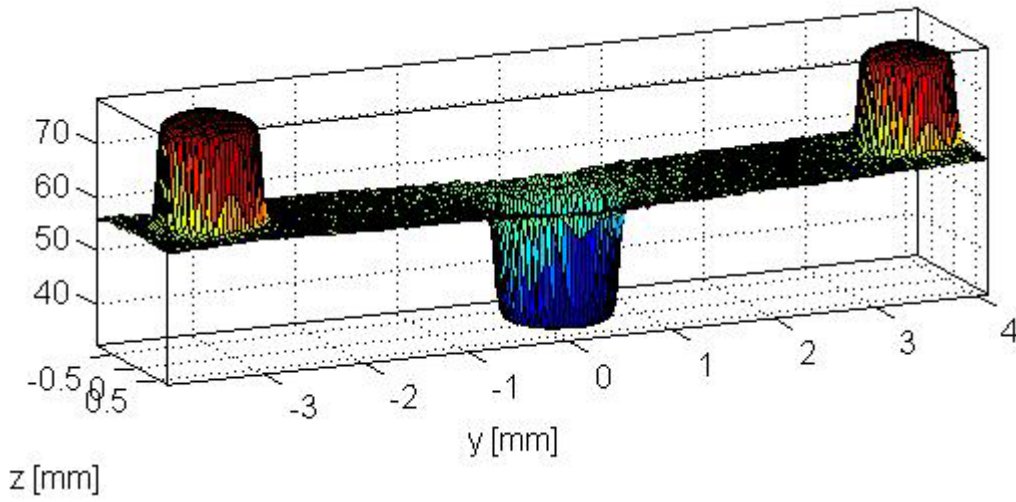


(b)

Figure 36 – Case H1: $R = 1/2$, $\Delta T = 44.4^\circ\text{C}$, $S/D_{jet} = 1.41$ measured at $x/D_{jet} = 0.09$ (a) profiles of velocity magnitude [m/s], and (b) temperature profiles [$^\circ\text{C}$]

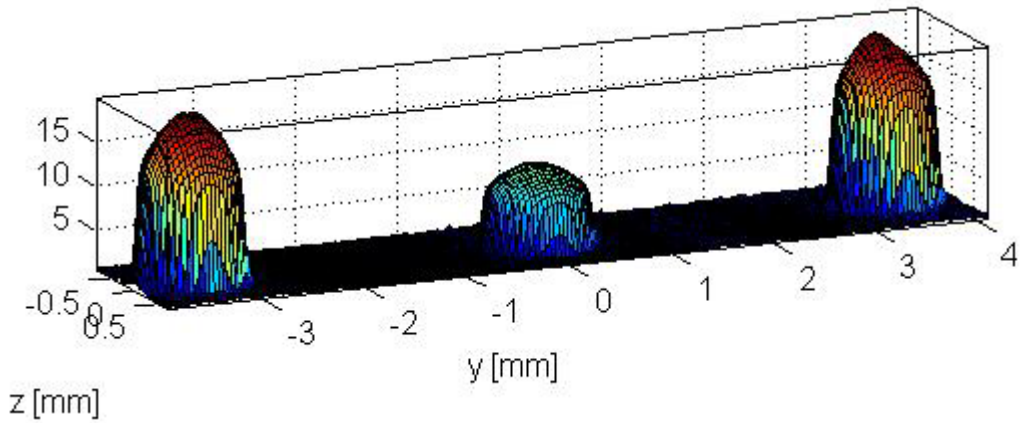


(a)

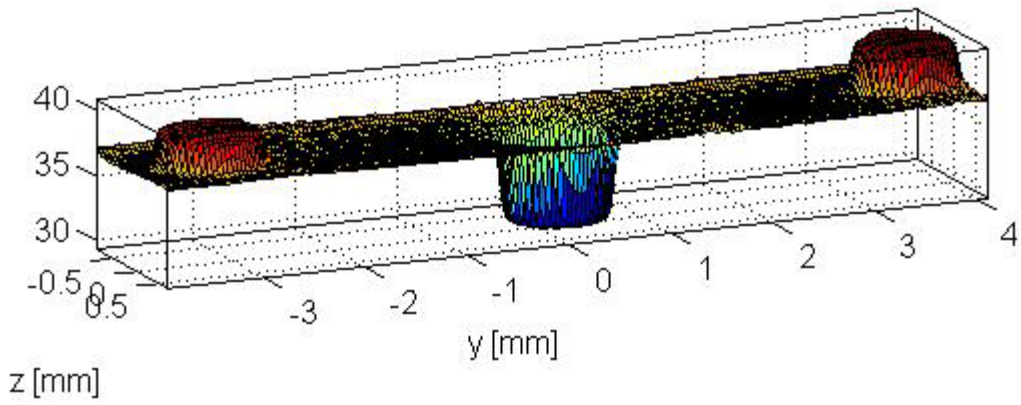


(b)

Figure 37 - Case H4: $R = \frac{1}{2}$, $\Delta T = 44.4^\circ\text{C}$, $S/D_{jet} = 3$ measured at $x/D_{jet} = 0.09$ (a) profiles of velocity magnitude [m/s], and (b) temperature profiles [$^\circ\text{C}$]

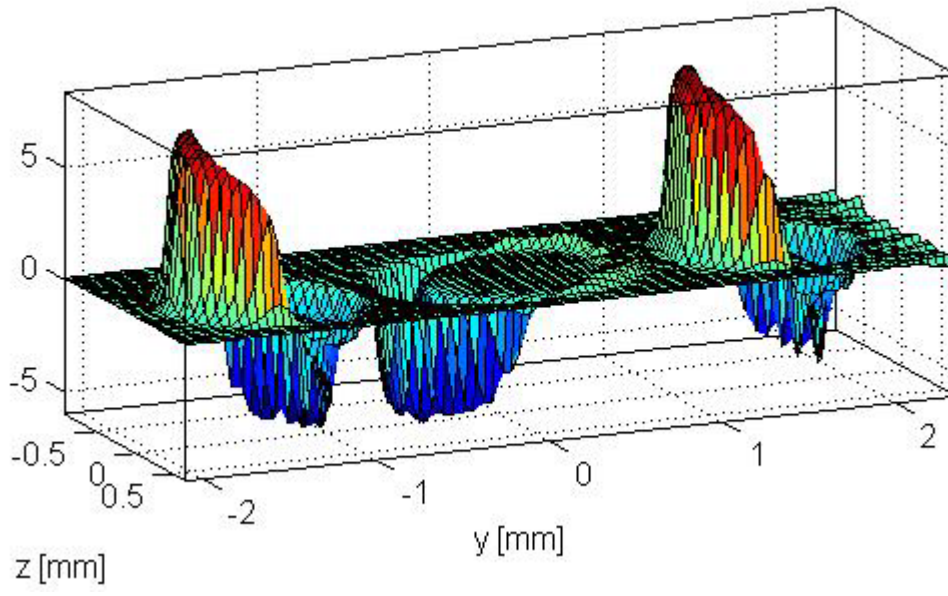


(a)

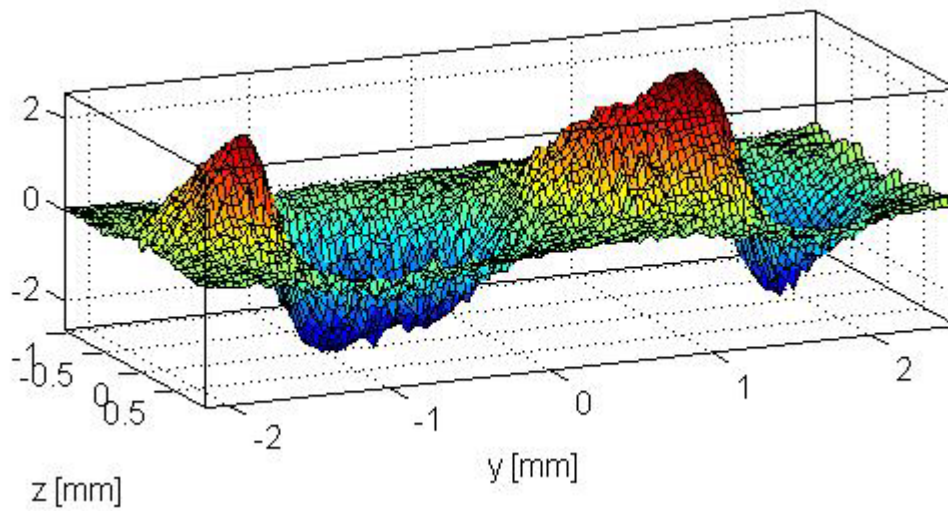


(b)

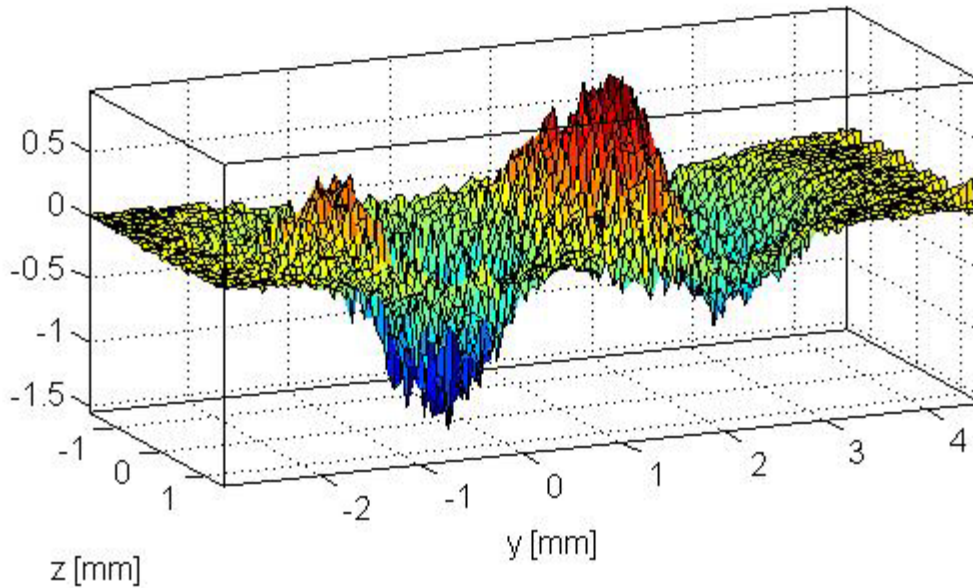
Figure 38 - Case H5: $R = \frac{1}{2}$, $\Delta T = 11.1^\circ\text{C}$, $S/D_{jet} = 3$ measured at $x/D_{jet} = 0.09$ (a) profiles of velocity magnitude [m/s], and (b) temperature profiles [$^\circ\text{C}$]



(a)



(b)

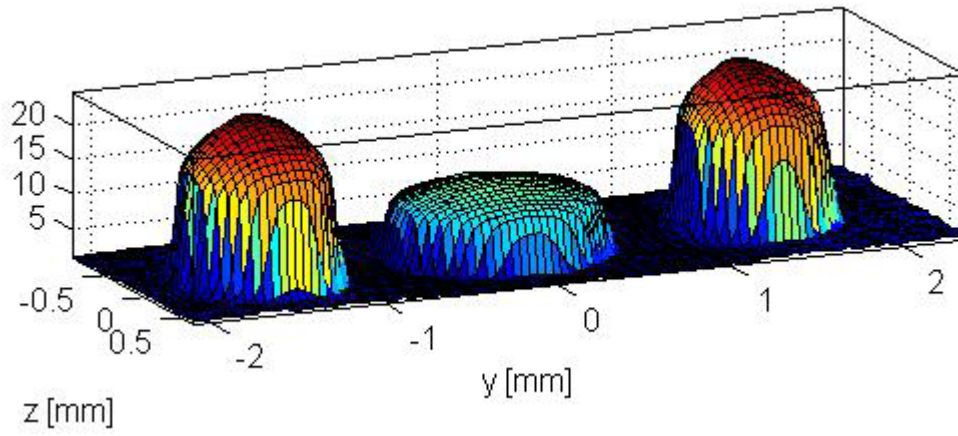


(c)

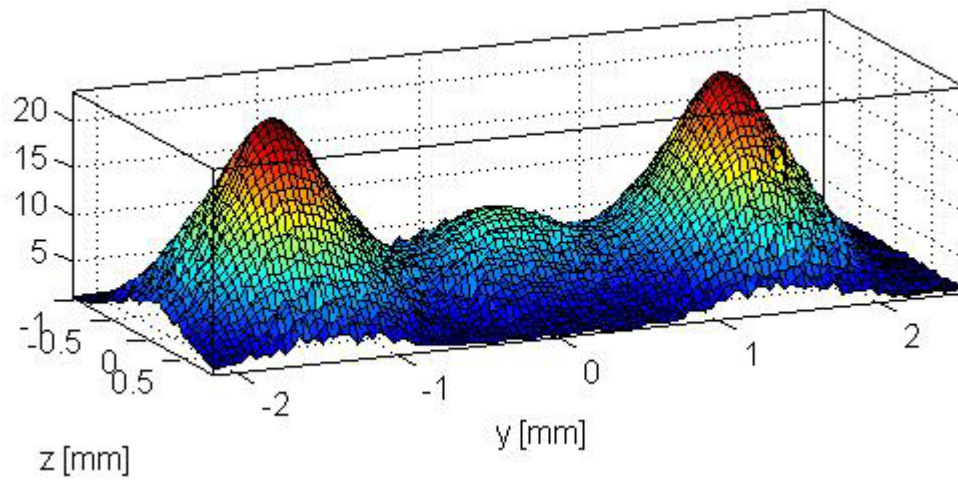
Figure 39 – Difference in temporally congruent and spatially congruent velocity correction methods [m/s] (a) case H1: measured at $x/D_{jet} = 0.09$, (b) case H2: measured at $x/D_{jet} = 5$, and (c) case H3: measured at $x/D_{jet} = 10$

4.2 ANALYSIS OF TRIPLE-JET FLOW PROFILES

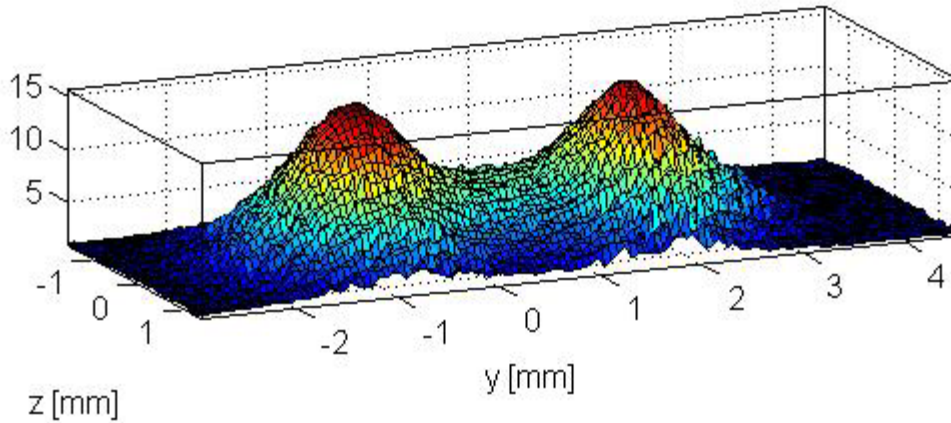
Of major concern in triple-jet behavior is the turbulent mixing of the jets. In order to study the mixing in the jets, profiles of the jets were considered first. As listed in Table 7 as cases H1, H2, and H3, data was gathered for three different downstream distances, $x/D_{jet} = 0.09$, 5.09, and 10.09 respectively. As illustrated in Figure 40 (a), the first cross-section shows three distinct jets. However by $x/D_{jet} = 5.09$ (Figure 40 (b)), the jets have begun to spread and mix significantly with only a small distinct cold peak existing where the center jet once had a prominent profile. This is further exacerbated by $x/D_{jet} = 10.09$, Figure 40, where there now only exists two distinct peaks associated with the hot outer jets.



(a)



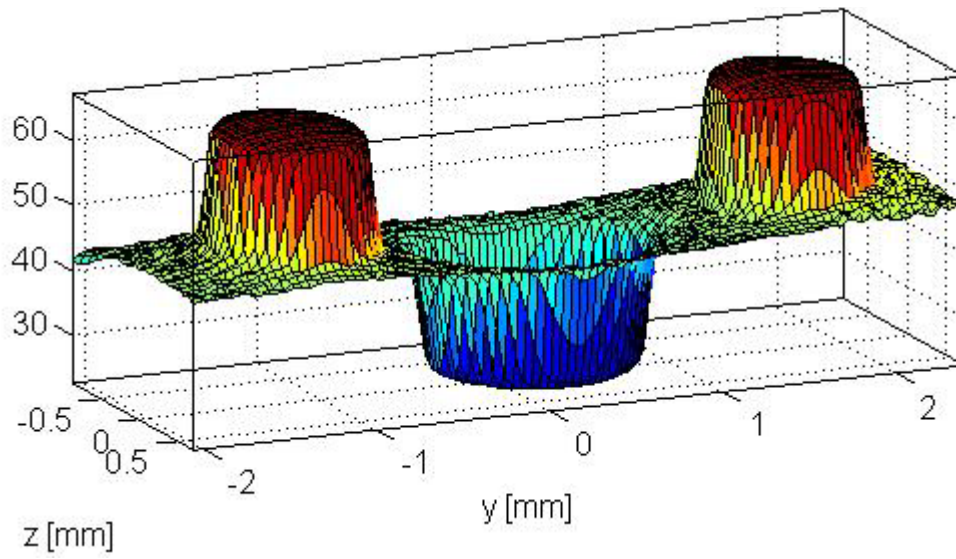
(b)



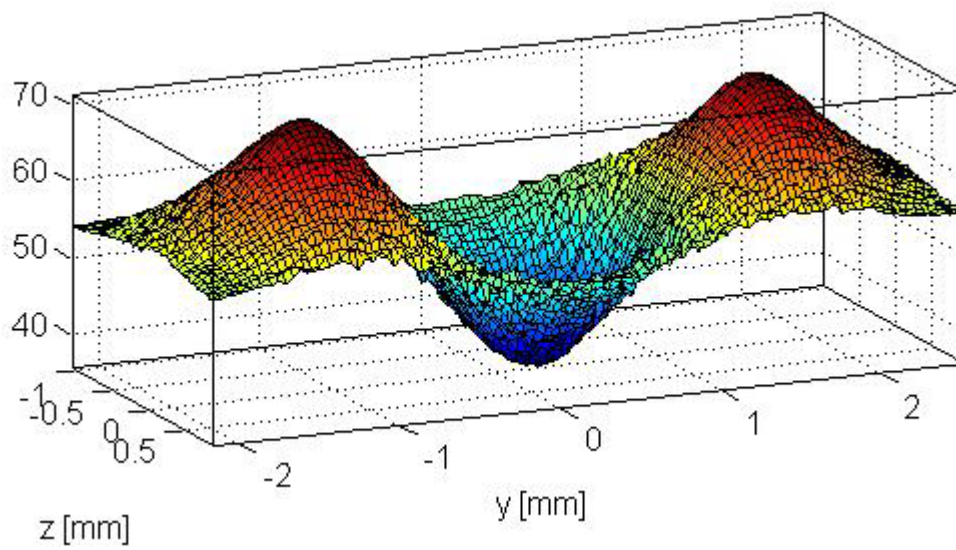
(c)

Figure 40 – Velocity contours [m/s] for $R = \frac{1}{2}$, $\Delta T = 44.4^\circ\text{C}$, $S/D_{jet} = 1.41$ (a) measured at $x/D_{jet} = 0.09$, (b) measured at $x/D_{jet} = 5.09$, and (c) measured at $x/D_{jet} = 10.09$

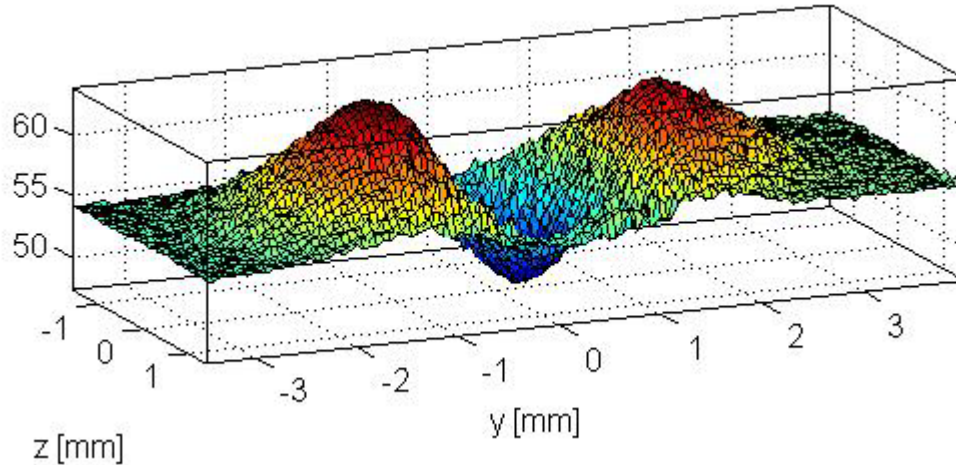
Considering contours of temperatures, similar trends are seen as those found with the velocity profiles. Shown in Figure 41 is the development of the triple-jet temperature profile at each of the three downstream planes for which data was captured. These uniquely represent case H1, H4, and H5 respectively. As observed in Figure 41 (a) the temperature profiles in both the hot jets and the cold is qualitatively a top-hat, in agreement with the single jet analysis conducted in Section 3.3. Looking in the downstream contours in Figure 41 (b) and (c) evidence of mixing is seen as the hot jet temperatures are spreading and decreasing as they mix with the cold jet whose temperature is increasing. Interestingly evident in both Figure 40 (a) and Figure 41 (a), the cold jet appears wider than both the hot jets in terms of temperature profile and velocity profile.



(a)



(b)



(c)

Figure 41 – Temperature contours [°C] for $R = \frac{1}{2}$, $\Delta T = 44.4^\circ\text{C}$, $S/D_{jet} = 1.41$ (a) measured at $x/D_{jet} = 0.09$, (b) measured at $x/D_{jet} = 5.09$, and (c) measured at $x/D_{jet} = 10.09$

To investigate the increased spreading of the center jet, line traces for each of the jets are gathered similar to that done in Figure 33. In order to sample the triple-jet inlet profiles in a logical manner, eight traces were taken of each jet then averaged with those traces with which symmetry was expected. The traces are shown in Figure 42 where a common nomenclature was used for all traces where symmetry was expected. Utilizing this sampling technique, profiles are shown for the H1 case in Figure 43. Investigating Figure 43 (b) the radius of the jet in the horizontal is approximately 10% larger than expected from the single jet curve fit. Conversely the jet appears to be oblong in profile as the single jet curve fit agrees well with the vertical traces. As would be expected for a jet stretching in the horizontal direction the average of the diagonal traces falls between that of the horizontal and vertical traces.

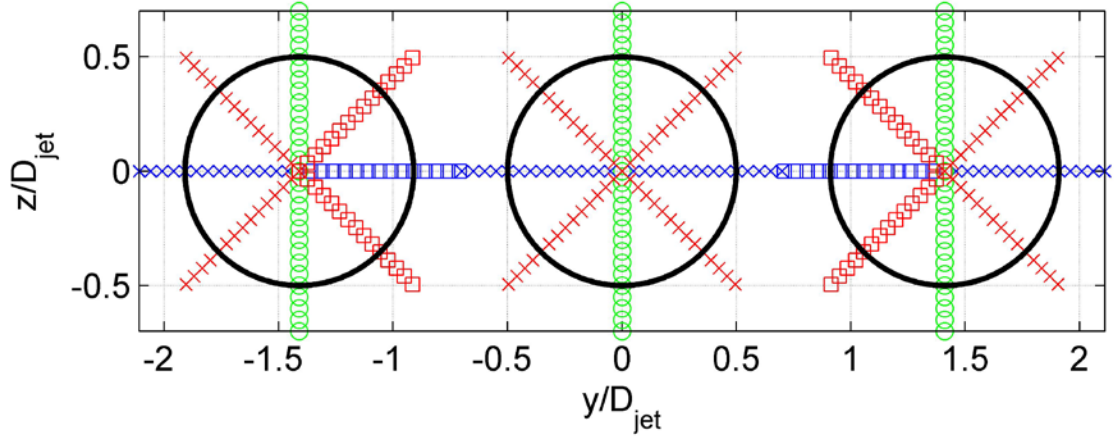


Figure 42 - Traces for triple-jet study and the averaging applied – \square inner horizontal averages, \times outer horizontal averages, \circ vertical averages, \square inner diagonal averages, \times outer diagonal traces. Black circle represents jet.

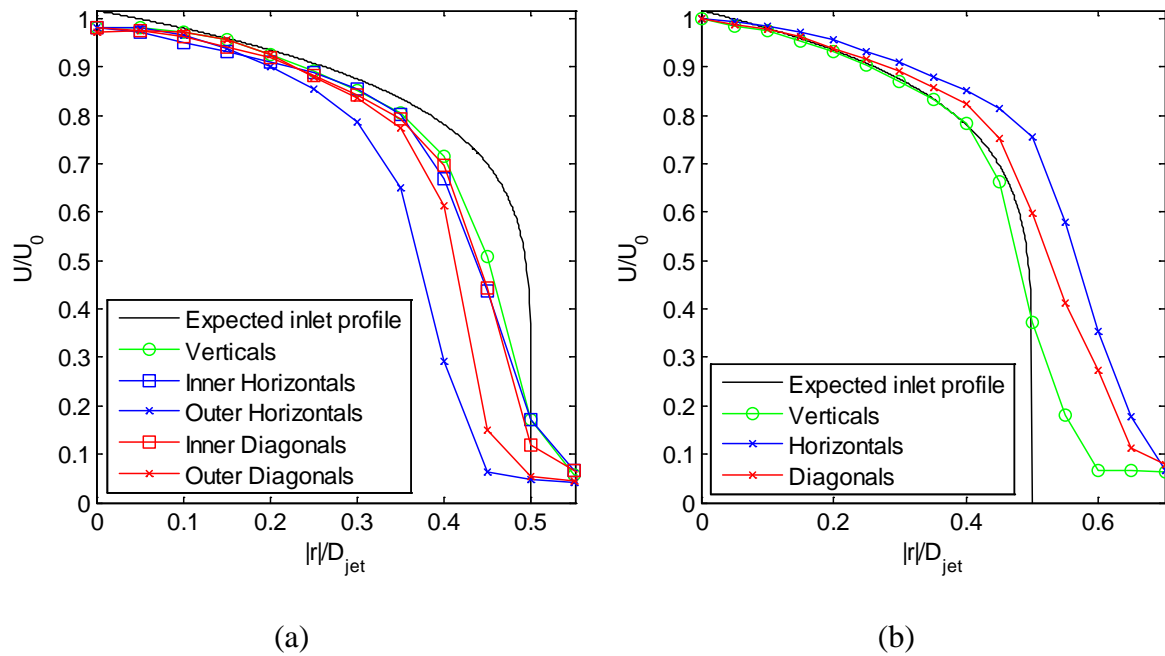


Figure 43 - Symmetrically averaged inlet profiles the case H1 measured at $x/D_{jet}=0.09$.
 (a) averaged traces for both hot jets, and (b) averaged traces for cold jet

Similar to the analysis done for the cold jet in Figure 43 (b) part (a) shows averages of the traces for the hot jets. Examining the profiles, it is first apparent that the hot jets appear much narrower than that of a single jet. However, more interesting is the trend in outer traces, both for

the horizontal and diagonal, which appear narrower than those for the vertical and horizontal traces. This suggests that the hot jets are “necking” in towards the cold jet even at distances of only $x/D_{jet} = 0.09$. Furthermore the cold jet is spreading horizontally towards the hot jets. To investigate if this is an effect of the tight jet spacing ($S/D_{jet} = 1.41$) similar analysis was conducted for cases H4 and H5 which having a non-dimensional jet spacing of $S/D_{jet} = 3.0$. Shown in Figure 44 and Figure 45 are the profiles for case H4 and H5 respectively.

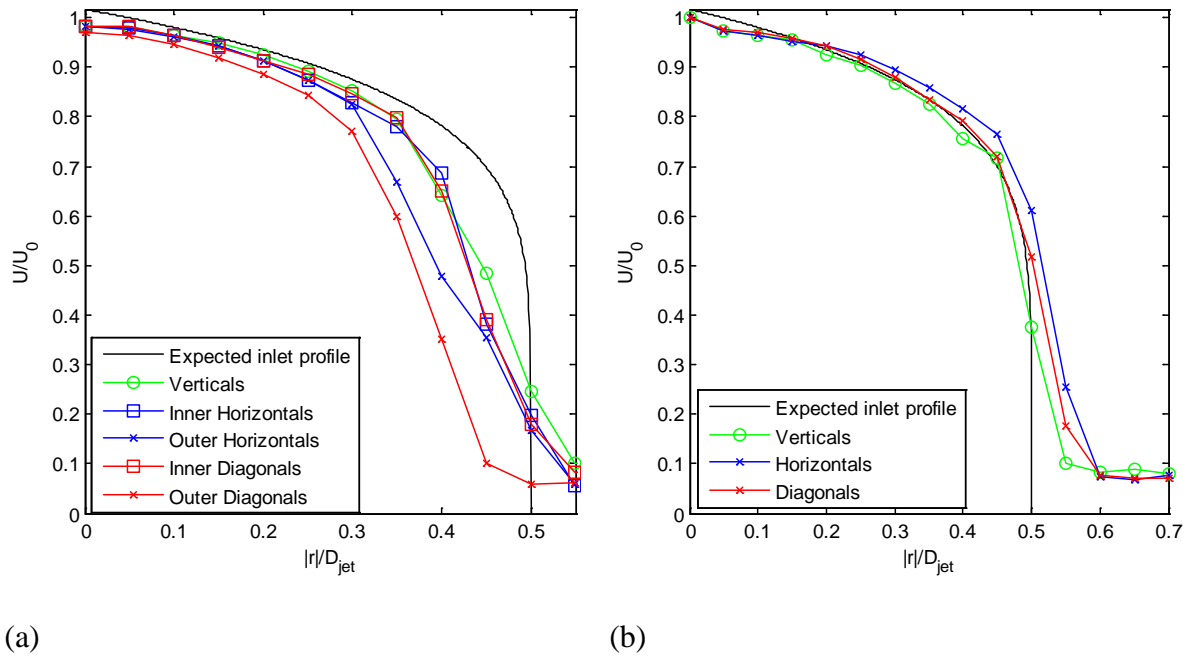


Figure 44 - Symmetrically averaged inlet profiles the case H4 measured at $x/D_{jet} = 0.09$. (a) averaged traces for both hot jets, and (b) averaged traces for cold jet

For the wider spacing in cases H4 and H5 (Figure 44 (b) and Figure 45 (b)) the cold jet inlet averages suggest that the cold jet does not spread as it does in the closer spaced case H1 (Figure 43 (b)). In fact it is observed that the jet behaves according to expectations. When looking at the hot jet inlet traces it is noticed for both case H4 and H5 that the profiles are slightly narrower than expected from the single jet measurements. Additionally, for case H4 there appears to be a slight degree of necking occurring in the hot jet, as evident by the outer

traces decreased velocity profiles seen in Figure 44 (a). This under-prediction of velocity on the outside of the triple jet is not likely due to the correction method. In all cases the CCA was offset from the CTA in the $-z$ direction. Thus when comparing temporally congruent and spatially congruent data the largest errors are not symmetric, but in fact occur in the $-z$ direction. For case H5 the hot jet appears narrower than expected but does not exhibit any necking towards the center jet. This necking is likely due to the symmetric behavior the triple-jet array. It seems plausible that as the number of jets in the array is increased the degree to which jets neck will decrease for jets closer to the center then compared to those closer to the end of the array. Furthermore changes in behavior may even exist for arrays with an odd number of jets compared to those with an even number of jets.

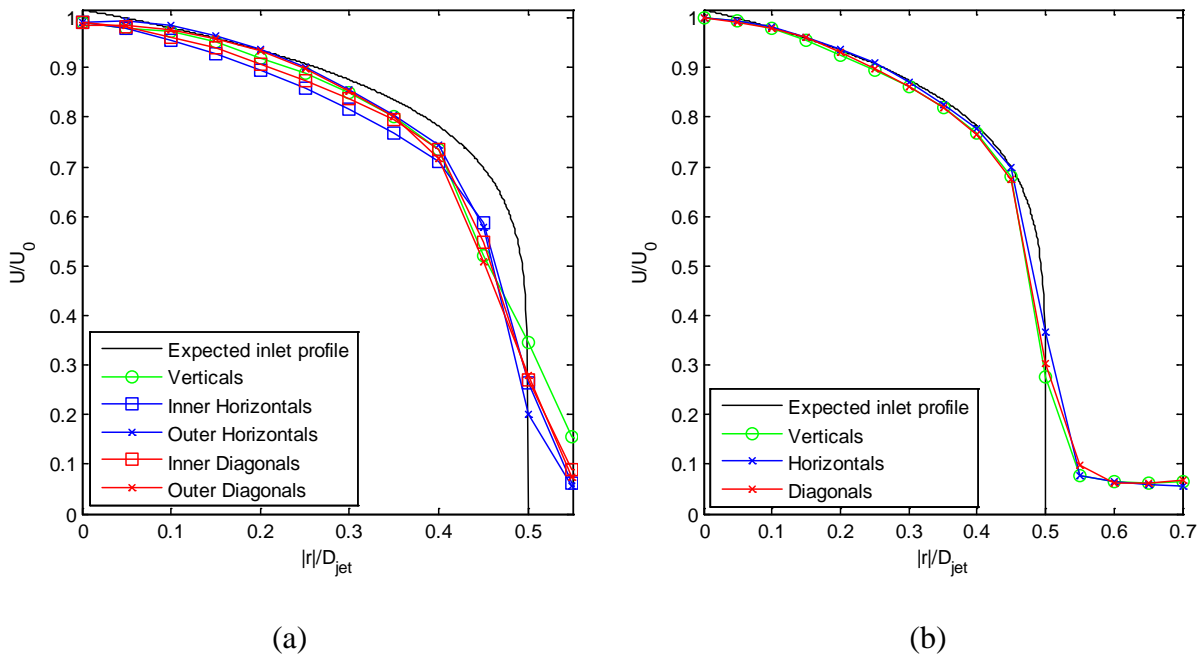


Figure 45 - Symmetrically averaged inlet profiles the case H5 measured at $x/D_{jet} = 0.09$.
 (a) averaged traces for both hot jets, and (b) averaged traces for cold jet

4.3 TRENDS IN THE TRIPLE-JET

In order to quantitatively talk about mixing in a parallel triple-jet vertical traces of multiple cases, shown in Table 6, were mapped in the xy -plane through $z = 0$. Contours of velocity and temperature data were gathered in the vertical plane. To compare the different behaviors of each case line traces were gathered at various downstream distances and symmetrically averaged to better understand trends in the temperature and velocity profiles. An example of these trends is shown in Figure 46 which is used to investigate the effect of temperature difference on the velocity profiles.

Shown in Figure 46 are symmetrically averaged velocity profiles normalized by the maximum velocity in the profile for different downstream distances. The cases presented were uniquely selected to represent three distinct velocity ratios, $R = \frac{U_{0,cold}}{\langle U_{0,hot} \rangle}$, each having two unique temperature differences. As shown by the close agreement between case V2 and V3, agreement between cases V3 and V5, and agreement between cases V8 and V9, the temperature difference does not have any apparent effect on the velocity profiles. Similar to the profiles shown in Figure 46, effort was taken to investigate how for these same cases the non-dimensional temperature profiles in the domain varied as a function of the temperature difference. The non-dimensional temperature was defined according to Equation (24). As shown in Figure 47 even at large downstream distances, there are no significant variations in the non-dimensional temperature profile in and near the periphery of the jet. However, in areas between and outside of the jets, the temperature appears to vary slightly from case to case. This difference can be attributed to different inlet temperatures and flow rates for the different cases. As the inlet boundary conditions were not the same in all cases, the average temperature in the test section changed to

case to case. To approximate the effects of each inlet condition on the test section temperature, the bulk inlet temperature was calculated for each case according to Equation (25). As anticipated, the cases with the largest observed peripheral temperatures also have the largest inlet bulk temperature. As the test section is an insulated box this is to be expected.

$$\theta = \frac{T - T_{inner}}{T_{outer} - T_{inner}} \quad (24)$$

$$T_{bulk} = \frac{\dot{V}_{hot,1}T_{hot,1} + \dot{V}_{hot,2}T_{hot,2} + \dot{V}_{cold}T_{cold}}{\dot{V}_{hot,1} + \dot{V}_{hot,2} + \dot{V}_{hot,1}} \quad (25)$$

Table 8 – Estimated bulk temperature of flow into test section for each case

#	U_o Expected [m/s]	T_{jet} [°C]	T_{bulk} [°C]	#	U_o Expected [m/s]	T_{jet} [°C]	T_{bulk} [°C]
V1	$U_{0,hot} = 19.18$	$T_{hot,1} = 41.89$ $T_{hot,2} = 42.31$	42.1	V6	$U_{0,cold} = 9.59$ $U_{0,hot} = 9.59$	$T_{cold} = 32.32$ $T_{hot,1} = 71.98$ $T_{hot,2} = 72.41$	58.9
V2	$U_{0,cold} = 9.59$ $U_{0,hot} = 19.18$	$T_{cold} = 32.94$ $T_{hot,1} = 73.01$ $T_{hot,2} = 72.28$	64.7	V7	$U_{0,cold} = 19.18$ $U_{0,hot} = 19.18$	$T_{cold} = 31.48$ $T_{hot,1} = 72.67$ $T_{hot,2} = 71.96$	58.7
V3	$U_{0,cold} = 9.59$ $U_{0,hot} = 19.18$	$T_{cold} = 30.83$ $T_{hot,1} = 51.07$ $T_{hot,2} = 51.00$	47.0	V8	$U_{0,cold} = 19.18$ $U_{0,hot} = 9.59$	$T_{cold} = 30.51$ $T_{hot,1} = 69.21$ $T_{hot,2} = 69.50$	49.9
V4	$U_{0,cold} = 9.59$ $U_{0,hot} = 19.18$	$T_{cold} = 31.41$ $T_{hot,1} = 77.54$ $T_{hot,2} = 75.39$	67.5	V9	$U_{0,cold} = 19.18$ $U_{0,hot} = 9.59$	$T_{cold} = 29.38$ $T_{hot,1} = 49.64$ $T_{hot,2} = 49.97$	39.6
V5	$U_{0,cold} = 9.59$ $U_{0,hot} = 19.18$	$T_{cold} = 29.59$ $T_{hot,1} = 39.78$ $T_{hot,2} = 40.39$	38.0	V10	$U_{0,cold} = 19.18$ $U_{0,hot} = 4.79$	$T_{0,cold} = 30.19$ $T_{0,hot,1} = 69.90$ $T_{0,hot,2} = 70.28$	47.4

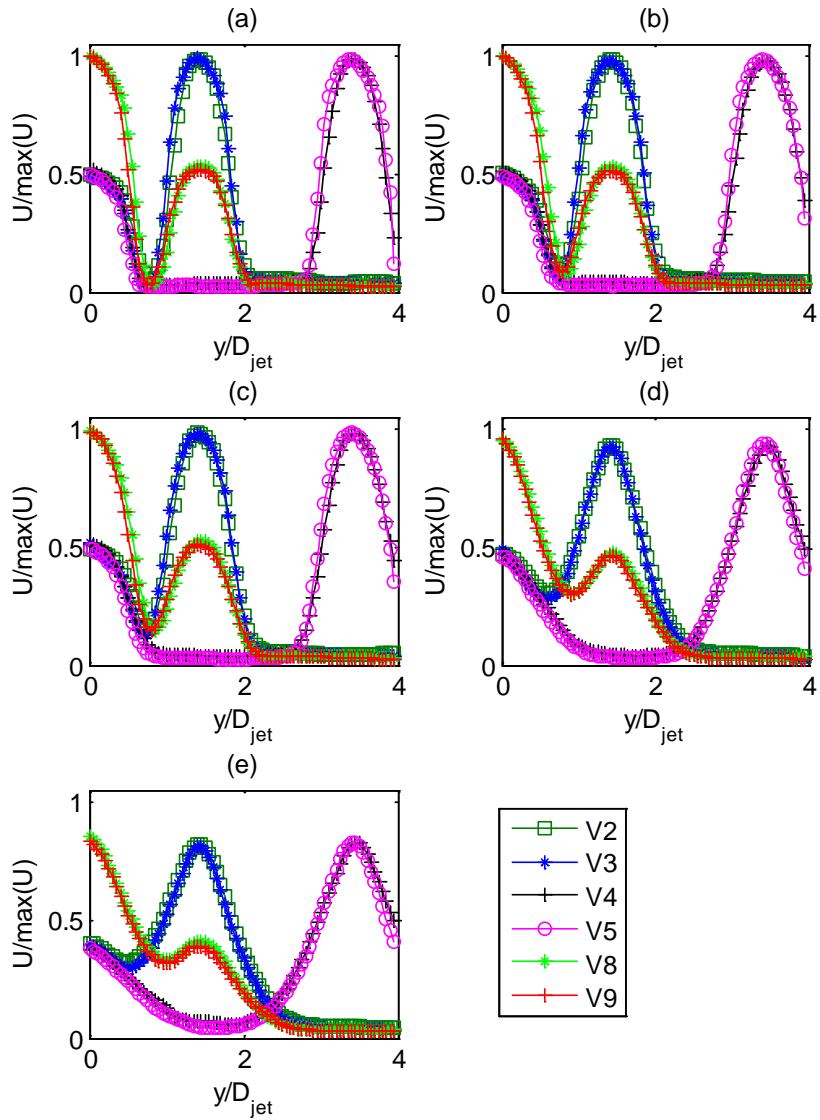


Figure 46 – Effects of temperature on the non-dimensional triple-jet velocity profile for different downstream distances (a) measured at $x/D_{jet} = 0.09$, (b) measured at $x/D_{jet} = 0.59$, (c) measured at $x/D_{jet} = 1.09$, (d) measured at $x/D_{jet} = 4.09$, and (e) measured at $x/D_{jet} = 6.09$

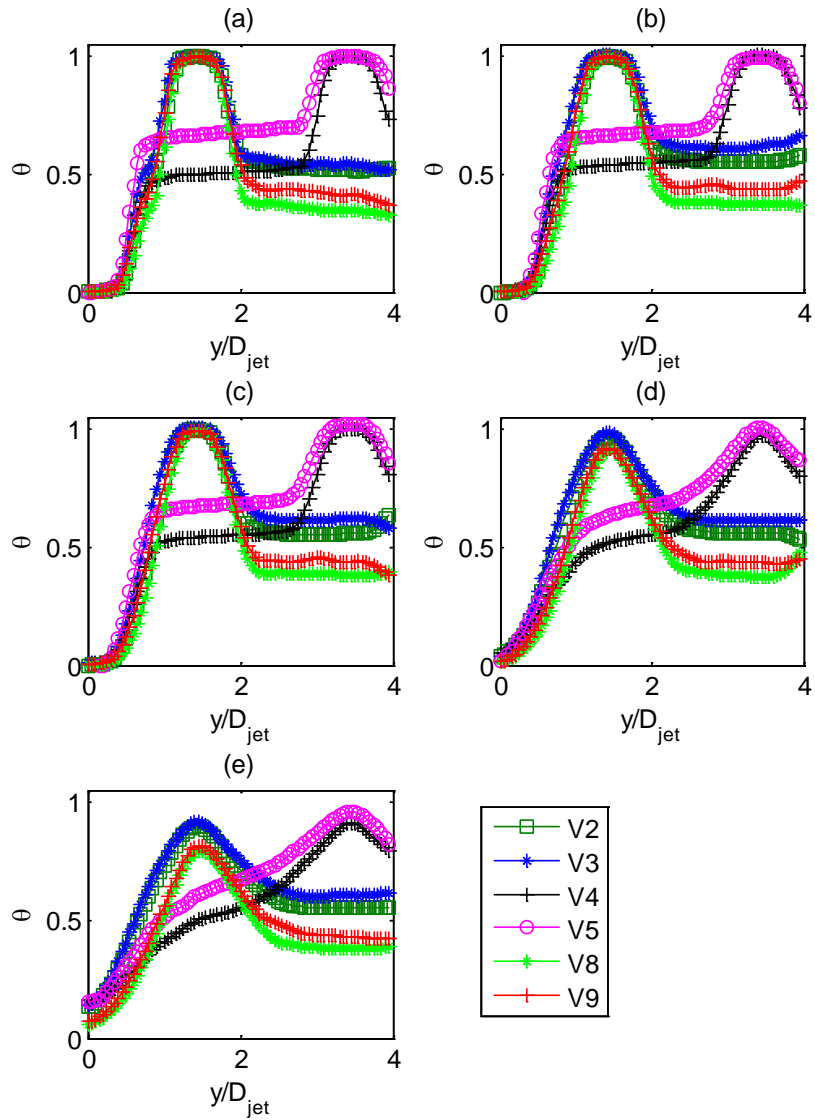


Figure 47 – Effect of temperature difference on the non-dimensional triple-jet temperature profiles at different downstream distances (a) measured at $x/D_{jet} = 0.09$, (b) measured at $x/D_{jet} = 0.59$, (c) measured at $x/D_{jet} = 1.09$, (d) measured at $x/D_{jet} = 4.09$, and (e) measured at $x/D_{jet} = 6.09$

While the profiles presented in Figure 46 and Figure 47 support the notion that the temperature behaves as a passive scalar, more detail about the triple-jet behavior can be examined by comparing cases for a fixed temperature difference where velocity ratio is varied.

This is the situation considered in Figure 48 where the temperature difference for all four cases shown is $\Delta T = 44.4^\circ\text{C}$. The first observation noticed is that for cases V6 and V7 there is very little difference. This suggests that for the limited range of jet velocities tested there is not a significant dependence of the flow field on the Reynolds number of the jets. However, by contrast there does appear to be significant differences associated with the velocity ratio. When comparing cases V2 and V8, several distinct trends are seen. It appears that in case V2, with $R = \frac{1}{2}$, the center jet has slightly narrowed compared to the $R = 1$ cases, while the opposite is true for case V8 in which the center jet is slightly wider than that of the isovelocity cases. One possible explanation for this behavior may be tied to single jet behavior. From early theoretical work on a free jet [37] we expect that in order to maintain momentum across the half width of the jet mass must be entrained. Thus, as the momentum of each outer jet is twice that of the center jet for $R = \frac{1}{2}$, it may be that the outer jets are entraining the center jet's mass into their own. In order to quantify this behavior it would be necessary to define the apparent width of each jet, and explain the complicated mechanism by which they combine. To aid in this analysis higher resolution experimental data, with multiple component velocity and stress measurements are suggested for future studies.

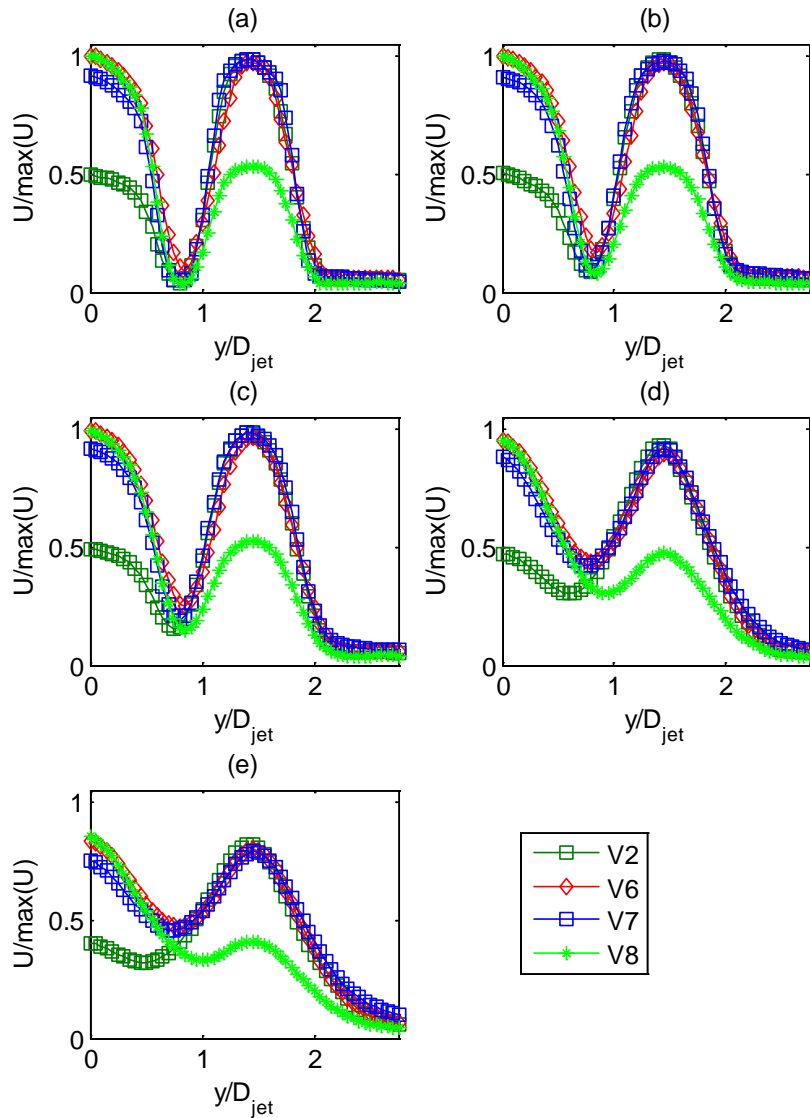


Figure 48 – Differences related to velocity ratio for triple-jet velocity profiles at different downstream distances (a) measured at $x/D_{jet} = 0.09$, (b) measured at $x/D_{jet} = 0.59$, (c) measured at $x/D_{jet} = 1.09$, (d) measured at $x/D_{jet} = 4.09$, and (e) measured at $x/D_{jet} = 6.09$

For the case of a parallel round triple-jet the effects of temperature difference, velocity ratio, and jet spacing on velocity and temperature profiles have been studied. It was seen that the temperature difference does present any significant impact on the velocity profiles measured in the jet. Moreover, any noticeable difference were less than those currently due to the uncertainty

associated with the dual CTA and CCA measurement compensation techniques. Furthermore, it has been seen that non-dimensional spacing does have an effect on the behavior of the center jet near the inlet. For the small $S = 1.41$ case the center jet appeared wider than expected. However, when increasing the spacing to $S = 3.0$ the center jet behavior near the inlet was as expected.

The qualitative assessment has provided additional understanding into the expected flow behavior in a round parallel triple-jet. Additionally, an unexpected physical behavior was observed for the spreading of a round jet. The present analysis provides encouraging results and suggests that future work should focus on more complete resolution of the flow field in the triple-jet as it is reasonable to expect the spacing of the jets influences and creates different flow regimes between the jets. Based on these observations first level approaches to validation and verification of turbulence models are possible. For future work care should be given to better understanding the physics associated with the spreading of the center jet and the effects on velocity profiles near the jet.

5.0 NUMERICAL MODELING OF A PARALLEL TRIPLE-JET

The parallel triple-jet will be modeling and validated against experiments using the Reynolds Averaged Navier-Stokes (RANS) model in OpenFOAM®. Open Field Operation and Manipulation (OpenFOAM), is an open source “toolbox” useful for solving partial differential equations. In the context of the proposed research, the coupled conservation of mass and balance of linear momentum (referred to as the Navier-Stokes equations), is of primary interest, and are provided for reference in Equations (26) and (27) for the case of incompressible flow, where \mathbf{u} is the velocity vector, ρ is the density, p is the pressure, and ν is the viscosity.

$$\nabla \cdot \mathbf{u} = 0 \quad (26)$$

$$\frac{\partial \mathbf{u}}{\partial t} + \mathbf{u} \cdot \nabla \mathbf{u} = -\frac{1}{\rho} \nabla p + \nu \nabla^2 \mathbf{u} \quad (27)$$

Equation (26), the divergence of the velocity field, represents the necessary and sufficient condition to ensure conservation of mass is satisfied for an incompressible flow field with constant density. Similarly, for incompressible flow, Equation (27) consists of a non-linear convective term on the right hand side, while on the left hand side a Laplacian of the velocity field accounts for viscous diffusion and a gradient of pressure represents the gradient of the

spherical component of the stress tensor which causes acceleration of the fluid down the gradient.

Several studies have been conducted, where OpenFOAM® has been utilized, and have aided in securing knowledge and experience in conducting various simulations. For example, a study on turbulent round jets in confinement [39] utilized the simpleFOAM solution algorithm, detailed in section 5.2.3, in conjunction with the Realizable k - ϵ turbulence model, detailed in section 5.2.2. However, to properly study non-isothermal triple-jets, modeling the temperature dependent fluid properties is essential. This can most easily be done by utilizing a polynomial temperature dependence of fluid properties, an approach outlined in a previous lower plenum study [4], or one of several thermophysical models currently available in OpenFOAM®. Additional aspects of the modeling investigate the applicability of various turbulence models and wall functions to flow in a round parallel triple-jet. Models examined include the k - ϵ realizable RANS model with and without wall functions, the Launder and Gibson RSM model including wall reflection terms with wall functions.

5.1 MESH DESIGN

Important to the accuracy of the results is the meshing of the domain as discretization errors can effect multiple steps of the solution procedures. Shown in Figure 49 is the numerical domain considered in the simulations. The width of the square domain is the same as that in the experimental facility. However, the downstream distances was truncated to more closely replicate the measurement region while still reducing the computation expenses. For all

simulations a symmetric quarter model was used. Following next is a description of the various turbulence models utilized in the present work and their implementation in OpenFOAM®.

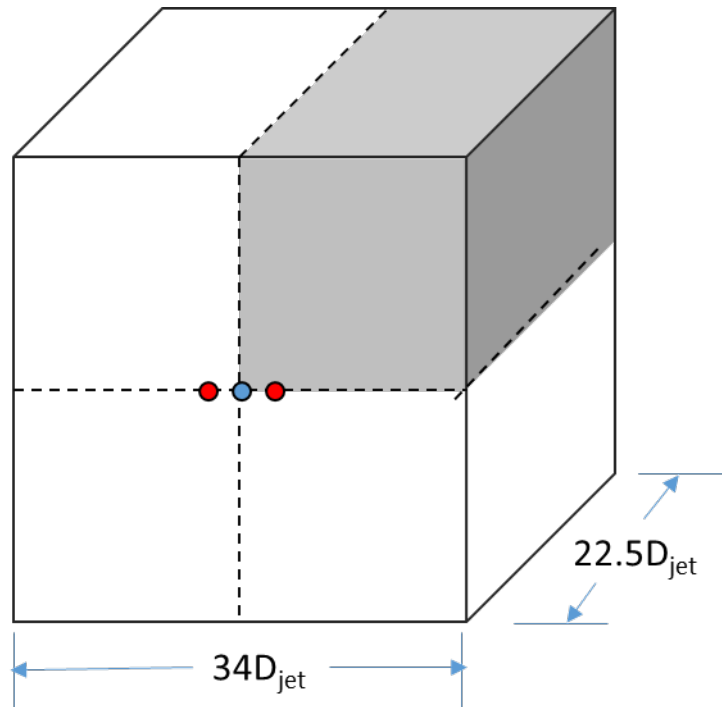


Figure 49 – Simulation domain. Lines: - walls, -- symmetry planes, hot jets, cold jets. Shaded section represents quarter model

In order to study systematically the effects of grid resolution on the results a standardized mesh structure was designed. The mesh structure is shown in Figure 50. The inclusion of an expanding region allowed for a reduced number of elements while a contracting mesh in the wall region allowed for improved prediction of velocity in the laminar regions. Cell-to-cell volumetric grading was fixed in both directions of the expanding mesh at 104%, while for the contractual wall mesh region the cell-to-cell volume grading was 90%. The number of cells in each region was then scaled based on the number of cell volumes present in the box inscribed in the center of each jet. The inscribed box was set based on experience to be half a jet diameter wide. Additionally while hexahedral elements were used in the majority of the domain, at the exact

interface between the radius of the jet and the first layer of cells outside of the radius polyhedral elements were used to allow for double the number of azimuthal elements in the shear layer. This is shown in Figure 51, where a blue and a red line has been super imposed to show the demarcation between the jet and the jet shear layer where increase in azimuthal elements occurs. Additionally a yellow line has been used to highlight the inscribed box at the center of each jet. A study of the mesh resolution, conducted utilizing Grid Convergence Index is presented in Section 5.3. For the RANS and RSM simulations all gradient and laplacian terms used Gauss linear differencing, while for divergence a Gauss upwind scheme was selected.

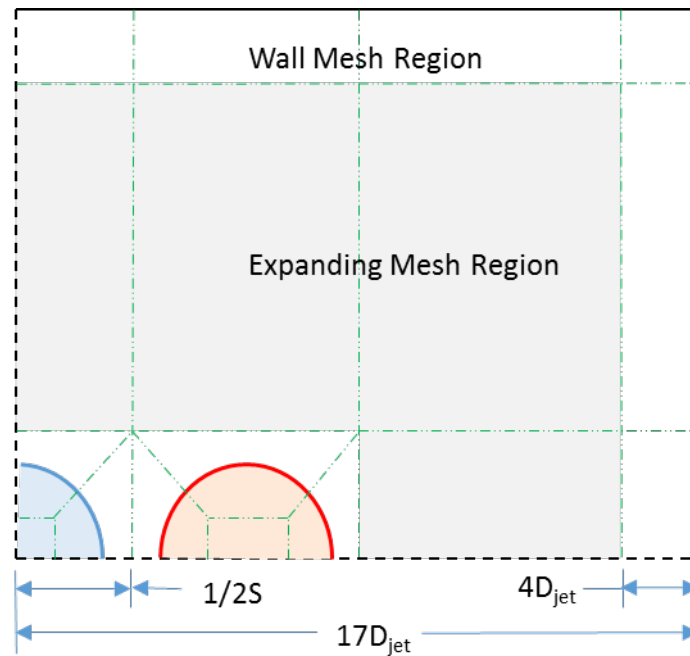


Figure 50 – Mesh structure. Lines: – walls, -- symmetry plane, cold jet, hot jet, -.- mesh regions

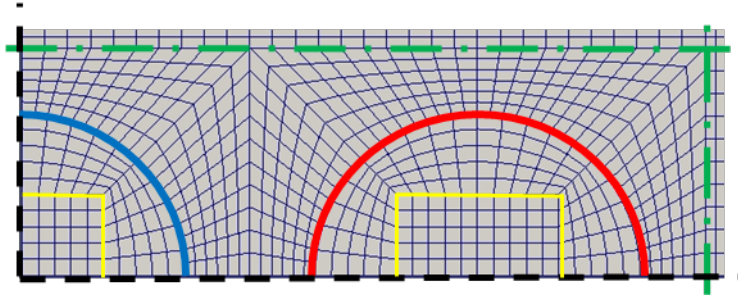


Figure 51 – Illustration of mesh layers between the jet and the shear layer. Lines: -- symmetry plane, cold jet, hot jet, -.- mesh regions, - inscribed box with 10 elements

5.2 SOLVER SELECTION AND TURBULENCE MODELING BACKGROUND IN OPENFOAM®

5.2.1 Reynolds-Averaged Navier Stokes Equations

In order to solve the Navier-Stokes equations (Equations (26) and (27)) several assumptions are made. First, Reynolds averaging is applied such that the velocity can be rewritten as $u = \langle u \rangle + u'$, where the brackets, $\langle \rangle$, represent ensemble averaging. With this assumption substituted back into the Equation (27), the well know RANS equations, shown in equations(28) and (29), are found. The assumption of a mean and fluctuation quantity introduces a new term, $\langle u'_i u'_j \rangle$, referred to as the Reynolds stress, which presents a closure problem, as there are now more variables than equations. As such, one common approach is to utilize a turbulent viscosity model for the Reynolds stress, shown in Equation (30) where $k = \frac{1}{2} \langle u'_i u'_i \rangle$. In the turbulent viscosity model, two new variables representing the turbulent kinematic viscosity, ν_t , and the kinetic energy, k , are introduced. Utilizing the turbulent viscosity model reduces the closure problem to

just two variables, requiring two new equations. The inclusion of the turbulent viscosity model and selection of the two new equations define the turbulence model used in the RANS solution.

$$\frac{\partial \langle u_i \rangle}{\partial x_j} = 0 \quad (28)$$

$$\frac{\partial \langle u_i \rangle}{\partial t} + \langle u_j \rangle \frac{\partial u_i}{\partial x_j} = \frac{-1}{\rho} \frac{\partial \langle p \rangle}{\partial x_i} + \frac{\partial}{\partial x_j} \left[\mu \left(\frac{\partial \langle u_i \rangle}{\partial x_j} + \frac{\partial \langle u_j \rangle}{\partial x_i} \right) - \langle u_i' u_j' \rangle \right] \quad (29)$$

$$-\langle u_i' u_j' \rangle = \nu_t \left(\frac{\partial \langle u_i \rangle}{\partial x_j} + \frac{\partial \langle u_j \rangle}{\partial x_i} \right) - \frac{2}{3} k \delta_{ij} \quad (30)$$

Similar to the averaging done for the Navier-Stokes equations, Reynolds averaging is also applied to the energy transport equations resulting in Equation (31), where $\alpha = \frac{k}{\rho C_p}$. As before, in order to do with closure issues associated with the stress term, $\langle u_j' T' \rangle$ OpenFOAM® employs a model, shown in Equation (32) where the laminar Prandtl number is $Pr = 0.7323$, and the turbulent Prandtl number was $Pr_t = 0.85$. For a history of this model and description of turbulent Prandtl number see [41]. For the solution of the heated jet Sutherlands law was utilized as a thermophysical model for the dynamic viscosity of the jet as shown in Equation (33). The form of the energy equation shown was utilized for all non-isothermal RANS solutions.

$$\frac{\partial \langle T \rangle}{\partial t} + \langle u_j \rangle \frac{\partial \langle T \rangle}{\partial x_j} = \alpha \frac{\partial}{\partial x_j} \left(\frac{\partial \langle T \rangle}{\partial x_j} \right) - \frac{\partial}{\partial x_j} \langle u_j' T' \rangle \quad (31)$$

$$\frac{\partial}{\partial x_j} \langle u_j' T' \rangle = \left(\frac{\nu}{Pr} + \frac{\nu_t}{Pr_t} \right) \frac{\partial}{\partial x_j} \left(\frac{\partial}{\partial x_j} \langle T \rangle \right) \quad (32)$$

$$\mu(T) = \frac{1.458 \cdot 10^{-6} \left[\frac{kg}{m \cdot s \cdot K^{1/2}} \right] T^{3/2}}{T + 110.4 [K]} \quad (33)$$

As OpenFOAM® uniquely implements each model following is a discussion of each including introductory details on their derivation. Specific attention is given to documenting the exact form of the equations as solved in OpenFOAM. Choice of a turbulence model for a parallel triple-jet is discussed next.

5.2.2 Realizable k-ε Turbulence Model

One common two equation turbulent viscosity model is the k-ε turbulence model, use of which requires solving a transport equation for kinetic energy, k , shown in Equation (34) with terms for production, turbulent kinetic energy flux, and dissipation are defined in Equations (35)-(37) respectively, all of which must be modelled in order to solve for the turbulent kinetic energy. Note that it is possible to derive the complete transport equation for turbulent dissipation, however it is considered a “modelled” equation being derived based on expected behavior not based on modeling of the exact transfer equation. For a thorough derivation of the transport of turbulent dissipation see Hanjalic and Launder [48].

$$\frac{\partial}{\partial t} k + \langle u_j \rangle \frac{\partial k}{\partial x_j} = \frac{\partial}{\partial x_k} \left[\nu_t \frac{\partial k}{\partial x_j} \right] - P_k + \frac{\partial}{\partial x_j} T_j - \varepsilon \quad (34)$$

$$P_k = \langle \overline{u'_i u'_j} \rangle \frac{\partial \langle u_i \rangle}{\partial x_j} \quad (35)$$

$$T_j = \left[\frac{1}{2} \langle u'_j u'_i u'_i \rangle + \frac{\langle u'_j p' \rangle}{\rho} - \nu \left\langle u'_i \left(\frac{\partial u'_j}{\partial x_i} + \frac{\partial u'_i}{\partial x_j} \right) \right\rangle \right] \quad (36)$$

$$\varepsilon = \frac{1}{2} \nu \left\langle \left(\frac{\partial u'_j}{\partial x_i} + \frac{\partial u'_i}{\partial x_j} \right)^2 \right\rangle \quad (37)$$

Several k- ε turbulence models have been previously developed and are well discussed in literature. . However, the standard k- ε model [40] has been shown to behaviour poorly when large adverse pressure gradients are present in the flow [41]. For this reason, several authors have suggested modifications, such as the inclusion of a non-constant C_μ [42]. Following this suggestion, one proposed change is known as the realizable k- ε model, proposed by Shih [43]. The transport equations implemented in OpenFOAM® for k and ε for the realizable k- ε model are shown in Equations (38) and (39), where $S_{ij} = \frac{1}{2} \left(\frac{\partial \langle u \rangle_i}{\partial x_j} + \frac{\partial \langle u_j \rangle}{\partial x_i} \right) - \frac{1}{3} \frac{\partial \langle u_k \rangle}{\partial x_k} \delta_{ij}$, $S = \sqrt{2S_{ij}S_{ij}}$, $C_1 = \max \left[0.43, \frac{\eta}{\eta + 5} \right]$ with $\eta = S \frac{k}{\varepsilon}$, and $C_2 = 1.44$. Note that in the realizable k- ε model, a non-constant definition of C_μ is used, as shown in Equation (41). As documented by Pope [44], the realizable k- ε model improves the prediction of the spreading of round jet, compared to the standard k- ε model. For this reason, the realizable k- ε model has been selected for use in uRANS simulations of a parallel, round triple-jet. After solution of both transport equations, the turbulent viscosity can be determined directly from to Equation (40), where the value of C_r is calculated according to Equation (41).

$$\frac{\partial}{\partial t} \langle k \rangle + \frac{\partial}{\partial x_j} \langle k u_j \rangle = \frac{1}{\rho} \left[\left(\nu + \frac{\nu_t}{\sigma_k} \right) \frac{\partial \langle k \rangle}{\partial x_j} \right] + \nu_t S_{ij} S_{ij} - \varepsilon \quad (38)$$

$$\frac{\partial}{\partial t} \varepsilon + \frac{\partial}{\partial x_j} \langle \varepsilon u_j \rangle = \frac{1}{\rho} \left[\left(\nu + \nu_t \right) \frac{\partial \langle \varepsilon \rangle}{\partial x_j} \right] + C_1 \langle S \varepsilon \rangle - C_2 \frac{\langle \varepsilon \rangle^2}{k + \sqrt{\nu \varepsilon}} \quad (39)$$

$$\nu_t = C_r \frac{k^2}{\varepsilon} \quad (40)$$

$$C_r = \frac{1}{4.04 + \sqrt{6} \cos \left(\frac{1}{3} \cos^{-1} \left(\sqrt{6} \frac{S_{ij} S_{jk} S_{ki}}{\sqrt{S_{ij} S_{ij}^3}} \right) \right)} \frac{k}{\varepsilon} \sqrt{S_{ij} S_{ij}} \quad (41)$$

After solving the governing equations for k and ε the turbulent viscosity calculated is then used to solve the modified RANS Equation (42). Note the kinetic energy term, $-\frac{2}{3}k\delta_{ij}$, originally included in Equation (30) is not present in the final solution. This is common in RANS turbulence models in OpenFOAM®.

$$\frac{\partial \langle u_i \rangle}{\partial t} + \langle u_j \rangle \frac{\partial u_i}{\partial x_j} + \frac{\partial \langle \frac{p}{\rho} \rangle}{\partial x_i} = \frac{\partial}{\partial x_j} \left[(v + v_t) \left(\frac{\partial \langle u_i \rangle}{\partial x_j} + \frac{\partial \langle u_j \rangle}{\partial x_i} \right) \right] \quad (42)$$

For the RANS simulations the velocity inlets considered were a parabolic profile, representing the extreme limit of laminar flow, and a tophat profile, being the extreme representation of a turbulent jet. For both velocity profiles the peak velocity magnitude was set in order to match the Reynolds numbers and mass flow rate seen in the experiments. Shown in Table 9 is the boundary conditions utilized for the RANS simulations. Note that the entries denoted as “By Case” are listed in Table 11 which describes the matrix of simulations run in the present work. The turbulent quantities v_t and α_t are set to be calculated at all boundaries. The turbulent intensity, I , was calculated based on the relationship for pipe flow shown in Equation (43). Note that for case T4 different conditions were utilized for k and ε . Additionally a unique version of the production term \mathbf{G} in the turbulent kinetic energy transport equation is incorporated. This is all discussed in Section 5.2.3.1.

$$I = 0.16 \text{Re}^{-1/8} \quad (43)$$

Table 9 - Boundary conditions for realizable k - ε model without wall functions

	$U(r)$	P	k	ε	T
Inlets	By Case	$\frac{\partial P}{\partial x_n} = 0$	$k = \frac{3}{2}(UI)^2$	$\varepsilon = \frac{C_{\mu}^{3/4} k^{3/2}}{0.07 D_{jet}}$	By Case
Walls	$U = 0$	$\frac{\partial P}{\partial x_n} = 0$	$k = 0$	$\varepsilon = 0$	$T = 300K$
Outlet	$\frac{\partial U_n}{\partial x_n} = 0$	$\frac{\partial P}{\partial x_n} = 0$	$\frac{\partial k}{\partial x_n} = 0$	$\frac{\partial \varepsilon}{\partial x_n} = 0$	$\frac{\partial T}{\partial x_n} = 0$

5.2.3 Reynolds Stress Transport Models

In an effort to improve upon the limitations in the realizable k - ε RANS model, an alternative approach to the closure problem in Equations (28) and (29) examines the transport of the Reynolds Stresses $\langle u_i u_j \rangle$ shown in Equation (44) coupled with a dissipation equation shown as Equation . In the Reynolds Stress Transport Equation, P_{ij} is production tensor, Equation (45), the velocity-pressure gradient tensor Π_{ij} is shown in Equation(46) , while the dissipation is defined according at Equation (47).

$$\frac{\partial \langle u'_i u'_j \rangle}{\partial t} + \langle u_k \rangle \frac{\partial}{\partial x_k} \langle u'_i u'_j \rangle + \frac{\partial}{\partial x_k} \langle u'_i u'_j u'_k \rangle = P_{ij} + \Pi_{ik} - \varepsilon_{ij} + \frac{\partial}{\partial x_k} \left[\nu \frac{\partial \langle u'_i u'_j \rangle}{\partial x_k} - \langle u'_i u'_j u'_k \rangle \right] \quad (44)$$

$$P_k = \langle \overline{u'_i u'_j} \rangle \frac{\partial \langle u_i \rangle}{\partial x_j} \quad (45)$$

$$\Pi_{ij} = -\frac{1}{\rho} \left\langle u'_i \frac{\partial p'}{\partial x_j} + u'_j \frac{\partial p'}{\partial x_i} \right\rangle \quad (46)$$

$$\varepsilon_{ij} = 2\nu \left\langle \frac{\partial u'_i}{\partial x_k} \frac{\partial u'_j}{\partial x_k} \right\rangle \quad (47)$$

In order to better understand conventional approaches to modeling the each term in Equation (44), the equations are often rewritten as shown in Equation (48). Upon examination of Equation (48) we see that it is necessary to model the dissipation tensor ε_{ij} , the first and third terms of the Reynolds-stress flux tensor T_{ijk} , and the pressure-rate-of-strain tensor R_{ij} .

$$\frac{\partial \langle u'_i u'_j \rangle}{\partial t} + \langle u_k \rangle \frac{\partial \langle u'_i u'_j \rangle}{\partial x_k} + \frac{\partial T_{ijk}}{\partial x_k} = P_{ij} + R_{ij} - \varepsilon_{ij} \quad (48)$$

$$T_{ijk} = \langle u'_i u'_j u'_k \rangle - \nu \frac{\partial \langle u'_i u'_j \rangle}{\partial x_k} + \frac{1}{\rho} \left(\langle u'_i p' \rangle \delta_{jk} + \langle u'_j p' \rangle \delta_{ik} \right) \quad (49)$$

$$R_{ij} = \left\langle \frac{p'}{\rho} \left(\frac{\partial u'_i}{\partial x_j} + \frac{\partial u'_j}{\partial x_i} \right) \right\rangle \quad (50)$$

The basic model for R_{ij} derived by Launder et al. [45], referred to as the isotropization of production model, is shown in Equation (51) where C_R is the Rotta constant, 1.8 and C_2 is taken to be 3/5. Note that the term W_{ij} accounts for wall reflections associated with inaccuracies with the modeling of dissipation tensor near the walls as shown in Equation (52). The unresolved terms of T_{ijk} are resolved using the simplified scalar diffusion model suggested by Daly and Harlows [46] as shown in Equation (53) with σ_R is 0.81967. The dissipation tensor, ε_{ij} is modeled according to Equation assuming isotropic turbulence where the scalar dissipation transport is modelled according to Equation (55) with $C_{\varepsilon 1}$, $C_{\varepsilon 2}$, and σ_ε equal to 1.8, 1.92, and

1.3 respectively. For an extensive explanation regarding the theory and approach of modeling the Reynolds stress transport equations see Pope [47] and Hanjalic and Launder [48].

$$R_{ij} = -C_R \frac{\varepsilon}{k} \left(\langle u'_i u'_j \rangle - \frac{2}{3} k \delta_{ij} \right) - C_2 \left(P_{ij} - \frac{1}{3} P_{mm} \delta_{ij} \right) + W_{ij} \quad (51)$$

$$W_{ij} = \begin{bmatrix} \left\{ C_1 \frac{\varepsilon}{k} \langle u'_k u'_m \rangle - C_2 C_1 \left(P_{km} - \frac{1}{3} P_{qq} \delta_{km} \right) \right\} n_k n_m \delta_{ij} \\ -\frac{3}{2} \left\{ C_1 \frac{\varepsilon}{k} \langle u'_k u'_i \rangle - C_2 C_1 \left(P_{ki} - \frac{1}{3} P_{qq} \delta_{ki} \right) \right\} n_k n_j \\ -\frac{3}{2} \left\{ C_1 \frac{\varepsilon}{k} \langle u'_k u'_j \rangle - C_2 C_1 \left(P_{kj} - \frac{1}{3} P_{qq} \delta_{kj} \right) \right\} n_k n_i \end{bmatrix} \frac{C_\mu^{3/4} k^{3/2}}{\kappa \cdot \varepsilon \cdot \Delta y} \quad (52)$$

$$T_{ijk} = - \left(\nu + \frac{C_\mu \sqrt{\frac{1}{2} \langle u'_l u'_l \rangle}}{\sigma_R \varepsilon} \right) \frac{\partial}{\partial x_k} \langle u'_i u'_j \rangle \quad (53)$$

$$\varepsilon_{ij} = \frac{2}{3} \delta_{ij} \varepsilon \quad (54)$$

$$\frac{\partial}{\partial t} \varepsilon + \langle u_j \rangle \frac{\partial \varepsilon}{\partial x_j} = \left(c_{\varepsilon 1} \frac{P_{ii}}{\varepsilon} - c_{\varepsilon 2} \varepsilon \right) \frac{\varepsilon}{k} + \frac{\partial}{\partial x_j} \left[\left(\frac{C_\mu \sqrt{\frac{1}{2} \langle u'_l u'_l \rangle}}{\sigma_\varepsilon \varepsilon} + \nu \right) \frac{\partial \varepsilon}{\partial x_j} \right] \quad (55)$$

After solving Equations (55) and (51) in that order, k is updated as $k = \frac{1}{2} R_{ii}$. The Navier-Stokes equations are then solved as shown in Equation (56). For this particular implementation in OpenFOAM® the divergence of R , the Reynolds stress, is included in the eddy viscosity model.

$$\frac{\partial \langle u_i \rangle}{\partial t} + \langle u_j \rangle \frac{\partial u_i}{\partial x_j} + \frac{\partial \left\langle \frac{p}{\rho} \right\rangle}{\partial x_i} = \frac{\partial}{\partial x_j} \left[(\nu + \nu_t) \left(\frac{\partial \langle u_i \rangle}{\partial x_j} + \frac{\partial \langle u_j \rangle}{\partial x_i} \right) \right] + \frac{\partial R_{ij}}{\partial x_j} \quad (56)$$

For the RSM simulation the boundary conditions used are shown in Table 10. The k and ε boundary conditions are discussed in more detail in Section 5.2.3.1, including a description of the modified production term incorporated into the kinetic energy equation.

Table 10 - Boundary conditions for RSM simulation

	$U(r)$	P	k	ε	R	T
Inlets	$U_{cold} = 7.72m/s$ $U_{hot} = 15.61m/s$	$\frac{\partial P}{\partial x_n} = 0$	$k = \frac{3}{2}(UI)^2$	$\varepsilon = \frac{C_{\mu}^{3/4} k^{3/2}}{0.07 D_{jet}}$	Mapped	$T_{cold} = 292.5K$ $T_{hot} = 339.3K$
Walls	$U = 0$	$\frac{\partial P}{\partial x_n} = 0$	$\frac{\partial k}{\partial x_n} = 0$	$\varepsilon = \frac{C_{\mu}^{3/4} k^{3/2}}{\kappa \Delta y}$	$\frac{\partial R}{\partial x_n} = 0$	$T = 300K$
Outlet	$\frac{\partial U_n}{\partial x_n} = 0$	$\frac{\partial P}{\partial x_n} = 0$	$\frac{\partial k}{\partial x_n} = 0$	$\frac{\partial \varepsilon}{\partial x_n} = 0$	$\frac{\partial R}{\partial x_n} = 0$	$\frac{\partial T}{\partial x_n} = 0$

5.2.3.1 RANS/RSM Wall Functions

One common problem with RANS solutions, as well as all turbulence modeling, is the ability to resolve the wall shear velocity when the size of the finite volume nearest the wall is larger than that necessary to resolve the boundary layer thickness. The resolution of the boundary layer has the most significant effect on drag predictions and wall heat transfer predictions. The sensitive of the results to the mesh resolution can be attributed to the “law of wall,” illustrated in Figure 52.

As shown, the skin velocity, $u^+ = \frac{|U|}{U_{\tau}}$ where U_{τ} is the friction velocity defined according to

Equation (57). In order to correct for the behaviour in skin velocity, a new definition of turbulent viscosity in the wall region is implemented. The turbulent viscosity was calculated for $y^+ < y_{laminar}^+$ according to Equation (60) where y^+ and $y_{laminar}^+$ are calculated according to Equations (58) and (59).

$$U_\tau = \sqrt{\nu \left. \frac{d\langle U \rangle}{dy} \right|_{y=0}} \quad (57)$$

$$y^+ = C_\mu^{1/4} \Delta y_1 \left(\frac{k}{\nu} \right) \quad (58)$$

$$y_{\text{laminar}}^+ = \frac{\log(11 \cdot 9.8)}{\kappa} \quad (59)$$

$$\nu_{t,wall} = \nu \left(\frac{y^+ k}{\ln(9.8 y^+)} - 1 \right) \quad (60)$$

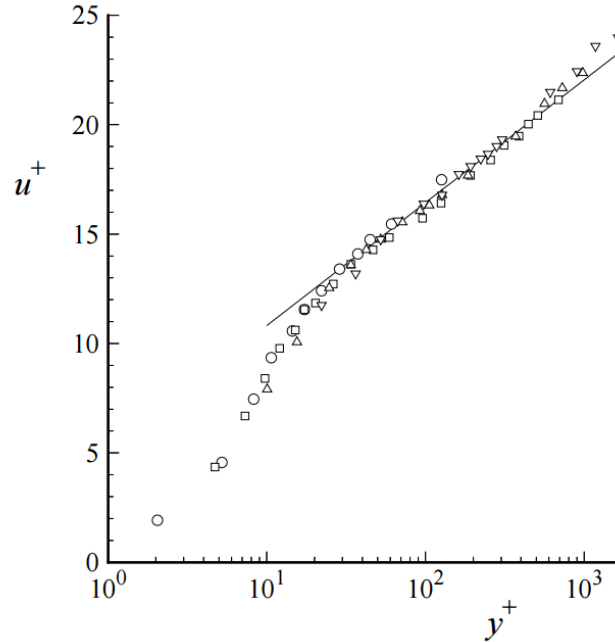


Figure 52 - Mean velocity profiles in fully-developed turbulent channel flow measured by Wei and Willmarth [49]. \circ , $Re_0 = 2,970$; \square , $Re_0 = 14,914$; Δ , $Re_0 = 2,970$; ∇ , $Re_0 = 39,582$; line, the log law (Taken from Pope [47]).

For the dissipation boundary conditions near the wall an explicit formula, based on the grid height Δy and the turbulent kinetic energy, is solved according to Equation (61). Additionally, at the wall the production term G in Equation (38) is modified as shown in

Equation (62) [50]. Note that these wall functions are implemented on both the upstream wall and the boundary walls for one RANS simulation and for all RSM simulations.

$$\varepsilon = \frac{C_{\mu}^{3/4} k^{3/2}}{\kappa \Delta y} \quad (61)$$

$$G = (\nu_t + \nu) |\nabla \mathbf{u}| \frac{C_{\mu}^{1/2} \sqrt{k}}{\kappa y} \quad (62)$$

5.2.4 Steady State Solution (RANS) - buoyantSimpleFoam

The simpleFoam algorithm is an implementation of the finite-volume based Semi-IMPlicit Pressure Linked Equation (SIMPLE) algorithm originally developed by Patankar & Spalding [51]. The SIMPLE algorithm, a standard steady state algorithm already implemented in OpenFOAM ®. For details of the implementation of this algorithm in OpenFOAM ® see, for example, Jasak [52]. The Semi-IMPlicit Pressure LinkEd algorithm, [SIMPLE], is an iterative solution procedure for solving the steady state Navier-Stokes equations for balance of linear momentum (Equation (27)). The solution method takes advantage of the fact that it possible to decouple the linear velocity-pressure relation when changes are large. It is assumed that pressure and velocity can be written as shown in Equations (63) and (64) respectively, where the prime (*) denotes a correction and the subscript (o) denotes the original guess, or the value from the previous time step. Substituting Equations (63) and (64) into the momentum equation, neglecting non-linear terms and accounting for conservation of mass (Equation (26)), an equation for velocity correction, Equation (65), and a *pressure correction equation*, Equation (67), are derived. Note in Equation (67) that A is a fictitious time increment divided by the density of the fluid. The value for p^* is then used in Equation (63) to correct the pressure.

$$p = p_o + p^* \quad (63)$$

$$\mathbf{u} = \mathbf{u}_0 + \mathbf{u}^* \quad (64)$$

$$\mathbf{u}^* = A \frac{\partial p^*}{\partial \mathbf{x}} \quad (65)$$

$$T = T_0 + f(\mathbf{u}^*) \quad (66)$$

$$\nabla^2 p^* = \frac{1}{A} (\nabla \cdot \mathbf{u}_0) \quad (67)$$

At the start of the SIMPLE algorithm, an approximate solution of the momentum equation (Equation (27)) is calculated using the initial values set for pressure. At this step the solution is under-relaxed. In OpenFOAM® the under-relaxation is done using an implicit method which enhances diagonalization of the matrix equations corresponding to the domain. For non-isothermal flows, the energy equation is then updated using the updated velocities (Equation (66)), before the momentum correction is applied. A pressure correction and momentum correction are applied. After the pressure is corrected, it is under-relaxed according to Equation (68), which is a modification of the original equation for pressure (Equation (63)). Note that the under-relaxation factor, α , varies from 0 to 1, with 0 corresponding to no change in the pressure, and 1 being the pressure equation given in Equation (63). The momentum corrector is applied as shown in Equation(65). After the pressure and momentum correctors have been applied, the process is repeated, starting with recalculating velocities based on the new pressure.

$$p^{new} = p_0 + \alpha (p^*) \quad (68)$$

5.3 GRID CONVERGENCE INDEX (GCI)

As the simulations are to be directly compared to experimental data with appropriately quantified experimental error and uncertainty, it is also necessary to determine a method to

gauge mesh independence and the numerical uncertainty. This can be done by utilizing the grid convergence index (GCI), a modified version of the Richardson Extrapolation [53]. The Grid Convergence Index study allows for an uncertainty, due to the mesh refinement level, to be placed on any relevant data. However, one drawback of GCI is the need for multiple grid refinements for comparison, which inevitably takes increased computational resources for each increasingly refined mesh. Grid Convergence Index assumes the error of the solution is in the asymptotic region, namely that the error decreases as a function of the local mesh scale according to Equation (69), where ε is the error, h is the local length scale, and p is the order of the discretization method used. The local length scale can be defined as the cube root of volume of the cell containing the particular point of interest.

$$\varepsilon \propto h^p \quad (69)$$

Once an important quantity is identified (e.g., centerline velocity at a specific axial location), data from three unique meshes are then compared to determine the uncertainty associated with the solution. The relative error between any two meshes can be calculated from the difference between the parameter of interest (ϕ). Note that for all equations relating to GCI, any two number subscript represents the difference between two cases: i.e. $\varepsilon_{32} = \phi_3 - \phi_2$. After determining the error, the local refinement between the two cases is calculated as $r_{21} = \frac{h_2}{h_1}$. When referring to the different meshes it is assumed that for the number of elements, N_i , $N_1 > N_2 > N_3$ and that $h_1 < h_2 < h_3$ accordingly. Next, the apparent order of the discretization method is calculated according to Equation (70), where $s = \text{sgn}\left(\frac{\varepsilon_{32}}{\varepsilon_{21}}\right)$. A negative value of s suggests

oscillatory convergence is occurring at that particular location. As shown, p must be determined using an iterative method.

$$p = \frac{1}{\ln(r_{21})} \left| \ln \left| \frac{\varepsilon_{32}}{\varepsilon_{21}} \right| + \ln \left(\frac{r_{21}^p - s}{r_{32}^p - s} \right) \right| \quad (70)$$

Finally, once the apparent order is known, the GCI for the refined mesh can be calculated according to Equation. (72), where FS is a factor of safety tied to the fact that it is unknown whether the solution is truly in the asymptotic region. A factor of safety suggested by Celik [54] is 1.25. This methodology was previously implemented in a study of laminar round jets issuing into a coaxial round confinement [55].

$$GCI_{21} = \frac{FS}{r_{21}^p - 1} \left| \frac{\phi_1 - \phi_2}{\phi_1} \right| \quad (71) \quad (72)$$

For the current work a GCI study was conducted on case P5, which was presented in Table 11. For the study three unique meshes with 4, 6, and 10 elements in the inscribed jet box, highlighted in yellow in Figure 51 were created. For each mesh the simulation was run until the residuals in the SIMPLE loop had maintained a constant value for 1000 iterations. Utilizing a global order of the method, P equal to the mean of p for each grid point and considering only the centerplane it was found the average uncertainty due to grid discretization is 1.31% while the maximum error is much larger, approximately 35,000%. This large uncertainty, which occurs in the shear layer near the wall between the jets, can be attributed to the low velocity and sensitivity of the flow results to the mesh in this region, a known problem with GCI [53]. A better understanding of the overall uncertainty along the center place is gathered by considering that 95.2% of the points have an uncertainty less than the mean while 98.3% of the data has an uncertainty of less than 5%.

5.4 SIMULATION RESULTS

One advantage of simulations is the ability to control and manipulate flow parameters that may not be controllable during actual experimentation. One example is inlet velocity profile. Despite careful design practices when planning an experiment, it is not possible to fully ensure the jet velocity profile nor is it easy to change if a specific end goal is in mind. However, with simulations this is easy to manipulate allowing for careful studies to be done on the effect of such a parameter. However, this can be sensitive to poor modeling practices so results need to always be considered carefully before drawing conclusions. Detailed explanation of the modeling practices utilized in the current study are examined in Sections 5.1-5.3. For the present two different studies have been conducted using simulations. First, expanding upon the experimental work that considered the effect of jet-to-jet temperature difference and velocity ratio, the simulation work will also consider the effects of velocity profile, namely contrasting that of a parabolic inlet profile with a tophat profile. Moreover expanding up on the experimental work the jet configuration will be adapted to include cold outer jets relative to a hot center jet, a configuration not possible with the existing experimental facility. Secondly, as new physics were investigated in Section 4.2 the ability of wall functions and different turbulent models to predict the center jet spreading is preliminarily examined. Shown in Table 11 is the simulation matrix including a note on whether or not wall functions were implemented. Note that flow rates match those in the experimental cases for similar velocity ratios, regardless of velocity profile. Since the data was acquired for a three dimensional domain, a Delaunay triangulation method was used to interpolate for values near the center plane of the parallel triple-jet. Care was taken not to extrapolate, as trends in the data can influence the extrapolation to provide unrealistic results, such as negative cell volumes.

Table 11 - Matrix of simulations ran

Case	Simulation Type	Velocity Profile	R	ΔT	Wall Functions
P1	RANS	Parabolic	$\frac{1}{2}$	$T_{inner} = 310K$ $T_{outer} = 325K$	No
P2	RANS	Parabolic	2	$T_{inner} = 310K$ $T_{outer} = 325K$	No
P3	RANS	Parabolic	$\frac{1}{2}$	$T_{inner} = 325K$ $T_{outer} = 310K$	No
P4	RANS	Parabolic	2	$T_{inner} = 325K$ $T_{outer} = 310K$	No
T1	RANS	Tophat	$\frac{1}{2}$	$T_{inner} = 292.5K$ $T_{outer} = 339.3K$	No
T2	RANS	Tophat	$\frac{1}{2}$	$T_{inner} = 292.5K$ $T_{outer} = 339.3K$	Yes
R1	RSM	Tophat	$\frac{1}{2}$	$T_{inner} = 292.5K$ $T_{outer} = 339.3K$	Yes

5.4.1 Parabolic Velocity vs Tophat Velocity Profile

In order to investigate the effects of velocity ratio on the numerical results comparisons of all cases with a parabolic inlet profile was made. For the given data, shown in Figure 53 there are two velocity ratios, $R = \frac{1}{2}$ and $R = 2$ with hot outer jets (P1 and P2) and cold outer jets (P3 and P4). It appears that close to the inlet, $x/D_{jet} < 3$ there is no significant effects of the jet configuration on the velocity field. This is in agreement with the experimental results which

suggested the temperature difference in the jets did not have an effect on the velocity field. When consider the velocity profile of the outer jet, it appears for cases P1 and P3 the outer jet is spreading slightly faster than in cases P2 and P4. As the momentum of the outer jets is four times larger than that of the inner jet it would seem the outer jet's momentum is dominating that of the inner jet.

For distances further downstream there appears to be deviation in the center jet velocity where the hot center jet in case P4 decays faster than the cold center jet in case P2. This seems unintuitive and is perhaps due to a convergence issue and should be further investigated. Similar analysis was given to the turbulent kinetic energy in each case as presented in Figure 55. As shown the kinetic energy profile at the edge of the center jet in case P4 does not agree well with those for case P2, further suggesting to the author a possible problem with convergence of one or both of the cases. When looking at the temperature profiles in Figure 54 it is noticed that the non-dimensional temperature does not appear to depend on the velocity ratio, except for far downstream distances in case P3 and P4. This is comparable in the experiments, where velocity ratio only effected the jets in terms of peripheral profiles where it could be thought of as a function of the bulk inlet temperature. As this is not seen in the simulations the boundary condition on the walls, $T = 300\text{K}$ may not be an adequate representation of the insulated box. Perhaps an insulated condition or a mixed boundary condition would better represent the physics peripheral to the jets.

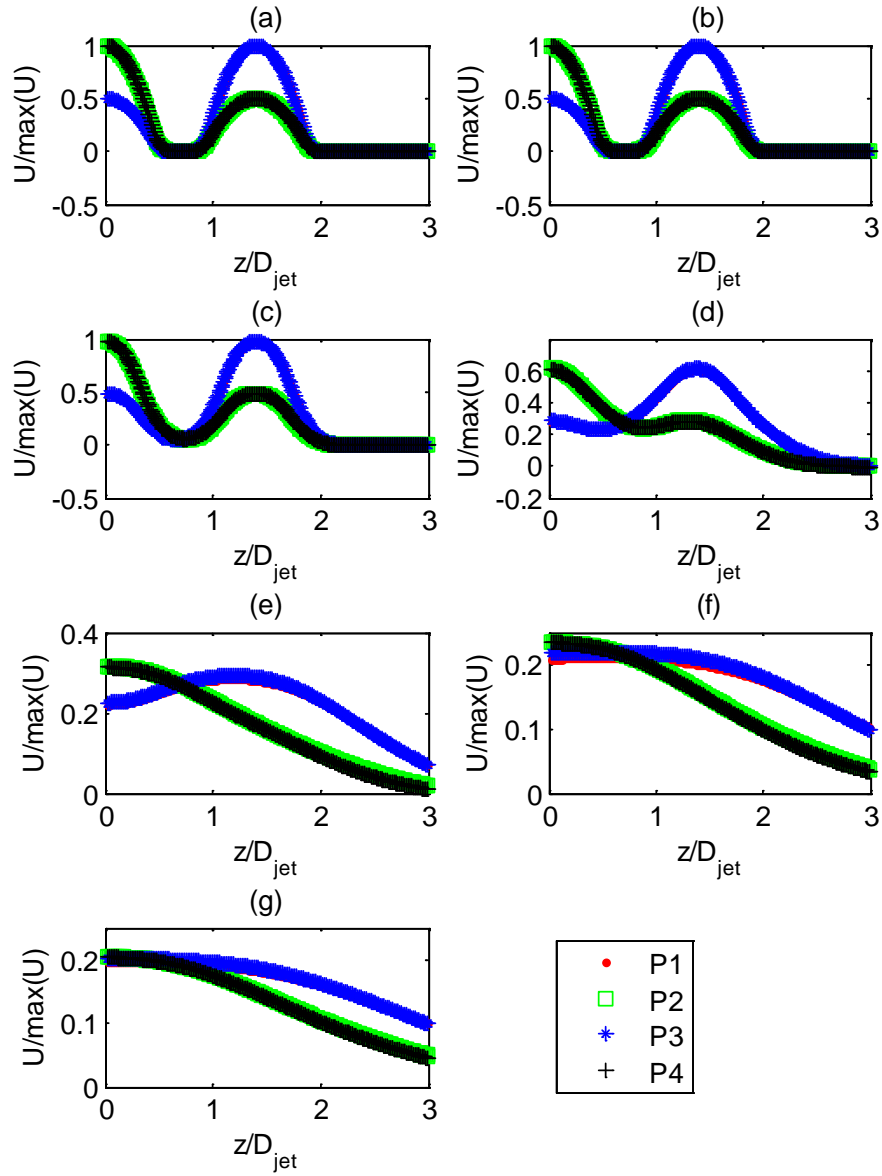


Figure 53 – Comparison of axial velocity profile in simulations with parabolic inlet profiles. (a) measured at $x/D_{jet} = 0.06$, (b) measured at $x/D_{jet} = 0.25$, (c) measured at $x/D_{jet} = 1$, (d) measured at $x/D_{jet} = 3$, (e) measured at $x/D_{jet} = 6$, (f) measured at $x/D_{jet} = 9$, and (g) measured at $x/D_{jet} = 18$

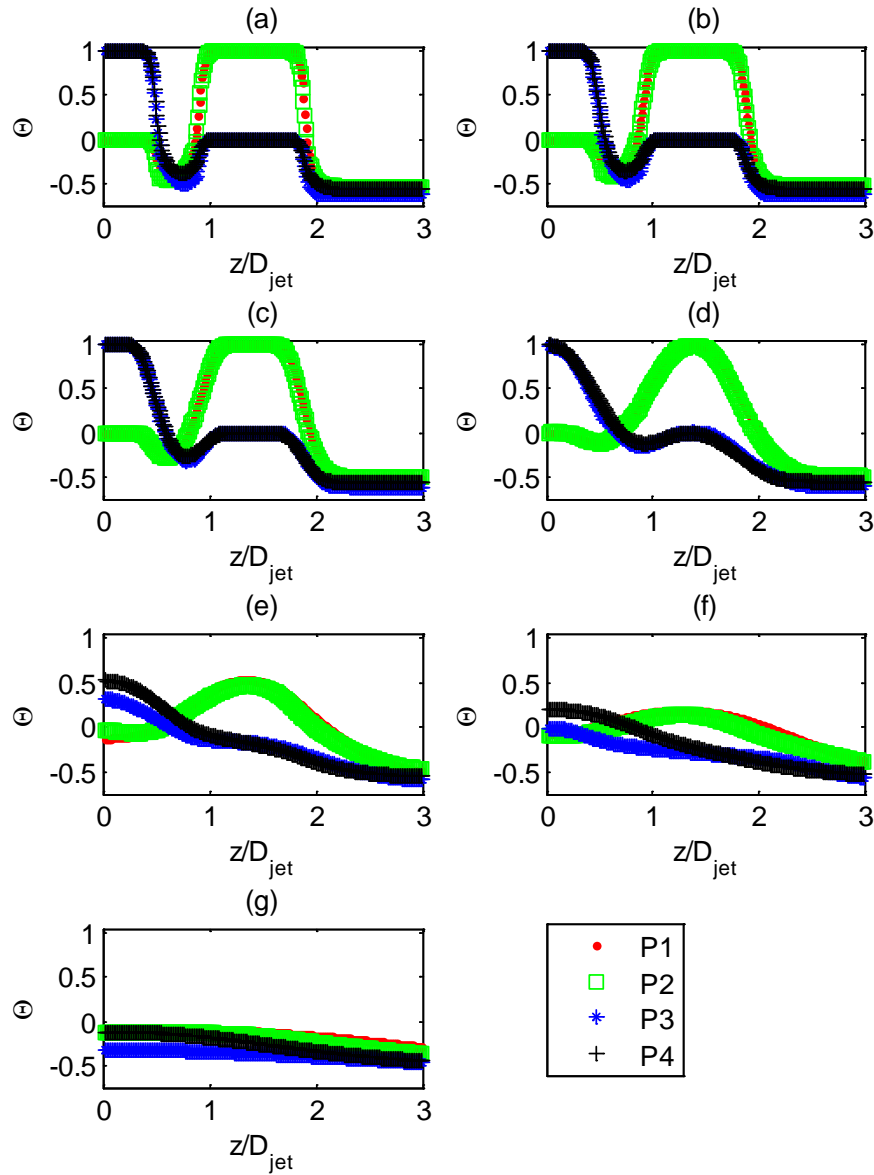


Figure 54 – Comparison of temperature profiles in simulations with parabolic inlet profiles. (a) measured at $x/D_{jet} = 0.06$, (b) measured at $x/D_{jet} = 0.25$, (c) measured at $x/D_{jet} = 1$, (d) measured at $x/D_{jet} = 3$, (e) measured at $x/D_{jet} = 6$, (f) measured at $x/D_{jet} = 9$, and (g) measured at $x/D_{jet} = 18$

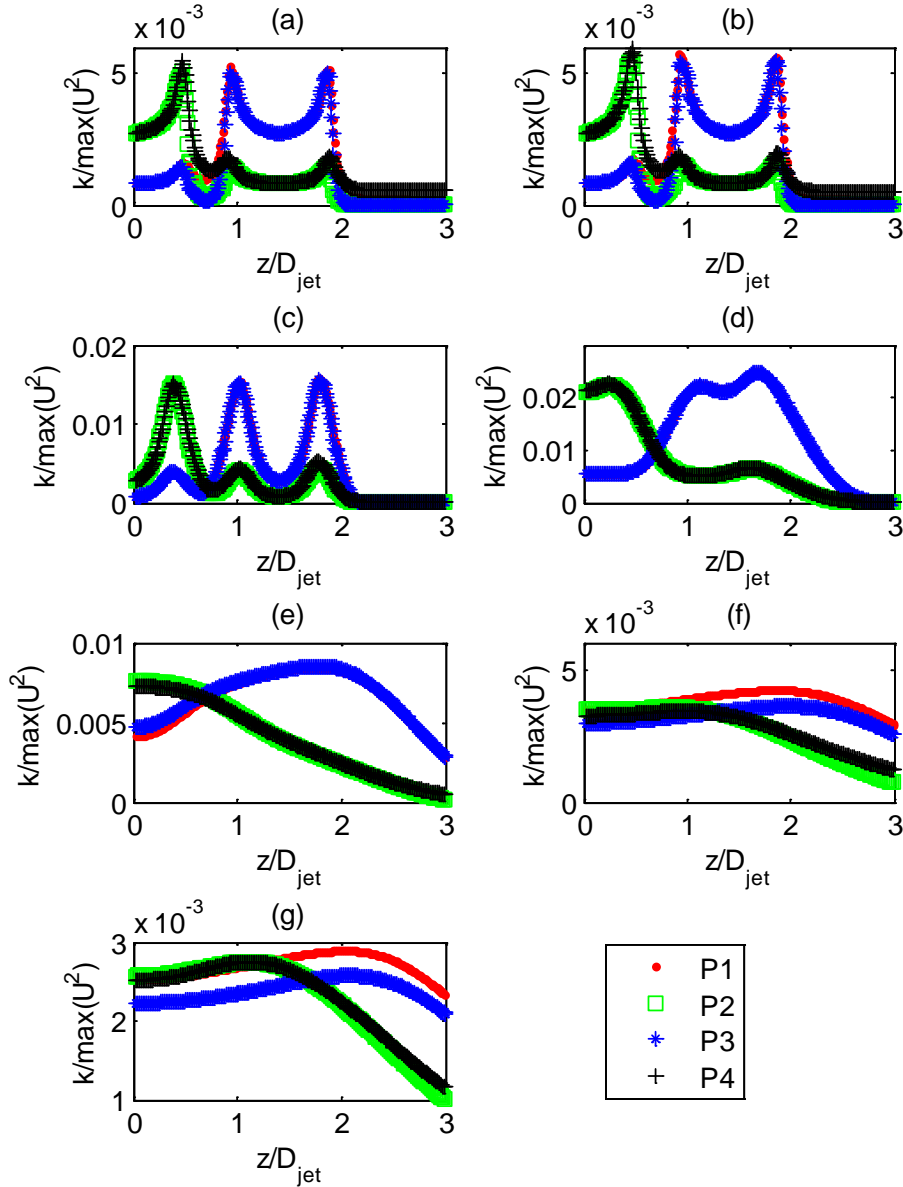


Figure 55 - Comparison of turbulent kinetic energy profiles in simulations with parabolic inlet profiles. (a) measured at $x/D_{jet} = 0.06$, (b) measured at $x/D_{jet} = 0.25$, (c) measured at $x/D_{jet} = 1$, (d) measured at $x/D_{jet} = 3$, (e) measured at $x/D_{jet} = 6$, (f) measured at $x/D_{jet} = 9$, and (g) measured at $x/D_{jet} = 18$

To better understand the effect of the velocity inlet profile comparisons were made between the parabolic inlet cases for two the $R = \frac{1}{2}$ velocity ratio with both jet configurations and the tophat inlet case for the same velocity ratio with the center cold jet configuration and the same case with wall function boundary conditions. As shown in Figure 56 the parabolic inlet

case jets centerline velocity decays much faster than those for the top hat profile. However, for the given results it is not possible to track the merge point of the jets as there did not exist a negative axial velocity component between the two jets. This may in fact be due to the close spacing suggesting that viscous effects dominate convective effects and provide some explanation into why the center jet velocity contours are much wider than expected.

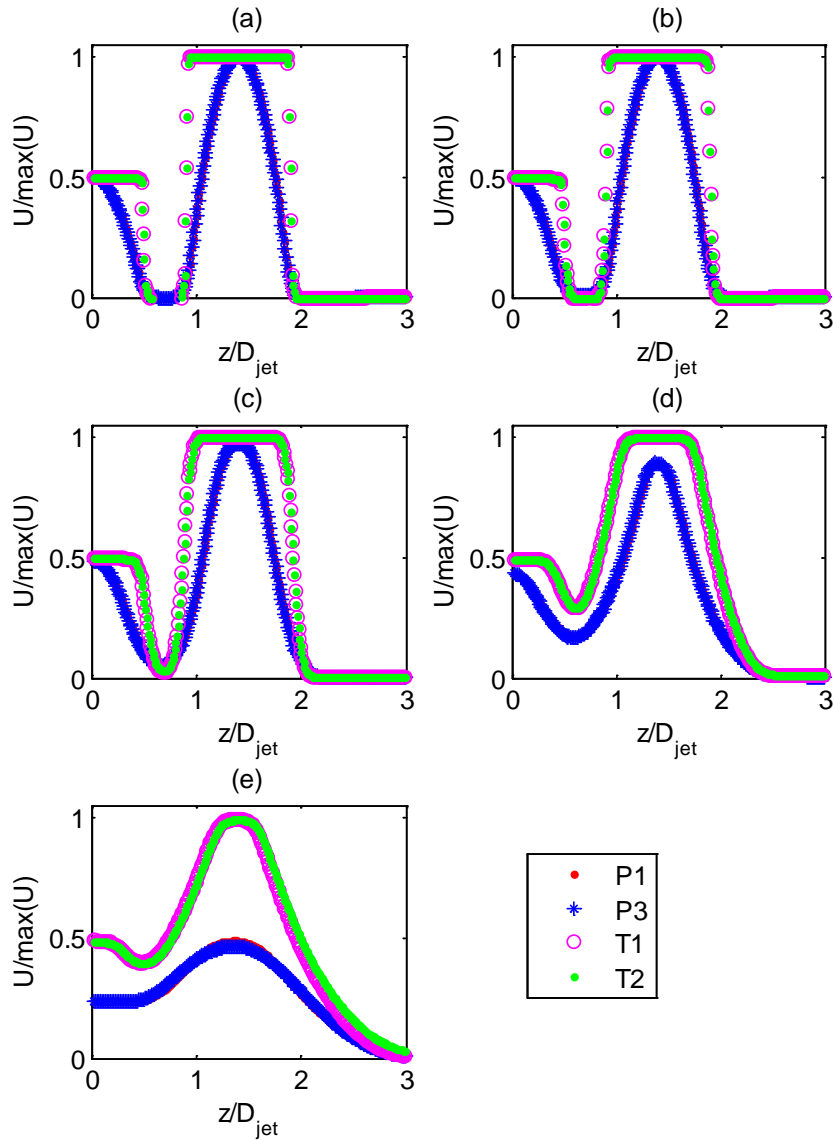


Figure 56 - Comparison of axial velocity profiles for tophat and parabolic inlet velocity profiles for both jet configurations. (a) measured at $x/D_{jet} = 0.06$, (b) measured at $x/D_{jet} = 0.25$, (c) measured at $x/D_{jet} = 1$, (d) measured at $x/D_{jet} = 3$, and (e) measured at $x/D_{jet} = 6$

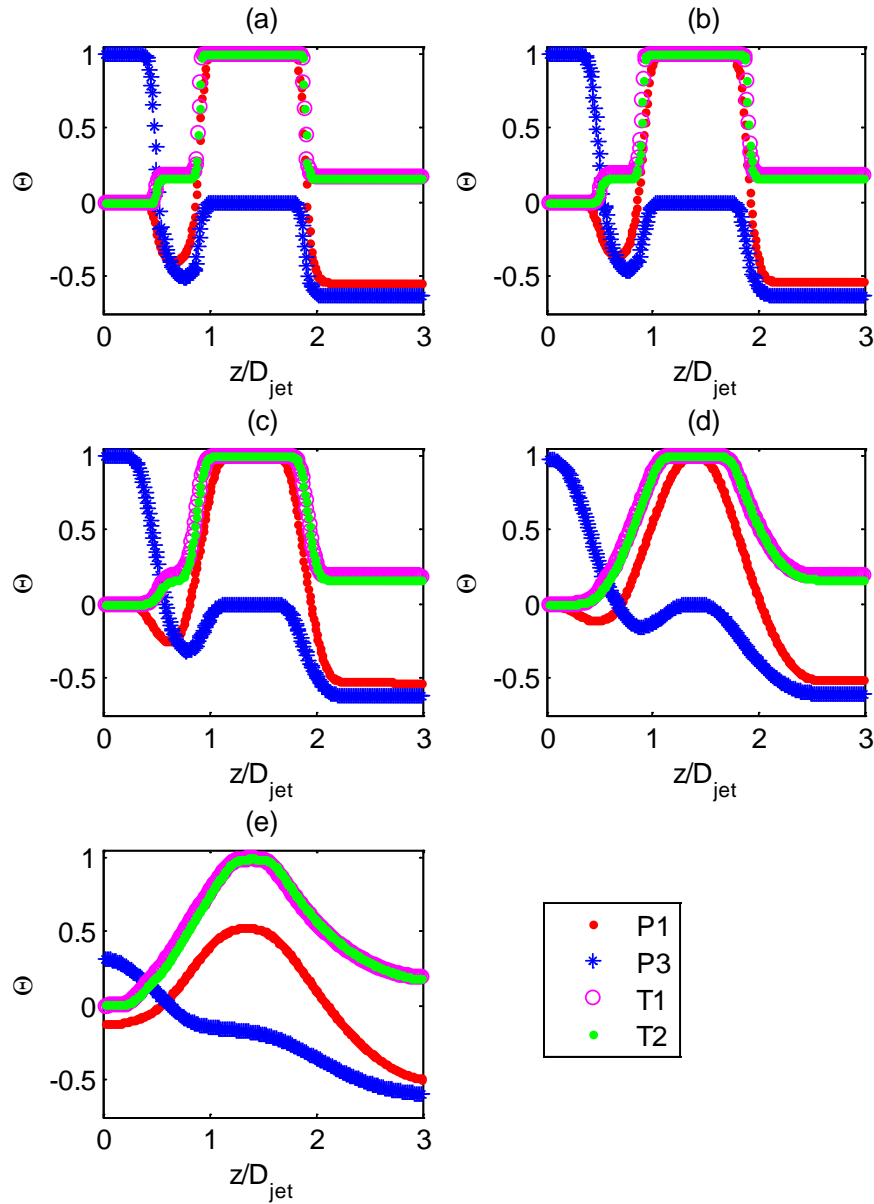


Figure 57 - Comparison of temperature profiles for tophat and parabolic inlet velocity profiles for both jet configurations. (a) measured at $x/D_{jet} = 0.06$, (b) measured at $x/D_{jet} = 0.25$, (c) measured at $x/D_{jet} = 1$, (d) measured at $x/D_{jet} = 3$, and (e) measured at $x/D_{jet} = 6$

5.4.2 Comparison of Turbulence Models

The qualitative analysis presented in Section 5.4.1 compare and contrasted the effect of different velocity profiles and jet configurations on the velocity, temperature, and turbulent kinetic energy

fields. However for the given models and cases tested the trends in inlet jet diameter found in the experiment were not observed. Several approaches to the modeling are first drawn into question including if grid convergence was in fact reached, is a steady simulations sufficient for computing this behavior, and can an isotropic turbulent model emulate the expected physical behavior. An in depth look at GCI presented in Section 5.3 addresses the first question. As for possibly quasi-steady state behavior, reinvestigation of the experimental data suggest not prevalent transients such as flapping or swirling. Perhaps then the isotropic RANS model cannot sufficiently model the turbulence present in the jets, an assumption that may be originally incorrect. In order to investigate the effects of assuming isotropic turbulence a simulation, case R1, was run utilizing a version of the Reynolds Stress Model derived by Launder [48]. This model is detailed in Section 5.2.3.

Shown in Figure 58 are velocity contours for $R = 1/2$ with hot outer jets utilizing a RANS model with a parabolic inlet condition (case P1), a RANS model with a tophat velocity profile (case T1), a RANS model with a tophat velocity profile and wall functions (case T2), and a RSM model with a tophat velocity profile and wall functions (case R1). As shown the RSM model did not differ significantly from the RANS model for the tophat case, both with and without the wall functions, appearing to be only slightly more dissipative both having a minutely faster decay rate and spreading rate. However, when investigating the turbulent kinetic energy in Figure 59 it is seen that the Reynolds stress model predicts higher kinetic energy than that for the $k-\epsilon$ realizable model near the inlet of the jets. When comparing the calculated turbulent kinetic energy values to that of the single jet the models both heavily under predict the magnitude. This could be due to errors associated with temporally dependent two-wire CTA results, which are known to be most sensitive to jet temperature at the edge of the jet where the largest turbulent

kinetic energy is expected. As such, the reader should be weary drawing conclusions on the accuracy of each model in the present work.

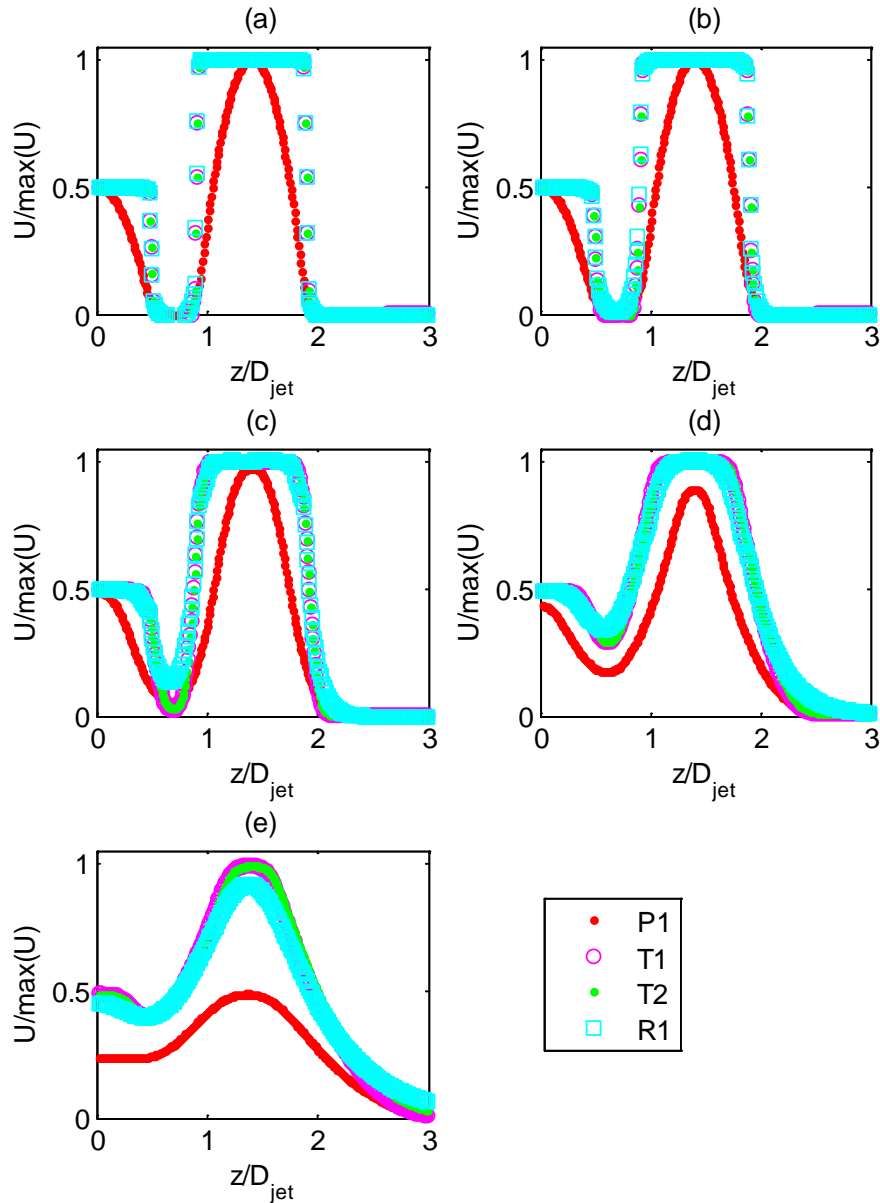


Figure 58 - Comparison of axial velocity profiles for different turbulence models. (a) measured at $x/D_{jet} = 0.06$, (b) measured at $x/D_{jet} = 0.25$, (c) measured at $x/D_{jet} = 1$, (d) measured at $x/D_{jet} = 3$, and (e) measured at $x/D_{jet} = 6$

When further investigating Figure 59 it is seen that by 1-3 diameters downstream the turbulent energy profiles agree for the different turbulence models, but by 6 diameters

downstream the turbulent kinetic energy expected in the outer jet by the RSM model has increased much faster than that predicted by the RANS models. However, by $x/D_{jet} = 18$ the turbulent kinetic energy predictions between the two models agree again, however this is not pictured here.

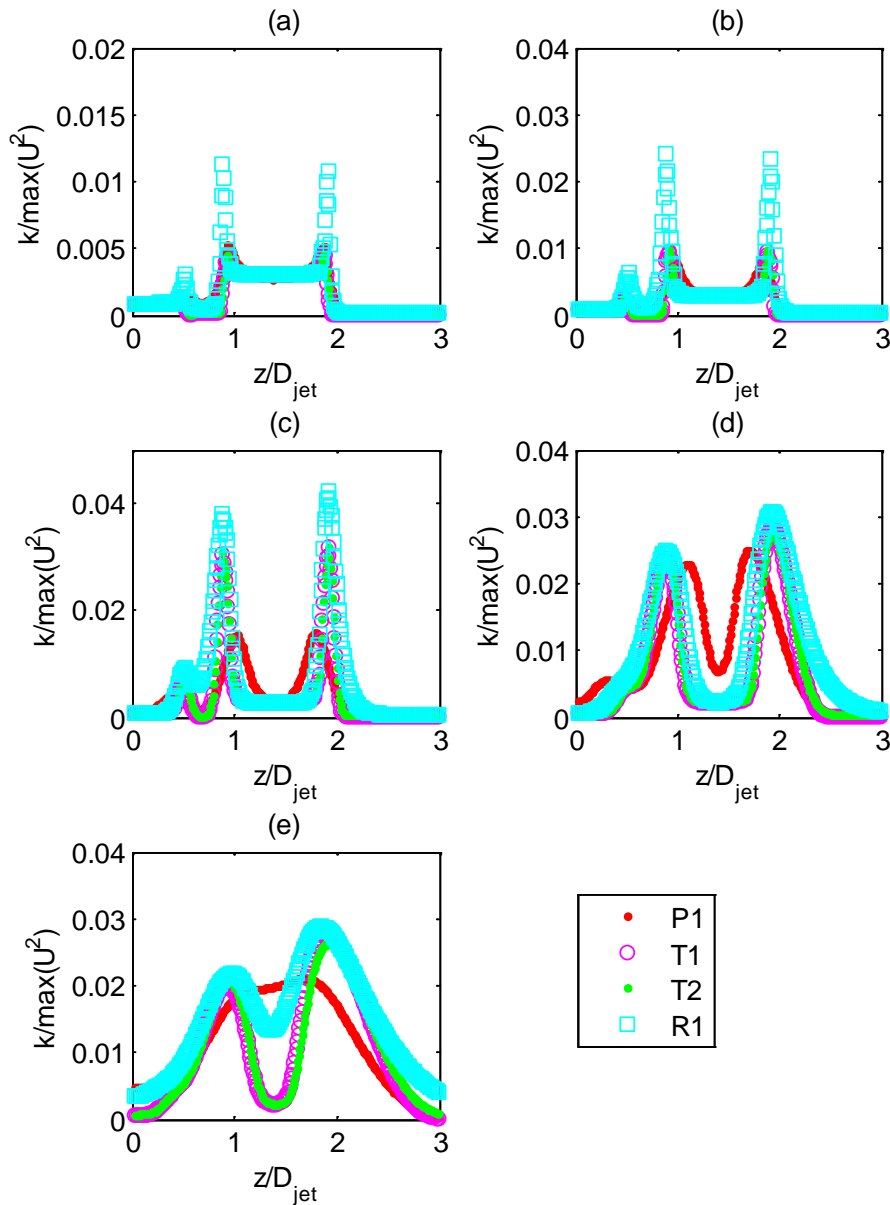


Figure 59 - Comparison of turbulent kinetic energy profiles for different turbulence models. (a) measured at $x/D_{jet} = 0.06$, (b) measured at $x/D_{jet} = 0.25$, (c) measured at $x/D_{jet} = 1$, (d) measured at $x/D_{jet} = 3$, and (e) measured at $x/D_{jet} = 6$

The present work with simulations has achieved two goals set forth for the study of a parallel round triple-jet. First, an extensive look into the available modeling methods in OpenFOAM® has been conducted with each's unique implementation studied. This is necessary for comparing results from OpenFOAM® with those from other commercial packages often used in validation studies. Secondly comparisons have been made between different velocity boundary conditions and temperature boundary conditions to see the effect of each on the behavior of the jet. These results have been qualitatively vetted with the experiments in terms of predicted trends. As discussed the realizable $k-\varepsilon$ turbulence model and the Launder Gibson Reynolds stress model were compared, however neither case predicted the spreading of the center jet. This suggests that first a more detailed investigation of the physics associated with the center jet is necessary. Additionally, a further look into the modeling of the triple jet is necessary. However, preliminary results have supported the idea that inlet conditions strongly effect the flow field in the triple jet.

6.0 FUTURE WORK

Thermal striping is considered a concern for next generation nuclear reactors such as the VHTR. However much of the available work in the literature has focused on either parallel, triple slot jets or stratified flows in a pipe mixing tee. While both are possible ways to study turbulent mixing phenomena neither is a straight forward representation of the VHTR lower plenum. As such neither is strongly applicable for validation and verification of computational modeling efforts. As such two unique efforts were presented to begin address thermal striping concerns, and the need for validation and verification, in the lower plenum. First, the present work included both experimental and computational efforts, focusing on contributions related to turbulent jet mixing, specifically in the parallel, round- triple-jet. Secondly, scaling analysis were conducted for the VHTR lower plenum and utilized in the design of a complex experimental facility capable of creating an impinging jet array issuing axially into a tube bundle in crossflow.

For experiments, the facility was designed and built, as detailed in Section 2.0. The first set of experiments focused on a parallel round non-isothermal triple-jet, centered in the 0.76 m x 0.76 m experimental cross section pictured in Figure 6. Velocity measurements were made using the two wire probe which consisted of constant temperature anemometer for measuring velocity and a constant current anemometer for applying temperature correction. Tests were run while varying the velocities and jet spacing within a matrix of different conditions. By studying a range of velocity ratios, qualitative and quantitative information about prominent hydraulic structures

within the flow were collected and studied to determine potential mechanisms that dominant the mixing process. Importantly, an unexpected and never before documented spreading behavior in the triple-jet array was identified. Significant effort was taken to assert that the witnessed behavior was not an artifact of the measurements and is in fact a newly observed physics.

While the current measurements do not provide high fidelity spatial or temporal resolution they have been thoroughly vetted as a new physics. This allows for a new interpretation of simulations results. Preliminary analysis has shown that isotropic RANS models are not expected to accurately predict this flow in the small region between tightly spaced jets. Additional to mean velocity magnitude data, it is necessary to determine trends in the components of the velocity field and temperature.

New information about hydraulic and thermal trends in the flow field was used for creating meshes of the domain for numerical studies, as well as for assessing the accuracy with which the average fields can be predicted utilizing Reynolds averaging, in both the isothermal and non-isothermal configurations. Careful consideration was given to simulate experimental case. Additionally the numerical models were used to study parameters which could not be controlled such as the inlet velocity profile and the configuration of the jet temperatures.

Finally, in order to begin the transition from thermal mixing in a parallel triple-jet to conditions more applicable in the VHTR lower plenum, scaling analysis of thermal mixing in the lower plenum were conducted. For future work, the unit cell facility described in section 2.2 will be used with PIV, thermocouple, and anemometry measurements. These detailed experiments will provide data needed for validation of future numerical investigations in the complex unit cell model [56].

Through the combined efforts of the experimental and computational studies of isothermal, and non-isothermal, triple-jet flow, new understanding into the physics involved will be gained, as well as development of predictive tools for future thermal striping studies. With increased understanding of the effects of geometry, velocity ratio, and temperature difference on magnitude and frequency of temperature fluctuations in the domain, future experiments will be able to better account for possible thermal striping in the facility to improve accuracy of desired measurements. Future experiments investigating the unit cell will also provide enhanced understanding of thermal striping in the VHTR lower plenum, and ultimately aid in predicting operational parameters that best improve safety and lifetime of components.

APPENDIX A

ANALYSIS OF SYMMETRY IN THE EXPERIMENTAL DOMAIN

A.1 VELOCITY CONTOURS AND TURBULENCE QUANTIFICATION

Before studying the behavior of a parallel triple-jet, attributes of the free jet scenario are of interest. Extreme care is taken to ensure the jet enters completely normal to the test section, but in reality there could potentially be some misalignment between the jet and the linear stages upon which the CTA is mounted. During early phases of design and fabrication validation work is conducted to check this alignment. Velocity data in the y - z plane are captured from three different planes: $x/D_{jet} = 0.33$ (jet nozzle), 3, and 8. For these tests, $Re_{jet} = 19.8 \times 10^3$. Contours for the velocity, turbulent kinetic energy, and percent turbulent intensity are shown in Figure 60(a), (b), and (c), respectively. The black circle represents the outline of the jet nozzle. The jet is approximately parabolic, with the majority of the velocity decay occurring near the nozzle walls. For the turbulent kinetic energy (Figure 60 (b)) and percent turbulence intensity (Figure 60 (c)), the respective quantities are computed from the velocity data according to Equation (18) and (19). For future studies where the experimental data will be used to validate numerical modeling efforts, it is ideal to have a symmetric, easy to quantify profile. The setup, in its current configuration, meets these requirements as described later.

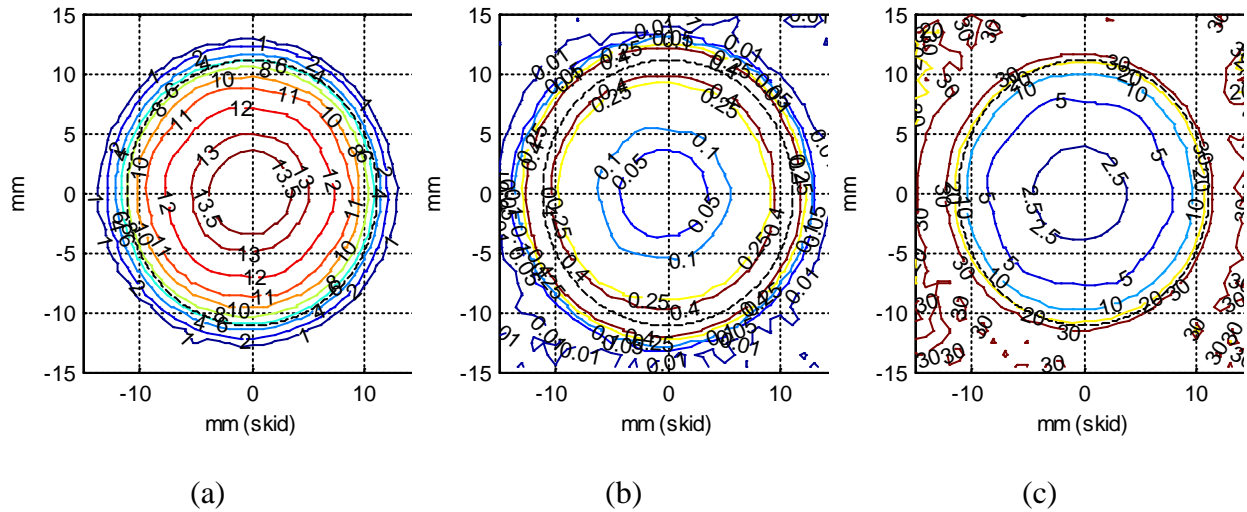


Figure 60 - Contours at $x/D_{jet} = 0.333$: (a) velocity (m/s), (b) turbulent kinetic energy (m^2/s^2), and (c) percent turbulence intensity. For each contour, the circular jet geometry is included for reference (solid black line, $D_{jet} = 0.875$ in (22.2 mm)). $Re_{jet} = 19.8 \times 10^3$

Similar data is captured for the two remaining y - z planes ($x/D_{jet} = 3$ and 8). The velocity, kinetic energy, and percent turbulence intensity contours are shown in Figure 61 and Figure 62 for $x/D_{jet} = 3$ and 8, respectively. Notice that the asymmetries seen for the $x/D_{jet} = 0$ plane seem to have increased at the $x/D_{jet} = 8$ plane. They then seem to become smaller for the final plane of data ($x/D_{jet} = 8$).

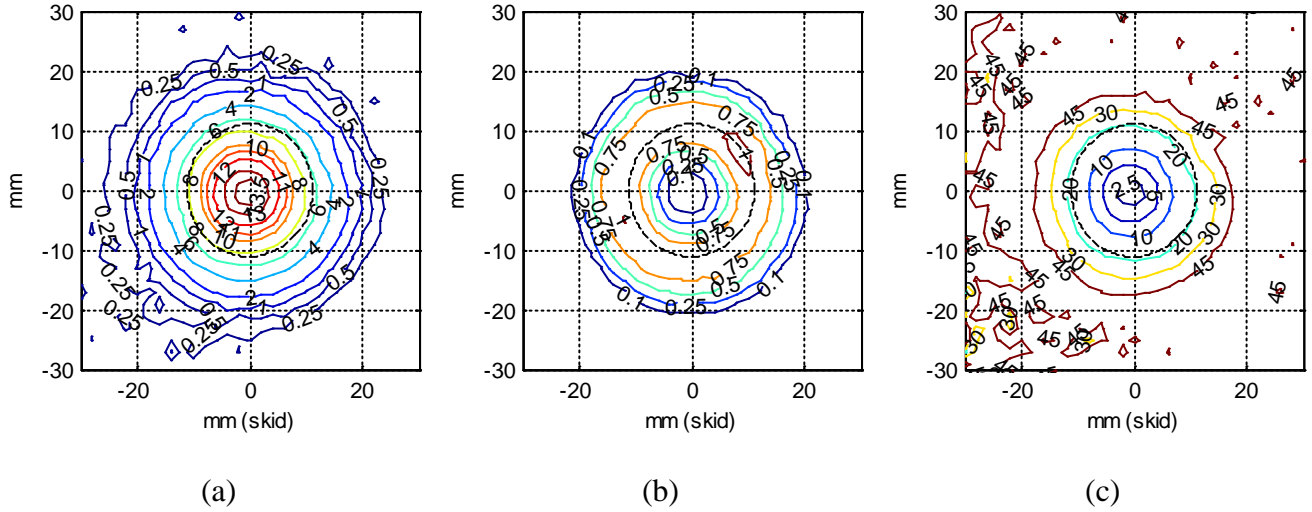


Figure 61 - Contours at $x/D_{jet} = 3$: (a) velocity (m/s), (b) turbulent kinetic energy (m^2/s^2), and (c) percent turbulence intensity. For each contour, the circular jet geometry is included for reference (solid black line, $D_{jet} = 0.875$ in (22.2 mm)). $Re_{jet} = 19.8 \times 10^3$.

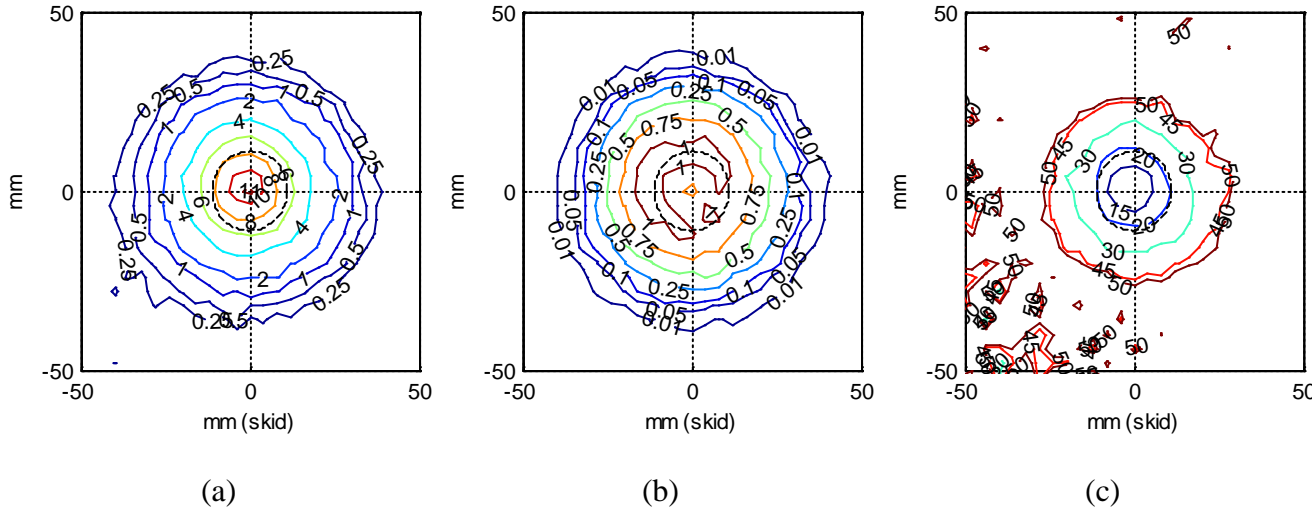


Figure 62 - Contours at $x/D_{jet} = 8$: (a) velocity (m/s), (b) turbulent kinetic energy (m^2/s^2), and (c) percent turbulence intensity. For each contour, the circular jet geometry is included for reference (solid black line, $D_{jet} = 0.875$ in (22.2 mm)). $Re_{jet} = 19.8 \times 10^3$.

A.2 QUANTIFICATION OF JET PROFILE

It is important to be able to gauge and quantify the asymmetries in a manner other than a visual estimate, as well as to find an appropriate, axisymmetric curve fit. Here, we choose to analyze velocity data traces from six distinct lines in the contours: negative y -axis, positive y -axis, negative z -axis, positive z -axis, quadrant one (positive z , positive y) diagonal cut, and quadrant 3 (negative z , negative y) diagonal cut. This creates six unique lines, representative of three lines “folded” onto themselves, that is, plotting the absolute value of the radial coordinate (U/U_0 vs. $|r/D_{jet}|$). For each x/D_{jet} plane, the velocity profiles along these six lines are compared. If the jet were perfectly symmetric, these six lines would lie exactly on top on each other. This data is shown for $x/D_{jet} = 0.33$ plane in Figure 63 where the velocities have been normalized by the centerline value (U_0). In order to better understand the asymmetry of the data set, a curve fit was applied to the data set containing all six lines, as shown in Figure 63. It was found that to a high degree, the data is accurately represented by a parabola. Fitting a parabola from $0 < x/D_{jet} < 0.45$ (90% of the jet diameter), the mean error was 0.53% with a maximum curve fit error of 2.18%, occurring at the outer most points. The parabolic nature of the flow suggests that, at the inlet to the test section, the flow has not become fully developed in the distance between the exit of the honeycomb flow straightener and nozzle. The same routine of “folding” was repeated for $x/D_{jet} = 8$ and $x/D_{jet} = 16$. A similar curve fitting procedure was conducted as a means of measuring the asymmetry at downstream locations. It is noted that up until $x/D_{jet} = 8$, the error in the mean and max curve fit grows, while for $x/D_{jet} = 16$ the mean and max uncertainty are both less than at $x/D_{jet} = 0.33$. This suggests perhaps some asymmetry is decaying further downstream. The source of increasing asymmetry at closer axial locations may be related

to the presence of the measurement equipment. However, these results show that the facility produces a jet with predictable and acceptable flow properties.

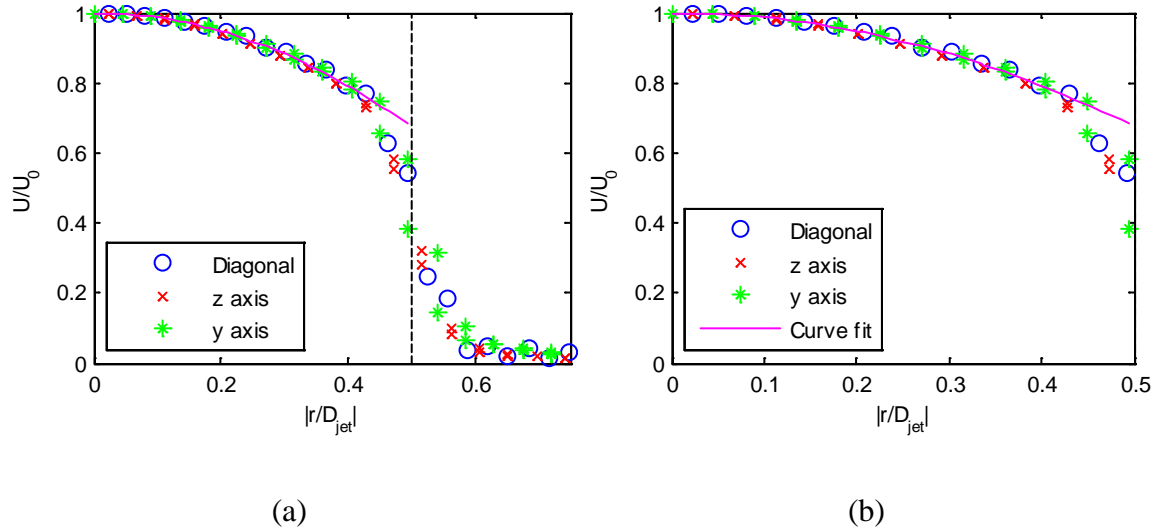


Figure 63 – Measured at $x/D_{jet}=0.33$ (a) normalized velocity contours “folded” on each other, and (b) curve fit over 0.85% of data included

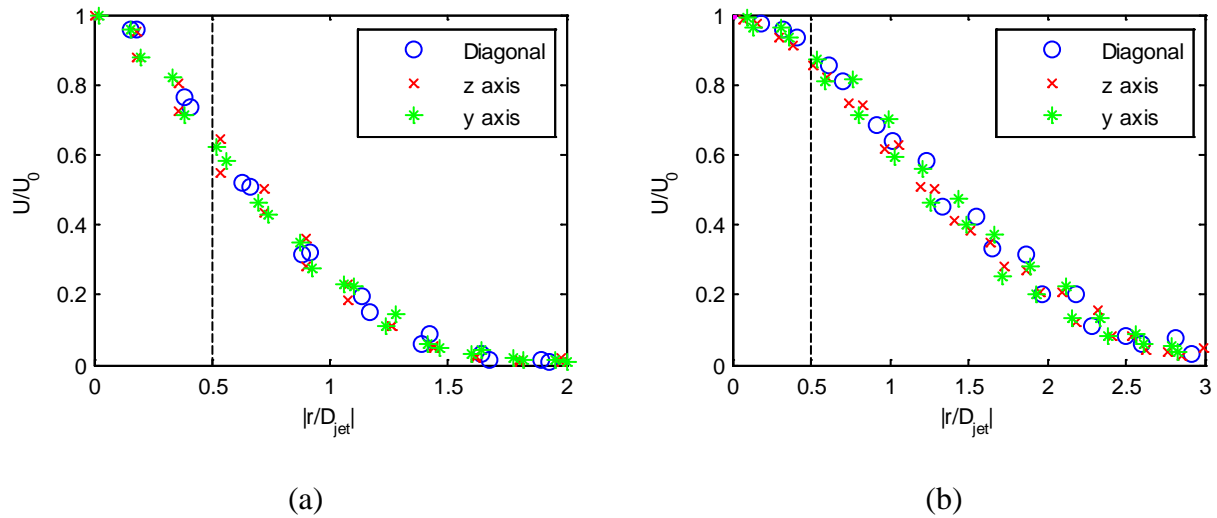


Figure 64 - Normalized velocity contours “folded” on each other. (a) measured at $x/D_{jet}=8$, and (b) measured at $x/D_{jet}=16$

APPENDIX B

OVERVIEW OF THREE-WIRE CTA PRINCIPLES AND DATA MANIPULATION

For future work it is necessary to resolve not just the magnitude of velocity by also the individual components. As such, three-wire anemometry is necessary. The 55P91 probe (from Dantec Dynamics), shown in Figure 65, consists of three orthogonal, 5 μm diameter gold plated wires. For a complete review of anemometry, including three-wire transformation, the reader is directed to the seminal review by Bruun [57]. Following is a brief description of measurement nuances associated with three-wire anemometry, including applicable ranges for utilizing the probe in experiments.

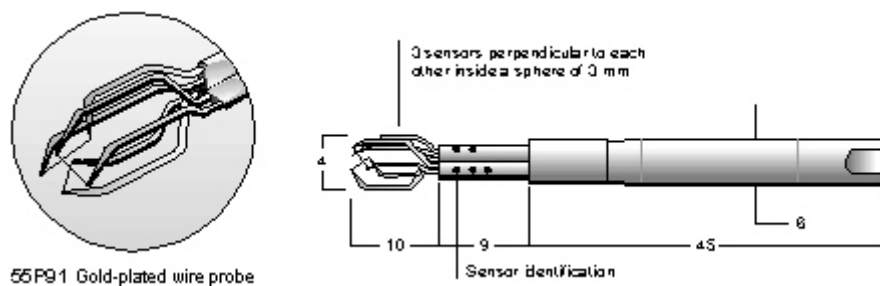


Figure 65 – Dantec Dynamics 55P91 three wire anemometer

When using a three wire probe it has been shown that the normal velocity to each wire is not the best representation of the effective cooling velocity. It has been shown that a better assumption for the effective velocity “felt” by each wire is that expressed in Jorgensen’s

equation (Equation (73)), where the subscript e denotes the effective cooling velocity (i.e., the velocity “felt” by the wire), and n , t , and b are the normal, tangential, and binormal components of the flow relative to a given wire. For a system of three orthogonal wires, it is then easy to simultaneously solve the equations for effective velocity in each wire in order to find the velocity vector incidental on the probe [57].

$$U_e^2 = U_n^2 + k^2 U_t^2 + h^2 U_b^2 \quad (73)$$

However, while a three-wire anemometer allows one to measure three simultaneous, orthogonal components of velocity, there exists a uniqueness problem originating from Jorgensen’s Equation, Equation (73). Since the effective velocity is related to the square of each component, it is not possible to discern if each component is positive or negative. This results in each unique measurement coming from one of 8 possible velocity vectors. This concept has been rigorously studied by Dobbeling [58], Lekakis [59], and Vukoslavcevic [60]. The minimum polar angle, measured from the axis of the probe stem, for which a unique solution is guaranteed, is commonly called the uniqueness domain. For the Dantec 55P91, the uniqueness domain, also referred to as the approach octant, is 35.264° [59]. This greatly restricts the angle at which anemometers can be oriented relative the dominant direction of the flow. Another problem with constant temperature anemometry is caused by temperature fluctuations in the flow. Since a constant temperature anemometer works by maintaining the wire temperature and measuring power lost to cooling, it is necessary that the calibration and the flow be at the same temperature. Some sources [61] suggest that even small changes in the fluid temperature ($\sim 1^\circ\text{C}$) might have significant changes ($\sim 2\%$) on the velocity measured. However, it is possible if the flow is non-isothermal to correct the voltage measurements if temperature in the fluid is recorded simultaneously with wire voltage, by applying Equation (74) to the gathered wire voltages,

where T_w is the sensor temperature, T_0 is the calibration temperature, T_a is the ambient temperature measured in the fluid, and E_a is the acquired voltage. This method is only recommended when the fluctuation temperature varies $\sim 10^\circ\text{C}$ from the calibration temperature [61]. For larger temperature variations a temperature dependent calibration, such as that done in Section 3.1.1 is required.

$$E_{corr} = \left(\frac{T_w - T_0}{T_w - T_a} \right)^{0.5} E_a \quad (74)$$

The last limitations with hot-wire anemometers involve physical constraints on their use. First, due to the physical size of the wires, often 1-3 mm in length, the probes do not provide true point measurements, but rather spatial averages over very small spaces. For the Dantec 55P91, the spatial resolution is listed as 1.3 mm [61]. Additionally, as touched on by both Brunn [57] and Jorgensen [61], for high turbulent intensity flows ($I > \sim 15\%$), the error associated with hot wire measurements can become large, due to effects associated with prong interference and the time response of the anemometry system.

For future work on parallel triple-jets two different anemometry probes have been purchased. For isothermal flows, a triple-wire anemometer (Dantec 55P91) will be used to map the three dimensional mean and fluctuation velocity field, as well as the Reynolds stresses, which can be calculated real time. Note that, as shown by Benedict [62], calculating the uncertainty in Reynolds stress measurements is not always straightforward, but should be implemented real time when gathering data, as it depends on third and fourth-order moments. For non-isothermal flows, a custom probe was built by Dantec Dynamics (14793S01), which contains three orthogonal $5\mu\text{m}$ diameter gold plated wires operated in constant temperature mode (CTA) to measure velocity, and a $1\mu\text{m}$ diameter platinum wire operated in constant current mode (CCA) to

measure the temperature fluctuations in the velocity field. The CCA wire is capable of sampling temperature fluctuations at up to 2 kHz. All four wires are contained in a small package, tighter than that of the 55P91.

APPENDIX C

OVERVIEW OF DETACHED EDDY AND LARGE EDDY SIMULATIONS IN OPENFOAM®

As part of the work present time was spent investigating the implementation of the Spalart-Allmaras Improved Delayed Detached Eddy Simulation (IDDES) Model in OpenFOAM® and the Dynamic Local Homogenous Smagorinsky Large Eddy Simulation Model in OpenFOAM®. Both model offer significantly more information than standard RANS approaches to turbulence but require significantly more computation time and a much greater sensitivity to the peculiarities of the simulation, such as mesh design, boundary conditions, and discretization schemes.

C.1 IMPROVED DELAYED DETACHED EDDIE SIMULATION (IDDES)

In OpenFOAM® the Spalart-Allmaras turbulent viscosity transport model is implemented with a few documented modifications, as shown in Equation (75) and (76) [63]. Note that in all subsequent equations $\chi = \frac{\tilde{\nu}}{\nu}$. The first modification to the standard SA model is the exclusion of

f_{i2} terms included in Spalart-Allmaras. A discussion of this exclusions is given in [64]. Additionally, an unpublished term, f_{v3} , and a new version of the f_{v2} term were developed by Spalart and Allmaras during early implementations of the model. These modifications are included in the OpenFOAM code. For a discussion of the new terms and their effects on the flow see [65]. In Equation (76) $C_{b1} = 0.1355$, $C_{b2} = 0.622$, $C_{w2} = 0.3$, $C_{w3} = 2$, $C_{v1} = 7.1$, $C_{v2} = 5$ $\sigma = 2/3$, $\kappa = 0.41$, and C_{w1} is given by Equation (83).

$$\nu_t = \tilde{\nu} f_{v1} \quad (75)$$

$$\frac{\partial \tilde{\nu}}{\partial t} + \langle u_j \rangle \frac{\partial \tilde{\nu}}{\partial x_j} = C_{b1} \tilde{S} \tilde{\nu} + \frac{1}{\sigma_{\nu_t}} \left\{ \nabla \cdot [(\nu + \tilde{\nu}) \nabla \tilde{\nu}] + C_{b2} |\nabla \tilde{\nu}|^2 \right\} - C_{w1} f_w \left(\frac{\tilde{\nu}}{d} \right)^2 \quad (76)$$

$$f_{v1} = \frac{\chi^3}{\chi^3 + C_{v1}^3} \quad (77)$$

$$\tilde{S} = f_{v3} \sqrt{2\Omega_{ij}\Omega_{ij}} + \frac{\tilde{\nu}}{(\kappa d)^2} f_{v2} = \sqrt{\frac{1}{2} \left(\frac{\partial u_i}{\partial x_j} - \frac{\partial u_j}{\partial x_i} \right)^2} + \frac{\tilde{\nu}}{(\kappa d)^2} f_{v2} \quad (78)$$

$$f_{v3} = \frac{(1 + \chi f_{v1})(1 - f_{v2})}{\chi} \quad (79)$$

$$f_{v2} \approx \frac{1}{\left(1 + \frac{\chi}{C_{v2}}\right)^3} \quad (80)$$

$$f_w = g \left[\frac{1 + C_{w3}^6}{g^6 + C_{w3}^6} \right]^{1/6} \quad (81)$$

$$r = \frac{\tilde{\nu}}{\tilde{S}(\kappa d)^2} \quad (82)$$

$$C_{w1} = \frac{C_{b1}}{\kappa^2} + \frac{1 + C_{b2}}{\sigma} \quad (83)$$

In the standard Spalart-Allmaras turbulence model, the length scale d is normally assumed to be the normal distance from the nearest wall. The length scale d is modified for use in the IDDES model based on multiple mesh dimensions. The hybrid length scale, d_{IDDES} , is shown in Equation (84). The IDDES length scale is equal to the large eddy simulation (LES) length scale d_{LES} when the modified blending function \tilde{f}_d , which itself depends on the blending function f_b is equal to zero. Similarly in the RANS region where \tilde{f}_d is 1 and the solution only depends on the RANS length scale, d_w , the function f_e can be thought of as a correction to the length scale in order to prevent a mismatch of the log-law velocity profile at the interface of the RANS and LES regions of the solution. Note in Equation (84) and subsequently defined terms $C_{DES} = 0.65$, $c_w = 0.15$, $h_{\max} = \max[\Delta x, \Delta y, \Delta z]$, Δ_{wn} is the mesh size in the direction normal to the nearest wall, $C_t = 3.55$, $C_l = 1.63$, and $f_w^* = 0.422$. All other coefficients are the same as those defined for the standard Spalart-Allmaras model.

$$d_{IDDES} = \tilde{f}_d (1 - f_e) d_{RANS} + (1 - \tilde{f}_d) d_{LES} \quad (84)$$

$$d_{LES} = C_{DES} \psi \min \left[\max \{ c_w d_w, c_w h_{\max}, \Delta_{wn} \}, h_{\max} \right] \quad (85)$$

$$d_{RANS} = d_w \quad (86)$$

$$\tilde{f}_d = \max \left[\left\{ -\tanh \left[\left(8r_{d,v+v_t} \right)^3 \right] \right\}, f_b \right] \quad (87)$$

$$r_{d,v} = \frac{\nu}{\max \left[\frac{1}{2} \sqrt{\left(\frac{\partial u_i}{\partial x_j} + \frac{\partial u_j}{\partial x_i} \right)^2}, 10^{-10} \right] (\kappa d_w)^2} \quad (88)$$

$$f_b = \min \left[2e^{-9\alpha^2}, 1 \right] \quad (89)$$

$$\alpha = \max \left[0.25 - \frac{d_w}{h_{\max}}, -5 \right] \quad (90)$$

$$f_e = \max [f_{e1} - 1, 0] \psi f_{e2} \quad (91)$$

$$f_{e1} = \begin{cases} 2e^{-11.09\alpha^2} \frac{h_{\max}}{d_w} & \text{if } \alpha > 0 \\ 2e^{-9\alpha^2} \frac{h_{\max}}{d_w} & \text{if } \alpha < 0 \end{cases} \quad (92)$$

$$f_{e2} = 1 - \max \left[\tanh \left[\left(c_t^3 r_{d,v_t} \right)^3 \right], \tanh \left[\left(c_l^3 r_{d,v} \right)^{10} \right] \right] \quad (93)$$

$$\psi = \left\{ \min \left[100, \frac{1 - \frac{C_{b1}}{C_{w1} \kappa f_w^*} f_{v2}}{\max [10^{-10}, f_{v1}]} \right] \right\} \quad (94)$$

Example boundary conditions for the Spallart-Almaras IDDES model are shown in Table 12. These boundary conditions are identical to those for the RANS model, except for the calculation of v_t at the wall. This should be expected as the Spallart-Almaras is a hybrid RANS-LES model.

Table 12 - IDDES Boundary Conditions

	$U(r)$	P	k	v_t
Inlets	$U_{cold} = 7.72m/s$ $U_{hot} = 15.61m/s$	$\frac{\partial P}{\partial x_n} = 0$	$k = \frac{3}{2}(UI)^2$	$\frac{\partial v_t}{\partial x_n} = 0$
Walls	$\mathbf{U} = 0$	$\frac{\partial P}{\partial x_n} = 0$	$k = 0$	Spalding's Law of the Wall (Section C.3)
Outlet	$\frac{\partial U_n}{\partial x_n} = 0$	$\frac{\partial P}{\partial x_n} = 0$	$k = 0$	$\frac{\partial v_t}{\partial x_n} = 0$

C.2 LARGE EDDY SIMULATION (LES)

An alternative to Reynolds averaged approaches is large eddy simulation (LES). In LES models large size scale structures are resolved, or solved for, while the smaller structures are modelled. While several different LES models are packaged in the official OpenFOAM distribution a different implementation of the Dynamic Smagorinsky turbulence model was utilized based on experience and results with simulations of heated and non-heated jets [66]. By defining a filter operation such that $\phi = \bar{\phi} + \phi''$, where an over-bar $\bar{\phi}$ denotes a unfiltered quantity while ϕ'' is the subgrid scale quantity removed by the filter. Applying this filtering technique to the Navier-Stokes equations the governing Equations for incompressible LES can be derived according to those shown in Equations (95) and (96). As with RANS models, there is a closure problem resulting the subgrid scale interactions in $u_i''u_j''$, thus one approach is to use an eddy viscosity model as done with RANS [47]. The typical eddy viscosity model is shown in Equation (97).

$$\frac{\partial \bar{u}_j}{\partial x_j} = 0 \quad (95)$$

$$\frac{\partial \bar{u}_i}{\partial t} + \bar{u}_j \frac{\partial \bar{u}_i}{\partial x_j} = \frac{-1}{\rho} \frac{\partial \bar{p}}{\partial x_i} + \frac{\partial}{\partial x_j} \left[\mu \left(\frac{\partial \bar{u}_i}{\partial x_j} + \frac{\partial \bar{u}_j}{\partial x_i} \right) - u_i''u_j'' \right] \quad (96)$$

$$u_i''u_j'' = \nu_{SGS} \left(\frac{\partial \bar{u}_i}{\partial x_j} + \frac{\partial \bar{u}_j}{\partial x_i} \right) \quad (97)$$

For the current work, the turbulent viscosity was calculated using a dynamic version of the Smagorinsky model [67] derived by Germano [68]. Given that D is the deviatoric component of the symmetric portion of the velocity gradient, shown in Equation (98), the locally averaged version is shown in Equations (99)-(102). When implementing and using LES simulations there

are a large number of careful considerations that the user should take to ensure accurate and applicable results. For the present work a top hat filter was used while the grid dependent delta (δ) was the cubic root of the volume of each cell. However, for the present work these are not elaborated on in detail. For additional information and understanding one should see references [47, 69, 70, 71]. The LES boundary conditions are the same as those shown in Table 12.

$$D = \frac{1}{2} [\nabla \mathbf{U} + (\nabla \mathbf{U})^T] - \frac{1}{3} \text{trace} \left(\frac{1}{2} [\nabla \mathbf{U} + (\nabla \mathbf{U})^T] \right) \quad (98)$$

$$\nu_{SGS} = cD \cdot \delta^2 \|D\|^2 \quad (99)$$

$$cD = \frac{\langle L \cdot M \rangle}{\langle M \cdot M \rangle} \quad (100)$$

$$L = (\overline{\mathbf{U}\mathbf{U}} - \overline{\mathbf{U}}^2) - \frac{1}{3} \text{trace}(\overline{\mathbf{U}\mathbf{U}} - \overline{\mathbf{U}}^2) \quad (101)$$

$$M = \delta^2 (\|\overline{D}\|D - 4\overline{D}D) \quad (102)$$

For the DES and LES simulations a Gauss linear scheme was used for calculating the laplacian and the gradient of all terms, a Gauss upwind was used for the divergence of velocity while a limited linear Gauss scheme was used for all turbulent terms. For time backward difference was implemented.

C.3 DES/LES WALL FUNCTIONS

Similar to the efforts taken for correcting the subgrid scale viscosity in RANS simulations, effort has been given to implement wall models for LES such that it is not necessary to satisfy $y^+ = 1$ at the wall. While several methodologies have been developed for modeling ν_{SGS} in OpenFOAM the only wall function implemented is that originally developed by Spalding

[72]. Spalding's Law of the Wall implements the relationship for subgrid scale viscosity shown in Equation (103), where the shear velocity U_τ is given in Equation where y^+ is implemented as shown on the right hand side of Equation (104). It is necessary to solve Equation (104) for the shear layer velocity U_τ which in OpenFOAM® is done utilizing a Newton-Raphson method to find the roots of the equation. The unified wall function shown provides the benefit of not having to worry about the first cell center next to a wall being in the logarithmic region of the shear velocity profile. This wall function is used for subgrid scale viscosity on the upstream wall of the domain.

$$\nu_{SGS} = \frac{U_\tau}{|\nabla U|} - \nu \quad (103)$$

$$\frac{|U|}{U_\tau} = \frac{1}{\kappa} \ln(Ey^+) = \frac{1}{\kappa} \ln \left[E \frac{|U|}{U_\tau} + e^{-\kappa \frac{|U|}{U_\tau}} - 1 - \kappa \frac{|U|}{U_\tau} - \frac{1}{2} \left(\kappa \frac{|U|}{U_\tau} \right) - \frac{1}{6} \left(\kappa \frac{|U|}{U_\tau} \right)^2 \right] \quad (104)$$

C.4 TRANSIENT SOLUTIONS (DES AND LES) – PISOFOAM

Transient flow problems are solved using a Pressure Implicit correction with Splitting Operations algorithm (PISO) originally developed by Issa [73]. Given a time n when the velocity and pressure are known/prescribed, the first momentum prediction step, denoted as *, is used to implicitly determine the velocity field according to Equation (105). Note that in Equation (105), H represents the discretized convection and diffusion terms, combined with any possible source terms. Similarly, Δ_i represents the finite-difference equivalent of the spatial derivative with respect to x_i ($\partial / \partial x_i$). The second step involves correcting the pressure based on the corrected momentum field. Utilizing the corrected momentum field, the explicit momentum equation is

shown in Equation (106). However, if one takes the divergence of Equation (106), and assumes $\Delta_i u_i^{**} = 0$, an explicit expression for the pressure p^* is derived, as shown in Equation (107). Once p^* is found from Equation (107), Equation (106) can be solved for u^{**} , which will satisfy continuity based on the assumptions made. This correction step is then repeated in a loop until adequate convergence is found, before the solution is then advanced in time to step $n+1$, where the process is then carried out again.

$$\frac{\rho}{\Delta t} (u_i^* - u_i^n) = H(u_i^*) - \Delta_i p^n \quad (105)$$

$$\frac{\rho}{\Delta t} (u_i^{**} - u_i^n) = H(u_i^*) - \Delta_i p^* \quad (106)$$

$$\Delta_i^2 p^* = \Delta_i H(u_i^*) + \frac{\rho}{\Delta t} \Delta_i u_i^n \quad (107)$$

BIBLIOGRAPHY

- [1] Anderson, N., Hassan, Y. and Schultz, R. “Analysis of the hot gas flow in the outlet plenum of the very high temperature reactor using coupled RELAP5-3D system code and CFD code.” *Nuclear Engineering and Design*. Vol. 238, 2008, pp. 274–279.
- [2] S.B. Rodriguez and M.S. El-Genk, “On Enhancing VHTR Lower Plenum Heat Transfer and Mixing via Swirling Jet.” *Procs. of ICAPP 10*, Paper 10160, 2010.
- [3] Bayless. “RELAP5/ATHENA calculations of VHTR conduction-cooldown. Private communication.” 2006.
- [4] S. Mazumdar, D.T. Landfried, A. Jana, and M. Kimber, “Initial computation study of the thermal mixing in a VHTR lower plenum”, *Proceedings – 15th International Topical Meeting on Nuclear Reactor Thermal Hydraulics, NURETH-15*, 2013.
- [5] H. M. McIllroy, D. M. McEligot, and R. J. Pink “Measurement of turbulent flow phenomena for the lower plenum of a prismatic gas-cooled reactor,” *Nuclear Engineering and Design*, vol 240, 2010, pp. 416-428.
- [6] D. P. Guillen, and H. M. McIllroy, “Preliminary study of turbulent flow in the lower plenum of a gas-cooled reactor,” *Proceedings - 12th International Topical Meeting on Nuclear Reactor Thermal Hydraulics, NURETH-12*, 2007.
- [7] D. P. Guillen, “Computational flow predictions for the lower plenum of a high-temperature, gas-cooled reactor,” *Transactions of the American Nuclear Society*, vol. 95, 2006, pp. 827-828
- [8] R. W. Johnson, “Modeling strategies for unsteady turbulent flows in the lower plenum of the VHTR,” *Nuclear Engineering and Design*, vol. 238, 2007, pp. 482-491.
- [9] N. Tauveron, “Thermal Fluctuations in the Lower Plenum of a High Temperature Reactor,” *Nuclear Engineering and Design*, vol. 222, 2003, pp. 125-137.

- [10] J. D. Hodson, R. E. Spall, and B. L. Smith, "RANS predictions in an idealized lower-plenum model," *International Conference on Nuclear Engineering, Proceedings, ICONE 14*, 2006.
- [11] K. G. Condie, G. E. McCreery, H. M. McIlroy, D. M. McEligot, "Development of an experiment for measuring flow phenomena occurring in a lower plenum for VHTR CFD Assessment," INL/EXT-05-00603, September 2005.
- [12] P. Chellapandi, S. C. Chetal, and B. Raj, "Thermal striping limits for components of sodium cooled fast spectrum reactors," *Nuclear Engineering and Design*, Vol. 239, 2009, pp. 2754-2765.
- [13] J. H. Kim, R. M. Roidt, and A. F. Deardorff, "Thermal stratification and reactor piping integrity," *Nuclear Engineering and Design*, Vol. 139, 1993, pp. 83-85.
- [14] N. Kimura, H. Ogawa, and H. Kamide, "Experimental study on fluid mixing phenomena in a T-pipe junction with upstream elbow," *Nuclear Engineering and Design*, Vol. 240, 2010, pp. 3055-3066.
- [15] H. Kamide, M. Igarashi, S. Kawashima, N. Kimura, and K. Hayashi, "Study on mixing behavior in a tee piping and numerical analyses for evaluation of thermal striping," *Nuclear Engineering and Design*, Vol. 239, 2009, pp. 58-67.
- [16] A. Nakamura, T. Oumaya, and N. Takenaka, "Numerical investigation of thermal striping at a mixing tee using detached eddy simulation," *Proceedings NURETH-13*, Kanazawa City, Ishikawa Prefecture, Japan, 2009.
- [17] A. Tokuhiko and N. Kimura, "An experimental investigation on thermal striping mixing phenomena of a vertical non-buoyant jet with two adjacent buoyant jets as measured by ultrasound doppler Velocimetry," *Nuclear Engineering and Design*, Vol 188, 1999, pp. 49-73.
- [18] N. Kimura, M. Nishimura, and H. Kamide, "Study on convective mixing for thermal striping phenomena (experimental analyses on mixing process in parallel triple-jet and comparisons between numerical methods)," *JSME International Journal, Series B*, vol. 45, 2002, pp. 592-599.
- [19] N. Kimura, H. Miyakoshi, and H. Kamide, "Experimental investigation on transfer characteristics of temperature fluctuation from liquid sodium to wall in parallel triple-jet," *International Journal of Heat and Mass Transfer*, Vol. 50, 2007, 2024-2036.
- [20] S. Choi and S. Kim, "Evaluation of turbulence models for thermal striping in a triple-jet," *Journal of Pressure Vessel Technology*, Vol. 129, 2009, pp. 583-592.

- [21] R. Knystautas, "The turbulent jet from a series of holes in a line." *The Aeronautical Quarterly*, Vol. 15, 1964.
- [22] B. Pani, and R. Dash, "Three-dimensional single and multiple free jets," *Journal of hydraulic engineering*, Vol. 109, 1983, pp 254-269.
- [23] T. Harima, S. Fujita, and H. Osaka, "Mixing and diffusion processes of the twin circular free jets with various nozzle spacings," *Experimental Heat Transfer, Fluid Mechanics, and Thermodynamics*, 2001
- [24] K. Svensson, "Experimental and Numerical Investigations of Confluent Round Jets," PhD Thesis, Kinkping University, Sweden, 2015.
- [25] Y. A. Cengel, and J. M. Cimbala, "Fluid Mechanics: Fundamentals and Applications," 1st ed., McGraw Hill.
- [26] H.S. Bean, ed. "Fluid meters: Their theory and application." Vol. 2. American Society of Mechanical Engineers, 1971.
- [27] G.E. McCreery and K.G. Condie, "Experimental Modeling of VHTR Plenum Flows During Normal Operation and Pressurized Conduction Cooldown," INL/EXT-06-11760, September 2006.
- [28] D. M. McEligot and G. E. McCreery, "Scaling studies and conceptual experiment designs for NGNP CFD Assessment," INEEL/EXT-04-02502, 30 November 2004.
- [29] N. Anderson, Y. Hassan, R. Schultz, "Analysis of the hot gas flow in the outlet plenum of the very high temperature reactor using a coupled RELAP5-3D system code and a CFD code," *Nuclear Engineering and Design*, Vol. 238, 2009, pp. 274-279.
- [30] M.A. Van Horn, "Scaling of the Thermal Mixing Processes within the Lower Plenums of VHTR Designs," Master Thesis, Oregon State University, June 2, 2005.
- [31] R. L. Panton, "Incompressible Flows," John Wiley and Sons, 2006.
- [32] R. D. Mehta, "Turbulent Boundary Layer Perturbed by Screen," *American Institute of Aeronautics and Astronautics Journal*, Vol. 23, 1985, pp. 1335-1342.
- [33] J. Scheiman, "Comparison of Experimental and Theoretical Turbulence Reduction Characteristics for Screens, Honeycomb, and Honeycomb-Screen Combinations," NASA Technical Paper, 1958.
- [34] R.D. Metha, P. Bradshaw, "Design rules for small low speed wind tunnels," *Journal of Royal Aeronautical Society*, Vol. 73, 1970.

- [35] J.H. Bell, and R.D. Mehta. "Contraction design for small low-speed wind tunnels," NASA Contractor Report NASA-CR-177488 (1988).
- [36] HEXCEL Composites, "HexWeb™ Honeycomb Attributes and Properties: A comprehensive guide to standard Hexcel honeycomb materials, configurations, and mechanical properties," 1999.
- [37] H. Schlichting, "Boundary-Layer Theory 7th Edition," McGraw Hill Press, USA, 1979
- [38] J. Mi, D.S. Nobes, and G.J. Nathans, "Influence of jet exit conditions on the passive scalar field of an axisymmetric free jet," *Journal of Fluid Mechanics*, Vol. 432, 2001, pp. 91-125.
- [39] S. Mazumdar, D.T. Landfried, A. Jana, and M. Kimber, "Computational study of confined isothermal turbulent round jets." Proceedings – 15th International Topical Meeting on Nuclear Reactor Thermal Hydraulics, NURETH-15, 2013.
- [40] B.E. Launder and D.B. Spalding, "Lectures in mathematical Models of Turbulence." Academic Press, London, England, 1972.
- [41] D.C. Wilcox, "Turbulence Modeling for CFD", 2nd Edition, DCW Industires, Anaheim, 1998.
- [42] W. C. Reynolds. "Fundamentals of turbulence for turbulence modeling and simulation." Lecture Notes for Von Karman Institute Agard Report No. 755, 1987.
- [43] T.-H. Shih, W. W. Liou, A. Shabbir, Z. Yang, and J. Zhu. "A New k - ϵ Eddy-Viscosity Model for High Reynolds Number Turbulent Flows – Model Development and Validation." *Computers Fluids*, Vol. 24, 1995, pp. 227-238.
- [44] S.B. Pope, "An explanation of the turbulent round-jet/plane-jet anomaly," *AIAA Journal*, 1978.
- [45] B.E. Launder, G.J. Reece, and W. Rodi, "Progress in the development of a Reynolds-stress turbulence closure," *Journal of Fluid Mechanics*, Vol. 68, 1975, 537-566.
- [46] B.J. Daly and F.H. Harlow, "Transport equation in turbulence." *Physics of Fluids*, 33, 1970
- [47] S. Pope "Turbulent Flows." Cambridge University Press, 2006.
- [48] K. Hanjalic and B. Launder, "Modeling turbulence in engineering and the environment. Second-moment routes to closure." Cambridge University Press, 2011.
- [49] T. Wei and W.W. Willmarth. "Reynolds-number effects on the structure of a turbulent channel flow." *Journal of Fluid Mechanics*, Vol. 204, 1989, pp. 57-95.

- [50] B.E. Launder and D.B. Spalding. "The Numerical Computation of Turbulent Flows". *Computer Methods in Applied Mechanics and Engineering*. 3. 269–289. 1974.
- [51] S.V. Patankar and D.B. Spalding, "A calculation procedure for heat, mass, and momentum transfer in three-dimensional parabolic flows." *International Journal of Heat and Mass Transfer*, Vol. 15, 1972, pp. 1787–1806.
- [52] H. Jasak, *Error analysis and estimation for the finite volume method with applications to fluid flows*. PhD thesis, London Imperial College, London, 1996.
- [53] Roache, P.J. 1997 Quantification of uncertainty in computational fluid dynamics. *Annual Review of Fluid Mechanics* 29, 123–160.
- [54] I.B. Celik, G. U. Ghia, and P.J. Roache, "Procedure for estimation and reporting of uncertainty due to discretization in CFD applications." *Journal of fluids*, Vol. 130, 2008.
- [55] D.T. Landfried, A. Jana, and M. Kimber, "Characterization of the behavior of confined laminar round jets." Under Review for publication in *Journal of Fluid Mechanics*, 2013.
- [56] W. Oberkampf and C. Roy. "Verification and Validation in Scientific Computing." Cambridge University Press, New York, 2010.
- [57] H.H. Bruun, "Hot Wire Anemometry: Principles and Signal Analysis," Oxford university Press, USA 1995.
- [58] K. Dobbeling, B. Lenze, and W. Leuckel, "Basic considerations concerning the construction and usage of multiple hot-wire probes for high turbulent three-dimensional flows," *Measurement Science Technology*, Vol. 1, 1990, pp. 924-933.
- [59] I.C. Lekakis, R.J. Adrian, and B.G. Jones, "Measurements of velocity vectors with orthogonal and non-orthogonal triple-sensor probes," *Experiments in Fluids*, Vol. 7, 1989, pp. 228-232.
- [60] P.V. Vukoslavcevic, D.V. Petrovic, and J.M. Wallace, "An analytical approach to the uniqueness problem of hot-wire probes to measure simultaneously three velocity components," *Measurement Science Technology*, Vol. 15, 2004, pp. 1848-1854.
- [61] F.E. Jorgensen "How to measure turbulence with hot-wire anemometers – a practical guide," Dantec Dynamics, 2002.
- [62] L.H. Benedict, and R.D. Gould, "Towards better uncertainty estimates for turbulence statistics," *Experiments in Fluids*, Vol. 22, 1996, pp. 129-136.
- [63] P.R. Spalart and S.R. Allmaras, "A one-equation turbulence model for aerodynamic flows." *Recherche Aerospaciale*, No. 1, 1994, pp. 5-21

- [64] B. Aupoix and P.R. Spalart, "Extensions of the Spalart-Allmaras turbulence model to account for wall roughness." *International Journal of Heat and Fluid Flow*, Vol 24, 2003, pp. 454-462
- [65] C.L. Rumsey, D.O. Allison, R.T. Bierdron, P.G. Buning, T.G. Gainer, J.H. Morrison, S.M. Rivers, S.J. Mysko, and D.P. Witkowski, "*CFD sensitivity analysis of a modern civil transport near buffet-onset conditions*," NASA/TM-2001-211263, December 2001
- [66] S. Salkhordeh, Large Eddy Simulations of isothermal and non-isothermal turbulent flows for High Temperature Gas Cooled Reactors. PhD Thesis, University of Pittsburgh, Pittsburgh PA 2015.
- [67] J. Smagorinsky, "General circulation experiments with the primitive equations. I: The basic Experiment," *Monthly Weather Review*, Vol. 91, 1963, pp 99-165.
- [68] M. Germano, U. Poimelli, P. Moin, W.H. Cabot, "A dynamic subgrid-scale eddy viscosity model." *Physics of Fluids A*, Vol. 3, 1991, pp. 1760-1765
- [69] P. Sagaut. "Large Eddy Simulations for Incompressible Flows," Springer Press, USA, 1998.
- [70] K. Hanjalic, and B.E. Launder, "Modelling Turbulence in Engineering and the Environment." Cambridge University Press, United Kingdom, 2011.
- [71] E. de Villiers, The potential of large eddy simulation for the modeling of wall bounded flows. PhD Thesis, London Imperial College, London, 2006.
- [72] D.B. Spalding, "A single formula for the 'Law of the Wall'," *Journal of Applied Mechanics*, Vol. 28, 1961. Pp. 455-458
- [73] R.I. Issa, "The computation of compressible and incompressible recirculating flows by a non-iterative implicit scheme," *Journal of Computational Physics*, Vol. 62, 1985, pp. 66-82.